Dissertation zur Erlangung des Doktorgrades

der Fakultät für Chemie und Pharmazie

der Ludwig-Maximilians-Universität München

Optical and electrophysiological approaches to examine the role of cAMP-dependent regulation of the sinoatrial pacemaker channel HCN4.

Verena Friederike Brox, geb. Schöttle

aus Herrenberg, Deutschland

2019

Für meine Mutter

Table of contents

1   Introduction

The average heart rate (HR) of an adult human at rest varies between 56 – 100 beats per minute (bpm), however, HR can be increased by up to 300%. Physical activity or physiological stress, for example anxiety, aggression or excitement are characteristically accompanied by an HR acceleration to adapt cardiac output to the given circumstances. Adjustment of the HR, also known as the chronotropic effect, is a mechanism controlled by the autonomic nervous system (ANS). The ANS comprises sympathetic and parasympathetic nerves that regulate the firing frequency of the dominant pacemaker of the heart, the sinoatrial node (SAN). The sympathetic branch of the ANS induces an increase in HR, whereby the parasympathetic branch leads to a decline in firing rate of the pacemaker. A critical determinant of HR regulation by the ANS is the second messenger cyclic adenosine monophosphate (cAMP) that promotes intracellular signal transduction. A potential target within the SAN are hyperpolarization-activated cyclic nucleotide-gated (HCN) channels, mainly HCN4 channels, which underlie a cAMP-dependent regulation (CDR) [1,2].

1.1   Architecture of the sinoatrial node

The primary pacemaker of the heart, the SAN, is the component of the cardiac conduction system that initiates the heartbeat. Specialized pacemaker cells within the SAN generate spontaneous electrical signals which are conducted to the surrounding tissue.
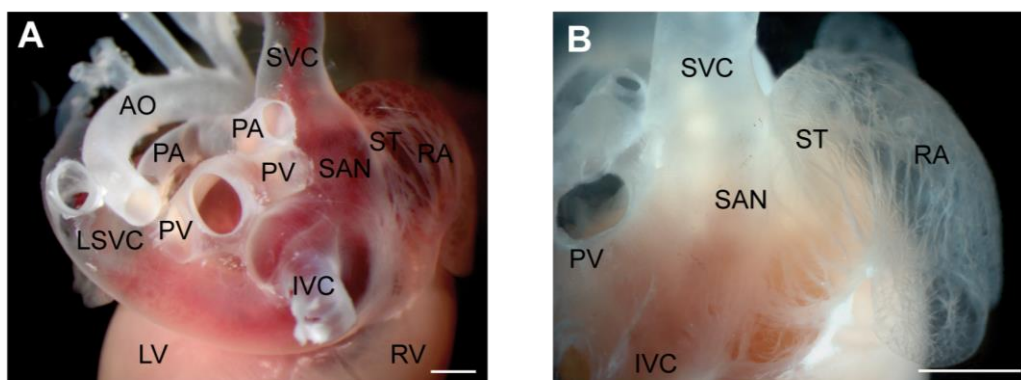
Fig. 1 Anatomical localization of the SAN. (A) Dorsal view of a gelatin-inflated mouse heart. (B) Epicardial, dorsolateral view of the right heart and magnification of the right atrium (RA) and sinoatrial node (SAN) area. The SAN is located between the superior vena cava (SVC), the inferior vena cava (IVC) and the sulcus terminalis (ST). Further abbreviations: PV, pulmonary vein; PA, pulmonary artery; AO, aorta; LSVC, left superior vena cava, LV, left ventricle; RV, right ventricle. Scale bars, 0.5 mm. Images are adapted from [3,4].

The SAN was anatomically identified in mammalian heart for the first time in 1907 by Arthur Keith and Martin Flack [5]. The murine SAN forms an approximately 1.5 mm long, comma-shaped, three-dimensional structure that is located in the intercaval region of the superior (SVC) and inferior vena cava (IVC) (Fig. 1). From the endocardial view, the territory of the SAN extends parallel to the crista terminalis (CT) and is laterally delimited by the CT and the interatrial septum (IAS). Epicardially the SAN extends along the sulcus terminalis (ST) [6].

The SAN is functionally almost completely insulated from the surrounding atrial myocytes. The insulation is composed of the SAN artery and connective tissue, which create a block zone around the SAN to shield it from hyperpolarizing influences from the atrial muscle [7]. Connective tissue consists of layers of fibroblasts, adipocytes and collagen fibers which are rarely interrupted by strands of pacemaker cells that protrude into the right atrial muscle and thereby build discrete interdigitations between SAN and atrium [6]. However, an additional functional barrier is provided by reduced electrical coupling properties of SAN cells which protect the tissue from external electrical activation and lead to very low conduction velocity within the SAN compared to the atrial muscle. Intercellular connections between the single cells in the tissue network are built by gap junctions that are composed of connexin (Cx) proteins [8]. Pacemaker cells exhibit a lower number of gap junctions and a characteristic pattern of Cx protein expression compared to atrial cells. Interestingly, Cx43, an ubiquitous member of the Cx family in the working myocardium, is absent in the SAN although Cx45 [6] and Cx40 [9] are expressed. Conduction velocity in the SAN is additionally reduced due to a lower depolarization rate in pacemaker cells compared to the working myocardium. The diastolic membrane potential of pacemaker cells is mainly driven by relatively slow L-type calcium currents instead of fast sodium currents found in other cardiac tissue [10].

The SAN can be subdivided into three major pacemaker compartments: head, body, and tail. Cell morphology and fibre orientation vary in these different regions of the SAN. The head of the SAN is located near the SVC and is also called the compact region of the SAN, because nodal cells are tightly packed and sparsely separated by connective tissue. The cells in this region are very small and poorly organized. In the body of the SAN, the arrangement of the cells becomes more regular as cells are orientated perpendicular to the CT. In the more inferior part, the tail region, cells are larger, more loosely packed, and oriented parallel to the CT. In general, pacemaker cells are smaller compared to atrial cells and contain a lower amount of myofilaments.

Pacemaker cells can be subdivided into three major classes: elongated, spindle, and spider cells. Elongated shaped cells are faintly striated, contain one or more nuclei, and exhibit a length of approximately 80 µm. Spindle cells have a similar shape but are shorter (approximately 50 µm) than elongated cells and are mono-nucleated. Spider cells are

irregularly shaped with a various number of branches with blunt ends. The head of the SAN is predominantly formed by spindle and spider cells [6,11,12].

Within the heterogeneous structure of the SAN described above, a small cluster of dominant pacemaker cells form the first excitation site within the SAN. During normal sinus rhythm the leading pacemaker site is primarily located in the head of the SAN close to the CT. However, multiple pacemaker sites are present in the SAN and a pacemaker hierarchy within the SAN can be observed with the fastest pacemaker located at the superior part (head) and the slowest at the inferior part (tail). The cluster of cells with the fastest firing frequency takes over the initiation of the heartbeat and thereby sets the HR. It has been shown, that an acceleration of the firing rate by isoproterenol shifts the leading pacemaker position superiorly within the SAN, whereby a decrease in firing rate by acetylcholine (ACh) shifts the leading pacemaker site more inferiorly within the SAN [13]. This phenomenon of multiple pacemaker sites and a shift of the leading pacemaker is thought to be due to regional differences in ionic current density within the SAN [14].

From the leading pacemaker site, the signal propagates slowly to the right atrium (RA) where it continuous through different sinoatrial conduction pathways (SACP) to excite the atrium. In the murine heart, in general, two SACPs constitute the breakthrough pathways in direction to the atrium and result in a sinoatrial conduction time (SACT) of approximately 5 ms [15]. Subsequently, the signal spreads rapidly through the atria to the atrioventricular node (AVN). In addition to the SAN, the cardiac conduction system consists of the AVN, the bundle of His and the Purkinje fibres (Fig. 2). Conduction in the AVN is very slow which results in a delay between atrial and ventricular excitation and thereby allows for sufficient filling of the ventricles with blood before the following contraction. The AVN also serves as a secondary pacemaker and takes over the excitation of the heart in the case of SAN failure. Following AVN excitation, the signal rapidly propagates through the His-Purkinje system which communicates the impulse to the ventricular muscle [12,17]. This specific chronologic sequence of electrical events is essential for normal cardiac excitation.
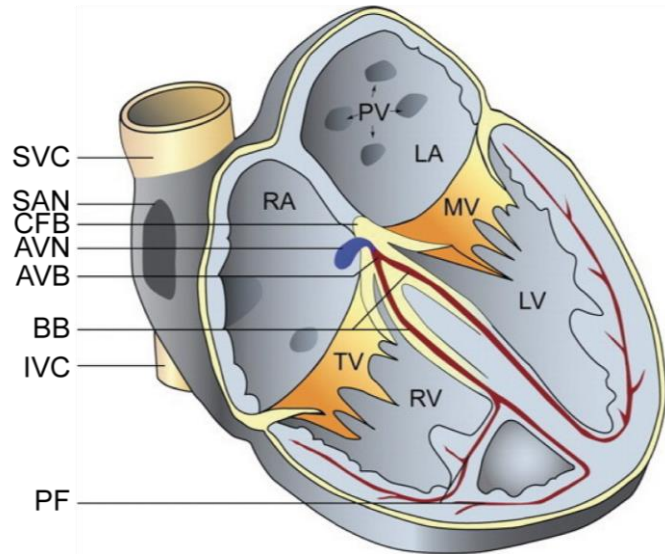
Fig. 2 Cardiac electrical conduction system. Schematic illustration of the mammalian cardiac conduction system. The first excitation site is located in the sinoatrial node (SAN). SAN extends in the intercaval region of the superior vena cava (SVC) and the inferior vena cava (IVC) within the right atrium (RA). The atrioventricular node (AVN) is located between the central fibrous body (CFB) and the tricuspid valve (TV). The atrioventricular bundle (AVB) splits up in two bundle branches (BB) that branch out to the left and right purkinje fibre (PF) network. Further abbreviations: LA, left atrium; PV, pulmonary veins; MV, mitral valve; RV, right ventricle; LV, left ventricle. Image is adapted from [1,16].

1.2   Hyperpolarization-activated cyclic nucleotide-gated (HCN) channels

A specific characteristic of pacemaker cells allows for its ability to generate spontaneous action potentials (AP). SAN cells do not exhibit a stable resting membrane potential. Instead, the AP reaches its maximum diastolic potential (at approximately -55 to -60 mV) and is automatically followed by depolarization of the membrane which results in the ensuing AP [18]. Pacemaker automaticity depends on a specific ion channel expression profile of SAN cells. Almost all cardiac pacemaker cells express hyperpolarization-activated cyclic nucleotide-gated (HCN) channels.

HCN channels are nonselective cation channels mainly permeable for Na^+ and K^+ and thereby constitute a depolarizing inward current termed I_f, (funny), I_q (queer) or I_h (hyperpolarization; for the present thesis the term I_h is used). HCN channels are named after their specific feature to be voltage-gated but activated upon hyperpolarization and deactivated by depolarization. Consequently, I_h current significantly contributes to a depolarizing current during diastole. This current is a key determinant of pacemaker automaticity and is called slow diastolic depolarization (SDD). SDD facilitates opening of other voltage-gated channels, like T-type or L-type calcium channels and thereby promotes the generation of an AP. The slope of SDD

determines the firing frequency. A second feature of HCN channels is their ability to be modulated by a second messenger, the cyclic nucleotide cAMP. Binding of cAMP modifies the gating properties of HCN4 channels by facilitating opening of the channels [19–22].

HCN channels are mainly expressed in the heart and central nervous system where they have been studied in detail since their discovery. In addition, HCN expression has been reported in other tissues like pancreatic B cells, the enteric nervous system and the urinary bladder, however, their physiological function in these tissues is still a matter of debate [23–26]. HCN channels comprise a small gene family of four distinct members (HCN1 - 4). In the human and murine heart all four HCN channel isoforms have been detected with varying expression levels in the different cardiac regions. In SAN, HCN4 is the major isoform carrying 80% of I_h, while HCN1 and HCN2 account for the remaining fraction of the current. A profound expression of HCN1 and its contribution to I_h was recently identified in mouse SAN tissue. In other parts of the conduction system, like AVN and Purkinje fibres, HCN4 also forms the major isoform [27,28]. However, HCN3 is not expressed in the conduction system and was found to play a pivotal role in the repolarization process of the ventricles [29].

1.2.1 Properties of the HCN channel core unit

HCN channels are part of the pore-loop cation channel superfamily and form a subfamily together with cyclic nucleotide-gated (CNG) channels and K^+ channels of the ether-à-go-go-type (KCNH) that is characterized by a cyclic nucleotide-binding domain (CNBD) [20,30].

HCN channels consist of four subunits that are organized in the cytoplasmic membrane to build a central pore in form of homo- or heterotetramers [31]. Each subunit consists of three major domains: the channel core region, the cytosolic N-terminus and the cytosolic C-terminus (Fig. 3). The most critical region for channel function is the core region which is formed by six alpha-helical transmembrane segments (S1 - S6). Segments S5 and S6 build the channel´s pore which is connected by an S4 - S5 linker to the voltage sensing domain (VSD) formed by S1 - S4.
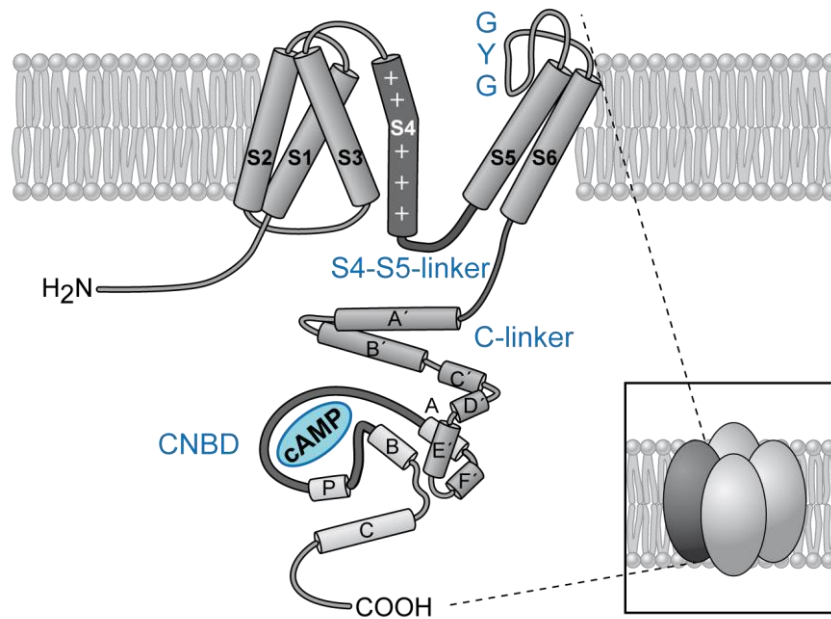
Fig. 3 Schematic structure of an HCN channel. Illustration of a single subunit and the corresponding HCN channel tetramer (inset). One subunit comprises six transmembrane segments (S1 - S6) and the cytosolic N- and C-terminus. The pore of the channel is formed by S5 and S6. An incorporated GYG motif serves as selectivity filter. The pore is connected by a S4-S5 linker to the voltage-sensing domain (VSD) represented by S1 - S4. The C-terminus comprises the C-linker (A´ - F´) and the cyclic nucleotide binding domain CNBD (A, B, C, and P) where cAMP is able to bind. Letters A - F stand for α-helices. Figure is adapted from [32].

In addition, the pore contains a characteristic amino acid sequence: glycine-tyrosine-glycine (GYG). This specific motif serves as the selectivity filter, conforms to the motif found in K^+ channels, and is essential for K^+ selectivity [33]. Since HCN channels are found to be nonselective cation channels permitting K^+ over Na^+ by a ratio of approximately 4:1 [20], the molecular basis of ion selectivity was recently investigated by cryogenic electron microscopy of the human HCN1 channel [34]. In K^+ channels ion selectivity is served by four binding sites provided by carbonyl oxygen atoms that coordinate K^+ within the GYG motif [35]. However, in HCN channels a conformational difference in tyrosine of GYG sequence results in only two cation binding sites and therefore explains the nonselectivity of HCN channels [34].

The gate of HCN channel´s pore is formed by the intracellular end of transmembrane segment S6 which possesses properties of a "hinge" that moves during channel gating. This particular process of gating is controlled by two gating domains in HCN channels: the transmembrane VSD and the intracellular CNBD. VSD is located in the S4 helix which is composed of multiple positive charged amino acid residues (arginine and lysine) at every third position [36]. These charges along S4 detect changes in membrane potential resulting in a transmembrane movement of S4 which triggers the opening of the pore gate [37]. Despite the fact that all voltage-gated members of the pore-loop cation channel superfamily share a similar topology of VSD,

in HCN channels the gate opens only upon hyperpolarization and closes during depolarization of the plasma membrane. The molecular specificity of gate opening during hyperpolarization is still a matter of debate [38].

It has been recently discovered that S4 of HCN channels exhibits an extraordinary length with two additional helical turns compared to other voltage-gated channels. Thereby, S4 extends further into the cytoplasm where it brings the S4 - S5 linker into contact with the C-linker of a neighboring subunit. It was hypothesized that in the depolarized conformation, force exerted by S4 leads to a twist of the C-linker and thereby stabilizes closure of the pore. It was proposed that during hyperpolarization of the cell a displacement of S4 releases the constraints on the C-linker and S6 which allows the pore to open [34]. However, after truncation of S4 in HCN1 by three helical turns, activation upon hyperpolarization was still preserved which implies that the length of S4 may not be a critical determinant for the opening of HCN channels during hyperpolarization [39]. In addition, mutation of the linkage between VSD and the S4 - S5 linker revealed that the S4 - S5 linker is not required for hyperpolarization-dependent activation [40].

1.2.2 Properties of the HCN channel cAMP binding module

HCN channels harbor a CNBD in the intracellular C-terminal region where cyclic nucleotides are able to bind to the channel. The binding of cAMP to CNBD accelerates the activation kinetics and shifts the voltage dependence of activation to more positive voltages. This modulation causes the channels to open faster and more completely in the presence of cAMP [21,41]. However, cAMP is not the only cyclic nucleotide that can bind to HCN channels. Both, cyclic guanosine monophosphate (cGMP) and cyclic cytosine monophosphate (cCMP) are ligands of the binding domain but exhibit a 30-fold lower affinity compared to cAMP [20,42].

The molecular determinants and the structural changes of the C-terminus upon binding of cAMP in the murine HCN2 channel [41], the human HCN4 channel [43], and the human HCN1 channel [34] were elucidated recently by cryo-electron microscopy and crystallographic techniques. Each of the four subunits of the HCN channel contains an intracellular CNBD domain which is connected by a C-linker to the transmembrane segment S6 of the pore. The C-linker consists of six α-helices, indicated as A´ - F´. Each helix is separated by short loops. Helices E´ and F´ are in contact with the subsequent CNBD, a mixed structure of four α-helices (A, P, B, C) and an eight-stranded β-roll. The β-roll is arranged in a β-jelly-roll configuration and forms the cyclic nucleotide binding pocket. The pocket contains several highly conserved residues that form electrostatic and hydrogen-bonding interactions to provide binding affinity. Binding of cAMP induces a conformational change by stabilizing the P-helix and by rotation of the B and C helices towards the β-roll. This rotation exerts an upward force on the C-linker. Consequently, the C-linker rotates in a counterclock manner to the S6 helical bundle of the

channel´s gate and thereby unwinds S6. This "twist-open" mechanism leads to a dilation of the gate, facilitating channel opening. However, this mechanism alone is insufficient to open the channel in the absence of hyperpolarization [30,34,41,43].

Within the HCN channel family the individual I_h currents differ from each other with respect to their activation time constants, their steady-state voltage dependence and their extent of cAMP-dependent modulation. Briefly, HCN3 shows slow activation kinetics and was found to be insensitive to cAMP, similar to HCN1 which reveals only a weak shift of the activation curve in presence of cAMP. However, HCN1 shows the fastest opening kinetics within the HCN channel family. HCN4 and HCN2 are highly modulated by cAMP, and binding of cAMP produces a 10 – 25 mV depolarizing shift in the half-maximal activation potential $V_{0.5}$, which indicates that channels are activated at more depolarized voltages when cAMP levels are elevated [20,32].

1.3   The role of cAMP-dependent regulation of HCN4 channels

Since HCN4 is the predominant HCN channel isoform expressed in SAN pacemaker cells and human HCN4 channelopathies are associated with a cardiac phenotype characterized by sinus bradycardia, it has been considered that CDR of HCN4 is the key mechanism of HR control by the ANS. It is believed that an upregulation of intracellular cAMP levels leads to an increase in HR given by HCN4 CDR, whereby a decline in cAMP level decreases HCN4 channel opening kinetics and slows HR [1,27,44].

Intracellular cAMP is generated by the enzyme adenylyl cyclase which catalyzes the conversion of adenosine triphosphate (ATP) to cAMP. Adenylyl cyclase can be inhibited or activated by guanine nucleotide-binding proteins (G proteins) originating from transmembrane G protein-coupled receptors (GPCRs) [45]. GPCRs involved in the autonomic regulation of the SAN are type-2 muscarinic receptors (M2-receptors) that bind the neurotransmitter ACh and beta-1 adrenergic receptors that are able to bind noradrenaline. The signal pathways described are regulated by the ANS. The cardiac ANS consists of two major components, the sympathetic branch and the parasympathetic branch. In general, the sympathetic branch accelerates HR, while the parasympathetic branch decreases HR. Briefly, sympathetic efferents release noradrenaline which binds to beta-1 adrenergic receptors, thereby activating adenylyl cyclase resulting in an increase in cAMP. In contrast, parasympathetic efferents release ACh which binds to M2-receptors, thereby inhibiting adenylyl cyclase and decreases the cAMP level [46].

To precisely determine the functional significance of HCN4 channels and their modulation by cAMP, several genetic mouse studies have been recently implemented. Experiments using mice with global HCN4 disruption as well as mice with a selective deletion of HCN4 in cardiomyocytes revealed that HCN4 is essential for embryonic pacemaker development. Both mutations led to death in utero between embryonic days 9.5 - 11.5. The beating frequency of hearts from HCN4-deficient embryos was significantly reduced and hearts did not respond to β-adrenergic stimulation and to the associated cAMP stimulation [47]. In addition, mice carrying a mutation in CNBD that abolished cAMP binding also died at the embryonic stage and the embryonic hearts similarly did not respond to cAMP. Together, these investigations indicate that CDR of HCN4 is indeed essential for HR control [48]. However, studies on adult mice with a temporally, tamoxifen-induced deletion of HCN4 contradicted these findings. In the study of Baruscotti et al [49] mice showed severe bradycardia and died 5 days after tamoxifen treatment. In contrast, the inducible HCN4 knockout in the work of Herrman et al [50] was not lethal but also showed cardiac arrhythmias characterized by recurrent sinus pauses. However, in both studies HR response to sympathetic drugs was preserved. This argues against a major role of HCN4 in principal HR control but suggests the channel to be essential for impulse generation and to maintain stable cardiac rhythm.

Analyses of human HCN4 channelopathies also support a key role of HCN4 channels in heart rhythmicity. Since 2003 several loss-of-function mutations in the HCN4 gene were identified and have been associated with sinus node dysfunction including sinus bradycardia. Notably, two of the previously known mutations in human directly affect cAMP modulation of HCN4, namely 573X [51] and 695X [52]. Studies of these mutations indicated that CDR of HCN4 determines basal HR but is not critical for autonomic HR control [52,53]. However, this data does not specifically provide additional insights into the role of HCN4 CDR due to an alteration of the general HCN4 architecture itself by truncation of the CNBD. In addition, all patients were heterozygous for the HCN4 mutation and therefore express the mutation in only one allele [44,54].

1.4   Optical mapping to investigate spontaneous generation and spread of cardiac excitation

In the last decades, investigations of cardiac electrophysiology have mainly focused on the cellular mechanisms using microelectrode techniques performed on single cells or on multicellular preparations. These experiments elucidated fundamental knowledge about the electrical properties of single cardiac cells. However, to fully understand heart physiology it is crucial to consider the heart as a functional syncytium of many electrically and mechanically connected cardiomyocytes [55]. Convenient methods, like electrocardiography, surface electrode measurements or ultrasound imaging techniques to investigate electrophysiological properties on the whole heart or on the tissue level suffer from low spatial resolution and are not able to precisely elucidate network behavior within the tissue [56].

In the 1970s molecular probes were discovered that bind to the plasma membrane of neurons [57] and cardiac cells [58]. These dyes follow changes in transmembrane potential by changes in fluorescence signal. These findings marked the birth of optical imaging techniques in excitable tissue. It is a method to precisely map and retrace electrical processes within cardiac and neuronal tissue by the usage of voltage-sensitive dyes and is therefore also referred to as optical mapping or voltage-sensitive-dye imaging. Fluorescent dyes used for this technique are fast-voltage-sensitive probes that are able to follow voltage changes in a time scale of microseconds [59]. The dyes are embedded into the cell membrane and respond to potential changes by changing their spectral properties. There are several theories which explain their voltage sensitivity. One is the solvatochromic theory implying that the electrical field induces a molecular rearrangement of the fluorescent probe within the membrane and thereby leads to a change in fluorescence [60,61]. Another explanation is provided by the electrochromic theory. There, it is thought that excitation of the tissue induces an intramolecular relocation of electronic charge along the electric field gradient [56,62].

Until now, series of potentiometric probes, including merocyanines, oxonols and styryl dyes have been discovered. However, styryl dyes exhibit specific properties that are required for cardiac optical mapping: fast-response, high signal-to-noise ratio, linear change of fluorescence with membrane potential changes and less phototoxicity of the dye [55]. Styryl dyes have been discovered in 1985 and demonstrate a group of dyes with appropriate qualities for optical recordings of membrane potentials [63]. Important members of this chromophore family are for example the dyes RH237, RH421, Di-4-ANEPPS and Di-8-ANEPPS. The molecular structure of Di-4-ANEPPS and Di-8-ANEPPS is an aminonaphthylethenylpyridinium (ANEP). These dyes respond to a 100 mV change in membrane potential by a 10% change in fluorescence. One limitation of styryl dyes is their depth of penetration which is limited to a

range of 0.5 - 2 mm [7,55,64]. If a measurement of deeper layers in the heart or of blood-perfused cardiac tissue is required, new infrared styryl dyes like di-4-ANBDQPQ or di-4-ANBDQBS can be applied [65].

In general, to perform optical mapping recordings an optical setup including an appropriate high-speed photodetector, a proper illumination technique as well as a suitable filter system is required. In addition, an appropriate dye and a cardiac contraction blocker have to be chosen. Available detectors for optical mapping are photodiode arrays, photomultiplier tubes, charge-coupled device (CCD) cameras and complementary metal oxide semiconductor cameras (CMOS). Illumination of the tissue during recording is given by light-emitting diodes (LEDs) or by xenon and halogen lamps. A cardiac contraction uncoupler is required to eliminate motion artifacts of the beating heart while recording voltage changes. Convenient blockers are 2,3-butanedione monoxime, cytochalasin D and blebbistatin, a specific myosin II inhibitor [55,66,67]. Importantly, the components have to be carefully chosen for the data intended to obtain by the user. The recorded optical signals allow for the exact localization of the leading pacemaker and the excitation pattern within the tissue [13]. In addition, the method provides a tool to measure conduction velocity and action potential duration [64].

1.5   Technique to investigate autonomic SAN regulation *in vivo*

As described above the cardiac conduction system is innervated by several efferent neurons of the ANS. The cardiac parasympathetic nerves are part of the vagus nerve. The sympathetic fibers project from autonomic ganglia along the cervical and thoracic spinal cord to the superficial layers of cardiomyocytes [68]. The region where nerve fibers innervate cardiac tissue is called intrinsic cardiac neuronal plexus. The SAN network is supplied by four epicardial nerves deriving from both, the dorsal right atrial and right ventral nerve subplexus [1,69].

Both, parasympathetic and sympathetic branch of the ANS are closely connected to each other and are activated simultaneously to keep the HR in a physiological range during rest or to adjust the HR during exercise. Changes in sympathetic activity are very slow (located in a range of 2 - 10 s) compared to changes in parasympathetic drive which are in the millisecond range (200 - 650 ms) [70,71]. The normal HR is not constant, but slightly fluctuates around a mean value. These fluctuations are called physiological heart rate variability (HRV). It is associated with several physiological processes including respiratory cycle, periodical changes in arterial blood pressure and peripheral vasomotor activity. An alteration in the physiological HRV can give a hint for deficient response to autonomic SAN regulation. Therefore, HRV data can be used as indicator for ANS response [3,72–74].

An additional parameter is the baroreceptor reflex. Blood pressure (BP) and HR are closely intertwined with each other due to the reflex mechanisms. In order to control short-term BP changes the ANS becomes activated to adjust HR to the given circumstances. Nerve endings of stretch-sensitive neurons sense BP changes in the walls of the aorta and carotid sinus by the use of baroreceptor mechanosensors PIEZO1 and PIEZO2 [75]. Signals are transmitted to the central nervous system and are then communicated to the parasympathetic and sympathetic branches of the ANS to adapt the HR. In conclusion, characteristics of baroreceptor reflex on HR regulation can be used as benchmark for SAN response to ANS innervation.

1.6   Mouse model with disrupted CDR of HCN4 channels (HCN4 FEA mice)

Since several key questions of the role of HCN4 CDR still remain unanswered, a novel mouse model with genetically disrupted cAMP binding to HCN4 channels was investigated for the present thesis. This mouse line was generated in the laboratories of Prof. Martin Biel and Prof. Christian Wahl-Schott [76]. In this mouse line (HCN4 FEA) three amino acid exchanges were introduced in the murine *hcn4* gene locus (Y527F, R669E, and T670A) (Fig. 4). T670A and R669E led to complete insensitivity of HCN4 to cAMP, whereby general HCN4 channel architecture was kept intact. These point mutations are located in the loop between the P helix and β7 sheet of the β-roll within the CNBD. Since both amino acid residues located at these positions directly interact with the phosphate group of cAMP, they were chosen to eliminate the high affinity binding of cyclic nucleotides. Advantages over other mutant mouse models in this field are that C-terminus and CNBD are completely preserved and mice do not carry genes from other species. Notably, in the mouse line HCN4-573X mentioned above, mutation led to total truncation of CNBD and parts of the C-linker [53]. The third amino acid exchange, Y527F in the C-linker, ensured the viability of the mice by partially mimicking steady-state pre-activation of HCN4 by baseline cAMP levels. As described above, previous studies revealed that CDR of HCN4 is required for embryonic development. Mutations in CNBD led to a shift of the activation threshold to more negative values than the physiological maximum diastolic potential of SAN cells. This results in a nearly complete depletion of HCN4 activity which is equivalent to a total knockout of the HCN4 channel [47,48]. HCN4 channels are constantly pre-activated in physiological conditions due to a consistent intracellular presence of cAMP in pacemaker cells [77]. To mimic pre-activation of cAMP the point mutation Y527F was introduced in the C-linker of the HCN4 channel. Exchange of tyrosine to phenylalanine facilitates the gating of the channel by shifting $V_{0.5}$ towards more positive potentials within the physiological range of SAN cells.

For the targeting strategy of the HCN4 FEA mice [76], a procedure that leads to self-induced excision of DNA sequences in sperm of male mice was chosen (Fig. 4C). A selection cassette, an ACN cassette, was introduced that carries the testis-specific promoter from the angiotensin-converting enzyme (tACE) gene. A Cre-recombinase was linked to the selectable marker Neo and to the two genes flanked with loxP elements. During spermatogenesis the tACE promoter induces expression of the Cre-recombinase gene, the ACN cassette is excised, and a single loxP element remains at the chromosomal locus [78]. The targeting vector for HCN4 FEA mice comprises exons 4 to 7 of the murine HCN4 gene. The point mutation Y527F is introduced into exon 4, exon 7 contains the mutations T670A and R669E, and intron number 4 contains the ACN cassette (Fig. 4C).
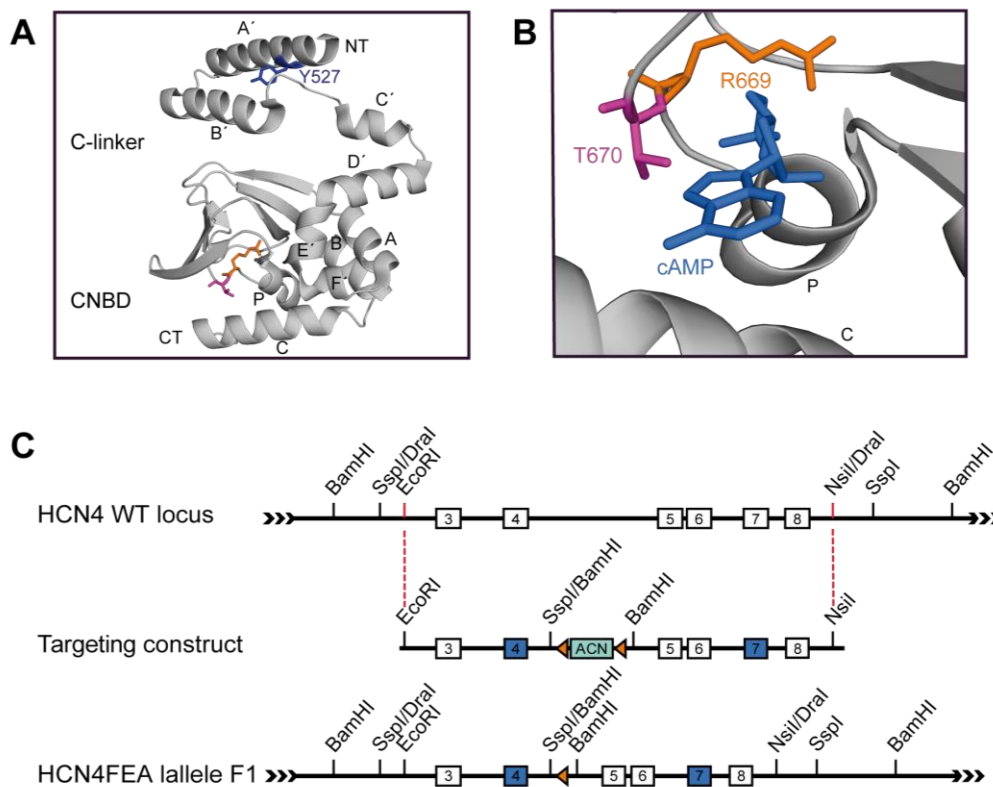
Fig. 4 Illustration of the incorporated point mutations in HCN4 FEA mice. (A) C-terminus of the HCN4 channel and key structures for the implemented point mutations (highlighted): Y527 (purple), R669 (orange), and T670 (pink). Residues R669 and T670 are located in the loop between the P helix and β-sheet of the CNBD and are required for (B) binding of cAMP (blue) within the CNBD. (C) Targeting strategy of HCN4 FEA knock-in animals. The gene locus comprises exons 3 – 8. Exons 4 and 7 carrying the mutations (Y527, R669 in the CNBD and T670 in the C-linker) are depicted in blue. Illustrations derived from human HCN4 channel structure (PDB #Q9Y3QA). Letters A – F stand for α-helices. Figure is adapted from [4].

2   Aim of the study

HCN4 is the predominant HCN channel isoform in the sinoatrial node (SAN) and mediates 80% of I_h. It has been proposed that I_h is crucial for the autonomic control of the heart rate. Mechanistically, HCN4 channels and thus I_h activity are regulated via the cAMP system. However, the functional role of cAMP-dependent regulation (CDR) of HCN4 channels and its relevance for autonomic nervous system (ANS)-mediated heart rate regulation remains to be clarified. In the following study these parts are tested by examining a novel knock-in mouse line (HCN4 FEA mice) harboring three mutations in the HCN4 channel thereby impairing cAMP binding. The present study was launched to experimentally perform cardiophysiological analyses on the whole-animal, the isolated organ and the SAN network level. For this purpose, the following methods are established beforehand and applied thereafter to the HCN4 FEA mouse line.

(1) In a first step, an optical mapping technique using fast-voltage sensitive dyes should be established for three different kinds of heart explants, i.e. isolated whole hearts, intact biatrial SAN preparations, and SAN preparations containing the right vagus nerve. This novel tool allows for visualization of the first excitation site and the propagation of the electrical signal within the specimen under basal conditions, during application of a parasympathomimetic drug and during direct vagus nerve stimulation. In a further step, calcium signals of individual cells in the intact network of the SAN should be investigated using confocal microscopy.

(2) Another goal of the present thesis is to establish telemetric recordings of combined electrocardiogram (ECG) and blood pressure (BP) and to apply it *in vivo*. In order to investigate the response of SAN firing to ANS activity, the effect of spontaneous vagus nerve inputs should be examined by an appropriate analysis of the baroreceptor reflex. Finally, ECG and BP data are used for comprehensive characterization of the cardiac phenotype of HCN4 FEA mice.

3   Materials and methods

3.1   Chemicals, solutions and buffers

Unless otherwise specified, all chemicals used were purchased from Merck KGaA, Carl Roth GmbH + Co. KG, Thermo Fischer Scientific and Bio-Rad Laboratories. The quality standard was either pro analysi or for molecular biological purposes. Highly purified and deionized water (Milli-Q water purification system, Merck Millipore®) was used for all working solutions. Additionally, solutions for long-term use were autoclaved.

3.2   Experimental animals

For the present work, a knock-in mouse line HCN4 FEA (Hcn4$^{tm3(Y527F;R669E;T670A)Biel}$) provisioned by the work of Andreas Scharr [76] and Christian Gruner [79] was used. It carries three point mutations in the HCN4 channel. The R669E and T670A mutations are inserted in the loop between the P helix and the β7 sheet of the CNBD and lead to a loss of sensitivity to cAMP. The third amino acid exchange, Y527F in the C-linker, ensured the viability of the mice by partially mimicking steady-state pre-activation of HCN4 by baseline cAMP levels. Mice were kept in accordance with legal guidelines in conventional Eurostandard Type III cages under SPF conditions, housed in a 12 h dark-light-cycle environment with *ad libitum* access to food (Ssniff; regular feed: R/M-H; breeding feed: M-Z Extrudat) and water. All animal experiments were performed according to governmental regulations and approved by the Regierung von Oberbayern. Animals used were mice from homozygous and heterozygous breeds. HCN4 FEA mice were bred on a mixed background from 129SvJ/C57-Bl6/N mice and did not differ in body weight and lifespan from their wild type (WT) littermates.

3.3   Genotyping of the experimental animals

3.3.1   Genomic DNA isolation

Genomic DNA was extracted from mouse ear biopsies by incubation of tissue in 600 µl, 50 mM NaOH for 10 min at 95°C. Subsequently, 50 µl of 1 M TrisHCl (pH = 8) were added and samples were centrifuged for 6 min at 13000 rpm. DNA present in the supernatant was utilized for polymerase chain reaction (PCR).

3.3.2   Polymerase chain reaction (PCR)

PCR was performed to amplify DNA fragments for genotyping of the experimental mice. GoTaq polymerase (Promega) and two specific, custom designed primers were used for the PCR reaction: HCN4_FEA_for 5'-CTC AAG GTC TCA GCT GAG G-3' and HCN4_FEA_rev 5'-GTA ATG TAA GCA CAC GGT ACC-3' (Eurofins Genomics).

PCR reaction mixture	Volume in µl
DNA	2
Primer 1 (10 µM)	2
Primer 2 (10 µM)	2
dNTP´s	0.5
5x Buffer	5
Taq Polymerase (GoTaq)	0.125
H_2O	11.375

PCR protocol			
Initial denaturation	95°C	2 min	
Denaturation	95°C	30 s	
Annealing	59°C	30 s	40 cycles
Elongation	72°C	40 s	
Final elongation	72°C	5 min	

3.3.3   Agarose gel electrophoresis

Agarose gel electrophoresis was used to separate DNA fragments of different sizes within a matrix of agarose gel. The gel was made using Agarose (peqGOLD, VWR International GmbH) at a concentration of 2% in TBE buffer (Tris/Borate/EDTA buffer). In addition, PeqGreen (VWR International GmbH) was added for visualization of nucleic acid under UV light. Once the gel had set, it was placed in a horizontal electrophoresis chamber filled with running buffer (TBE buffer), and loaded with DNA samples and a 6x loading-dye (Thermo Fisher Scientific). For migration and separation of DNA, a voltage of 130 - 180 V was applied. DNA bands were visualized using a molecular imager (GelDoc 2000, Bio-Rad), and amplicon sizes were determined using a 1 kb GeneRuler Plus ladder (Thermo Fisher Scientific). Transgene band (HCN4 FEA): 450 bp and WT: 350 bp.

3.4   Optical mapping of action potentials in cardiac tissue

A protocol to measure optical action potentials (OAP) in cardiac tissue was established in cooperation with the group and laboratory of Professor Dr. Igor Efimov, Department of Biomedical Engineering, George Washington University, Washington DC, in particular by assistance of Jaclyn Brennan. The procedure to optically measure transmembrane voltage changes in cardiac tissue is described in detail in chapter 4.1. Briefly, the experimental setup consisted of an optical mapping system, instruments for electrical recordings and a perfusion system. Electrical recordings were performed in parallel with the optical measurements to determine HRV parameters and to trace the beating rate of the cardiac tissue over the entire experimental procedure. A perfusion system was employed to supply the cardiac tissue with Tyrode solution, a physiological electrolyte solution and to maintain a temperature of 37°C. Attention was paid to the aortic pressure measurement during perfusion of the heart in order to keep the pressure within a range of 70 ± 10 mmHg to simulate physiological perfusion via the cardiovascular system. Detailed setup data are presented in chapter 4.1.1.

3.4.1   List of materials

Reagents	Source
(±)-Blebbistatin	Cayman Chemical Company
Calcium chloride dihydrate	Merck KGaA
Carbamoylcholine chloride	Merck KGaA
D(+)-Glucose monohydrate	Carl Roth GmbH + Co. KG
Di-4-ANEPPS	Merck KGaA
Dimethyl sulfoxide	Carl Roth GmbH + Co. KG
Heparin sodium 5000	Ratiopharm GmbH
Isoflurane	CP-Pharma H.-Ges mbH
Magnesium chloride hexahydrate	Carl Roth GmbH + Co. KG
Mucasol®	Schülke & Mayr GmbH
Potassium chloride	Merck KGaA
Sodium chloride	Merck KGaA
Sodium dihydrogen phosphate monohydrate	Carl Roth GmbH + Co. KG
Sodium hydrogen carbonate	PanReac AppliChem
Dissecting set	Source
Blunt dissecting scissors	Fine Science Tools (FST, cat. no. 14078-10)
Blunt forceps	Standard Pattern Forceps (FST, cat. no. 11000-13)
Fine forceps	Dumont no. 5 forceps (FST, cat. no.11251-20)
Fine scissors curved	FST, cat. no. 14061-09
Minutien pin (diameter 0.1 mm)	Fiebig Lehrmittel
Tungsten carbide scissors straight	FST, cat. no. 14568-12

| Vannas spring scissors Straight; 2.5 mm blades | FST, cat. no. 15000-08 |
| Vannas spring scissors straight; 8 mm blades | FST, cat. no. 91500-09 |

Optical mapping setup	Source
Beam splitting system	DLFLSP2R, SciMedia, Brainvision Inc.
Camera Lens Adaptor	SciMedia, Brainvision Inc.
Condenser lens	M5095+AD, SciMedia, Brainvision Inc.
Dichroic mirror (50 x 70 mm)	SciMedia, Brainvision Inc.
Emission filter long pass (> 600 nm)	SciMedia, Brainvision Inc.
Excitation filter bandpass 531/40 nm	BrightLine®, SciMedia, Brainvision Inc.
Fiber optic light guide	SciMedia, Brainvision Inc.
Focus drive	SciMedia, Brainvision Inc.
Halogen lamp 150 W	MHAB-150W, Moritex
MiCAM05 Processor	SciMedia, Brainvision Inc.
MiCAM05 Ultima	SciMedia, Brainvision Inc.
Objective 1.6 x, Plan Apo	Leica Microsystems, SciMedia
Objective nosepiece for 2 objectives	SciMedia, Brainvision Inc.
Shutter controller	SSC-2, SciMedia, Brainvision Inc.

Perfusion system	Source
Aortic cannula	Custom-made
BP Transducer, MLT1199	ADInstruments
Bubble trap	Radnoti Ltd
Heating coil, 5.5 ml	Radnoti Ltd
In line Luer Injection Port	Ibidi®
Peristaltic pump MINIPLUS 3	Gilson
Prep. tissue bath	Radnoti Ltd
Stereomicroscope Stemi 2000	Carl Zeiss
Syringe filter sterile 10 µm	PALL Life Sciences
Temperature controller, ML312	ADInstruments
Thermocirculator Lauda A100	Lauda-Brinkmann
Tubing Tygon®, E3603	Carl Roth GmbH + Co. KG

Other	Source
Needle electrodes, MLA1213	ADInstruments
Pacing electrode Ag/AgCl	Custom-made
Stimulator Cable, MLA260/L	ADInstruments
Stimulus Isolator, FE180	ADInstruments
Silk fibre non absorbable 7/0, 0.5 metric,	Resorba Medical

Data acquisition and analysis	Source
Animal Bio Amp (ECG amplifier), FE136	ADInstruments
Bridge AMP (Pressure amplifier), FE221	ADInstruments
BV_Ana, analysis software	Brainvision Inc.
Labchart 8	ADInstruments

MATLAB R2015b	MathWorks
MiCAM05 data acquisition software	Brainvision Inc.
PowerLab 8/35, PL3508/P	ADInstruments
Rhythm MATLAB GUI 2012	Laughner et al., 2012 [80]

Reagent setup	Instruction
Tyrode solution	Dissolve 128.2 mM NaCl, 4.7 mM KCl, 1.05 mM $MgCl_2$, 1.3 mM $CaCl_2$, 1.19 mM NaH_2PO_4, 20 mM $NaHCO_3$ and 11.1 mM Glucose. Adjust the pH by oxygenation with carbogen (95% O_2, 5% CO_2) to 7.35 ± 0.05.
Blebbistatin stock solution	Dissolve ±blebbistatin in dimethyl sulfoxide (DMSO) to a concentration of 10 mg/ml. Aliquots of 20 µl are stored at -20°C.
Blebbistatin solution	Dilute 20 µl of blebbistatin stock solution with 1 ml of prewarmed (37°C) Tyrode solution
Di-4-ANEPPS stock solution	Dissolve Di-4-ANEPPS in DMSO to a concentration of 1.25 mg/ml. Aliquots of 30 µl are stored at -20°C.
Di-4-ANEPPS solution	Dilute 30 µl of Di-4-ANEPPS stock solution with 1 ml of prewarmed (37°C) Tyrode solution

3.4.2 Preparations of cardiac tissue used for optical mapping

In order to perform optical mapping experiments of cardiac tissue, three types of preparations were utilized: (1) intact whole hearts, (2) isolated biatrial SAN preparations and (3) isolated biatrial SAN preparations containing the intact right vagus nerve. Female mice at the age of 12 ± 2 weeks were utilized for all experiments. To avoid blood clotting in the coronary arteries, mice were injected intraperitoneally with heparin (100 IU/kg) 10 min prior to the experiment. Mice were anesthetized using 5% isoflurane in carbogen (95% O_2, 5% CO_2) and sacrificed by cervical dislocation.

(1) Intact whole hearts

For dissection of intact whole hearts (Langendorff hearts), mice were placed in a supine position to perform a mid-sternal incision. The rib cage was then opened to remove the heart while preserving a substantial part of the aorta and the SVC. To avoid damaging or stretching the heart and vessels, the heart was excised by fixation at the thymus and cutting cardiac blood vessels and midsternal tissue *en bloc*. The heart was immediately placed in oxygenated, pre-warmed (37°C) Tyrode solution and cannulated rapidly (<5 min post mortem).

For cannulation of the heart, the ascending aorta was identified and a custom-made cannula was introduced in the vessel, so that the tip of the cannula was just above the aortic valve. The cannula had two circular notches at a distance 1 and 2 mm from the tip, permitting the aorta to be tied to the cannula with silk suture material. Aortic pressure was detected continuously by a pressure transducer (BP transducer, ADInstruments). The heart was perfused retrogradely via the coronary arteries by applying a constant aortic pressure of 70 ± 10 mmHg. Following cannulation of the heart, the lung and thymus were dissected and removed. It was also necessary to dissect free the preparation from fat tissue and to shorten the remaining pulmonary vessels to obtain noiseless optical measurements of the SAN. The Langendorff heart was continuously perfused (aortic pressure 70 ± 10 mmHg) and superfused (20 ml/min). ECG traces were recorded (Labchart8, ADInstruments) by placing three needle electrodes close to the isolated heart in an approximate Einthoven I configuration.

(2) Isolated biatrial SAN preparations

For biatrial SAN preparations, the heart was isolated and cannulated as described previously for Langendorff heart preparations. Subsequently, the heart was removed from the perfusion cannula and the ventricles were pinned to the silicone (Sylgard® 184) coated floor of the superfusion chamber. It was pinned in a position to give access to the anterior site of the heart, first of all to remove the ventricles, and secondly to open the right atrium (RA). This was achieved by cutting the tricuspid valve along the axis of the SVC and making a second incision along the medial limb of the crista terminalis (CT). The atrium was subsequently opened, flattened, and pinned to expose the endocardial side of the RA and the SAN. To open the left atrium (LA), a cut through the mitral valve towards the LA appendage was performed. A second cut through the anterior atrial free wall was performed to open the LA. The interatrial septum (IAS) was partially removed to reduce scattering of the optical signal. The resulting specimen provided access to the SAN, located between the SVC, the inferior vena cava (IVC), the RA, LA and the atrio-ventricular junction (AVJ) (Fig. 5). Three needle electrodes were placed around the SAN explant in order to perform ECG recordings. Optical mapping measurements were performed as described in the result section 4.1. In order to identify the maximum shift of the leading pacemaker upon parasympathetic activation mediated by carbachol application, 1 µM carbachol was delivered through the perfusion system for 5 - 7 min until steady state was reached. ECG data (Labchart8, ADInstruments) was used to calculate the average beating rate for a 1 min recording under basal conditions and during steady-state of the carbachol effect.

In addition, standard deviation of the NN interval (SDNN) and root mean square of the successive differences (RMSSD) were calculated for heart rate variability (HRV) analysis.

$$SDNN = \sqrt{\frac{1}{n-1}\sum_{i=1}^{n}(NN_i - \overline{NN})^2}$$

$$RMSSD = \sqrt{\frac{1}{n-1}(\sum_{i=1}^{n-1}(NN_{i+1} - NN_i)^2}$$

SDNN describes the total HR variability, whereby RMSSD reflects short-term variations between two successive beats.

(3) Isolated biatrial SAN preparations containing the intact right vagus nerve

The isolation of biatrial SAN preparations with preserved right vagus nerve were performed as described above, with the following modifications. Prior to heart excision, the right vagus nerve was identified close to the right carotid artery in the cervical region of the mouse. For this purpose, a small incision on the right side of the neck was made, the mandibular glands were separated and the right vagus nerve, extending along the right carotid artery was identified. Subsequently the nerve was carefully isolated from adjacent tissue using curved forceps and a silk suture was gently tied around the nerve to mark the position of the nerve during the following preparation steps. The heart was then carefully removed with the intact vagus nerve and mounted onto the perfusion system. Biatrial preparation was performed as described above, although fat tissue had to be removed with extra caution to avoid injury of presynaptic terminals. Three needle electrodes were positioned around the SAN preparation in order to track the beating rate throughout vagus nerve stimulation. The nerve was placed on a custom-made Ag/AgCl stimulation electrode. The experimental procedure is presented in result section 4.1.2.
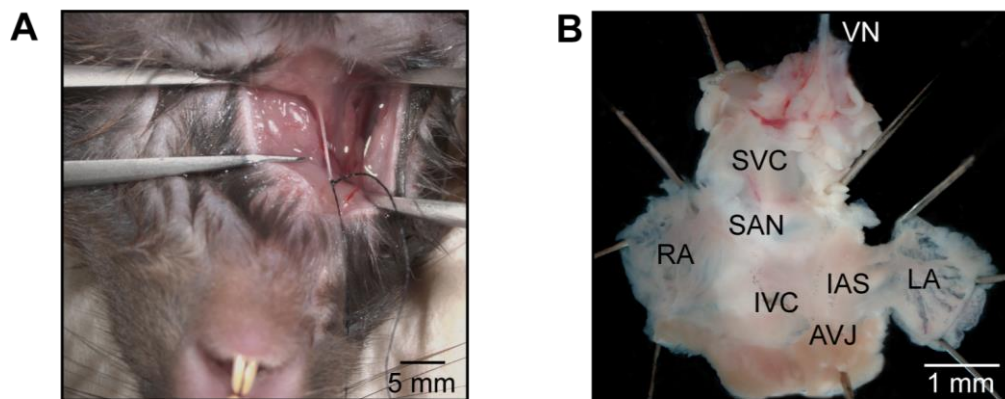
Fig. 5 Biatrial SAN preparation with preserved right vagus nerve. (A) Identification of the right vagus nerve in the cervical region of a mouse. A ligature was made to mark the upper end of the nerve. (B) Photograph of an isolated biatrial SAN preparation used for optical mapping. The preparation was oriented so that the endocardial side faced up to give free access to the sinoatrial node (SAN), the right atrium (RA), the left atrium (LA), the superior vena cava (SVC), the inferior vena cava (IVC), the crista terminalis (CT), the interatrial septum (IAS) and the atrio-ventricular junction (IAS). The right vagus nerve (VN) is preserved within the explant.

3.5   Functional confocal laser scanning microscopy

3.5.1   Confocal calcium imaging of whole mount SAN explants

Intact SAN explants of 12 ± 2 week old female WT and HCN4 FEA mice were prepared as described in chapter 3.4.2 for optical mapping, except that the LA was removed. In addition, the specimen was completely freed from fat tissue and carefully placed in a custom-made Sylgard®-coated superfusion chamber. The explant was pinned with the endocardial side face-up to grant free access to the SAN. Subsequently, the calcium indicator Fluo-4 AM was dissolved in DMSO to a concentration of 2 mM, diluted 1:1 with Pluronic F 127 (13% in H_2O) (Merck KGaA), and added to Tyrode solution to reach an end concentration of 20 µM Fluo-4 AM. The explant was loaded with Fluo-4 AM (Thermo Fisher Scientific) at room temperature (RT) for 45 min. Subsequently; the SAN explant was continuously superfused with oxygenated and warmed (28°C) Tyrode solution containing 0.2 mg/ml of the excitation-contraction uncoupler blebbistatin. To record calcium signals, an upright Leica SP8 confocal microscope with a 20x water objective (HCX APO L 20x/1.00 water, Leica) was used. For excitation, a wavelength of 488 nm was chosen and emission was collected >500 nm by a hybrid detector. Calcium signals from head, body and tail of the SAN explant were recorded. Frames of 443 µm^2 were taken for 10 s with an optically pumped semiconductor laser (OPSL) at a frame rate of 28 frames/s by imaging with a scan speed of 8 kHz. The dimension of each frame was 1024 x 1024 pixels with a pixels size of 0.433 µm. Each frame was scanned in

bidirectional line scan configuration (1024 pixels per line). Every region of the SAN was subsequently examined for cells displaying highly localized and spontaneous calcium release. These cells were counted and normalized to the total surface area measured. Change in fluorescence intensity (ΔF) was assessed after background subtraction, and normalized to baseline fluorescence F_0. Analysis was performed using the Leica LasX image analysis software. Following basal measurements, 15 µM (in Tyrode solution) of TAT-TRIP8b$_{nano}$ (sequence: YGRKKRRQRRRGGNHSLEEEFERAKAAVESTEFWDKMQAEWEEMARR NWISEN, CASLO ApS) [81] a protein that prevents cAMP binding to HCN channels, was added to 4 of the WT preparations. After 30 min incubation, SAN explants were scanned and analyzed as described above.

3.5.2   Confocal voltage sensitive dye imaging of whole mount SAN explants

In order to record the emission spectrum of SAN cell-bound Di-4-ANEPPS in Tyrode solution, intact SAN preparations of 12 week old female WT mice were made as described above for confocal calcium imaging. 10 min after blebbistatin application, the voltage-sensitive dye Di-4-ANEPPS was applied. Di-4-ANEPPS was dissolved in DMSO to a concentration of 1.25 mg/ml, and diluted in Tyrode solution to obtain a final concentration of 37.5 µg/ml. 0.5 ml of Di-4-ANEPPS was slowly applied to the SAN preparation using a 1 ml syringe, and after 5 min incubation, the tissue specimen was continuously superfused with Tyrode solution (28°C). The Leica SP8 confocal microscope was used as previously described (chapter 3.5.1) to record the emission in a range of 500 - 750 nm. The software mode xyλ was chosen to scan the SAN explant in steps of 10 nm with a 5 nm overlap using an excitation wavelength of 488 nm.

3.6   Immunohistochemistry

In order to immunostain SAN explants for HCN4 proteins, female WT mice at an age of 12 weeks were used. SAN preparation was performed as described in chapter 3.4.2, with the following alterations. Prior to heart removal, small incisions into the liver were made to exsanguinate the mouse, reducing the blood volume in the circulatory system. To completely free the heart from blood, it was perfused via the left ventricle (LV) and right ventricle (RV) with phosphate buffered saline (PBS) at RT, and subsequently it was excised from the animal. Following SAN preparation, the tissue was fixed with 4% paraformaldehyde (PFA) in PBS for 25 min, washed with PBS for 10 min and incubated in immunohistochemistry (IHC) permeabilization solution (79.75% PBS, 19.75% DMSO, 0.5% Triton X-100) for 1.5 h on a rotary shaker.

After washing three times with 10 ml PBS, non-specific antibody binding sites were blocked by incubation for 1 h in 5% normal donkey serum in PBS. This was followed by another three washing steps and subsequent overnight incubation at 4°C with guinea pig anti-HCN4 antibody (αHCN4gp, Alomone labs) (1:200 in PBS). The SAN explants were washed three times with PBS before incubation with FITC-conjugated donkey anti-guinea pig secondary antibody (Merck KGaA) (1:100 in PBS) at RT under exclusion of light for 4 h. Tissue was washed with PBS, placed on a microscope slide, mounted with mounting medium (Vectashield, Vector Laboratories), and scanned using a Leica SP8 confocal microscope with 10 x magnification. FITC was excited by a wavelength of 488 nm and emission was collected in a wavelength range of 500 - 600 nm, displayed in green.

3.7   Combined telemetric ECG and blood pressure recordings

Combined telemetric ECG and BP transmitters (HD-X11, Data Sciences International) were implanted in 4 months old male HCN4 FEA (n = 11) and WT (n = 9) littermates. These devices permit simultaneous ECG, arterial BP, subcutaneous body temperature and animal activity recordings. A detailed description of the implantation is provided in the result section 4.2.1 of the present work.

3.7.1   List of materials

Reagents	Source
Acepromazine maleate (Calmivet® Solution Injectable)	Vetoquinol AG
Atropine sulfate	Merck KGaA
Carprofen (Carprieve®)	Norbrook
Ketamine hydrochloride	Medistar
Propranolol hydrochloride (±)	Merck KGaA
Sodium chloride solution 0.9% sterile Miniplasco Connect 5 ml	B. Braun Melsungen AG
Xylazine (Xylariem®)	Ecuphar GmbH
Transmitter implantation devices	Source
Blunt dissecting scissors	Fine Science Tools (FST, cat. no. 14078-10)
Cotton Tipped Applicator sterile	Puritan Medical products
Forceps - Micro-Blunted Tips	Dumont (FST, cat. no.11253-25)
Forceps straight	Semken (FST, cat. no. 11008-13)
Homothermic blanket system with flexible probe	Harvard Apparatus
Hot bead sterilizer	FST, cat. no. 18000-45
Needle holder, Halsey	FST, cat. no. 12501-13
Needle holder, Olsen-Hegar	FST, cat. no. 12002-14

Needle single use No. 17, 0.55 x 25 mm	B. Braun Melsungen AG
Needle single use No. 20, 0.40 x 20 mm	B. Braun Melsungen AG
Needle-suture combination, sterile, absorbable (6-0 USP, metric 0.7, braided)	Resorba Medical
Needle-suture combination, sterile, silk (4-0 USP, metric 1.5, braided)	Resorba Medical
Povidone-Iodine hydrogel 10%	Ratiopharm GmbH
Sensitive plasters, Leukosilk®	BSN medical GmbH
Surgibond® tissue adhesive	SMI AG
Suture, sterile, silk, non-needled (5-0 USP, metric 1 braided)	Resorba Medical
Syringe 1 ml sterile Injekt-F	B. Braun Melsungen AG
Trimmer, Wella Contura type 3HSG1	Procter & Gamble
Vessel Cannulation Forceps	FST, cat. no.18403-11
Data acquisition and analysis	Source
DSI Data Exchange Matrix	Data Science International
DSI Dataquest ART 3.1	Data Science International
DSI PhysioTel HDX-11 for mice	Data Science International
DSI PhysioTel receivers RPC1	Data Science International
ecgAUTO v3.3.5.10	EMKA Technologies

3.7.2 Procedure for data acquisition and analysis

Following implantation of the transmitters, mice were allowed to recover for at least 3 weeks before the basal 72 hour-recordings of BP and ECG. The mice were placed in separate housing cages with *ad libitum* access to food and water. In each recording session, the same number of WT and HCN4 FEA mice was included to equally distribute environmental variations. Signals from six mice were recorded simultaneously using the Dataquest A.R.T data acquisition software (Data Sciences International). Transmitters were configured within the software and turned on by magnetic activation. Each housing cage was placed on individual receiver plates. The receiver plates were shielded from electrical interferences using custom-made Faraday cages. All parameters were recorded continuously for 72 hours without external perturbations in a 12 h dark-light-cycle environment. ECG and BP signals were digitized at 1 kHz, whereby activity was sampled at a rate of 0.1 Hz. Intraperitoneal injections of propranolol (20mg/kg in 0.9% NaCl) and atropine (1 mg/kg in 0.9% NaCl) were performed in a separate recording session of 4 hours. Propranolol was injected after 1 hour prerun whereby atropine was injected 20 min later.

Data analysis was performed using the ecgAUTO v3.3.5.10 software (EMKA Technologies). For baroreceptor sensitivity analysis, a 3 hour-recording during low activity of the mice was

analyzed. The related sequence method, established for the present thesis is described in detail in the result section 4.2.3. ECG and HRV analysis was carried out as previously described [3]. Mean, minimum and maximum heart rates (HR) were evaluated from continuous recordings over 72 hours. Histograms to determine differences in HR dynamics were calculated from 72 hour-recordings. HR values were binned using 50 equally distributed sections of 16 in a range from 150 to 950 bpm. To investigate data for HR fluctuation characteristics frequency domain analysis and time domain analysis were applied. For frequency domain analysis, HR fluctuations in three frequency ranges, named very-low-frequency band (VLF 0.0 - 0.4 Hz), low-frequency band (LF 0.4 - 1.5 Hz) and high-frequency band (HF 1.5 - 4.0 Hz) were determined by spectral analysis. For each mouse, three raw ECG strips of 103 s during stable sinus rhythm were plotted as RR tachograms and interpolated by third degree spline interpolation at 50 ms intervals. This provided equally spaced points for the following Fast Fourier Transformation (FFT). After detrending the data, FFT was performed using 1024 spectral points. A Hamming windowing function was applied to avoid spectral leakage. Power spectral density plots were determined, and for each time segment of 103 s, the total power was calculated as the integral sum of total variability over the total frequency range (0.0 - 4.0). In addition, VLF, LF and HF power was obtained for each time segment and averaged. Time domain parameters were obtained by calculating SDNN and RMSSD from three representative RR time series of 10 min during low activity period (see chapter 3.4.2, biatrial SAN preparations). Poincaré plots were created by plotting the RR interval (n) of 20.000 data points against their successive RR interval (n+1).

3.8   Data analysis and statistics

All data are displayed as mean ± SEM unless otherwise stated. N represents the number of animals or preparations. For all statistical tests, $p<0.05$ was considered statistically significant (***$p<0.001$, **$p<0.01$, *$p<0.05$). Data analysis was performed using OriginPro8 (OriginLab Corporation). Differences between groups were analyzed by Student´s unpaired two-sampled t-test.

4   Results

In the present thesis the role of cAMP-dependent regulation (CDR) of HCN4 channels on SAN activity was characterized using a multilevel cardiophysiological analysis. Within this context, two new methods were established, namely optical recordings of action potentials and combined ECG and BP telemetry. These methods were utilized to examine the phenotype of HCN4 FEA mice.

4.1   Optical mapping of action potentials in cardiac tissue

High-resolution optical mapping of transmembrane voltage changes in cardiac tissue and particularly in the SAN is a method to precisely define electrical processes in the heart. This novel method was established as part of this thesis to characterize the cardiac phenotype, especially on the SAN network level of mice lacking CDR of HCN4. Optical mapping was applied to investigate impulse formation and propagation in HCN4 FEA mouse hearts as well as to define the exact functional anatomy of the SAN after disruption of CDR.

Briefly, optical mapping is a fluorescence imaging technique where tissue is stained with a fast voltage-sensitive probe. It binds to the plasma membrane of cardiac cells and shifts its emission spectrum in response to changes in transmembrane voltage. The changes in emitted fluorescence light intensity collected in a defined wavelength range are proportional to changes in membrane potential[82]. Emitted light intensity was detected by a high-speed camera and translated into action potentials. For interpretation of optical data, the basic element was to calculate the activation times for individual regions of the cardiac tissue. Activation times were then used to create isochronal activation maps for defining the exact pattern of excitation within the heart and the first excitation site within the SAN. Further parameters determined by optically obtained activation times were the sinoatrial conduction time (SACT), the action potential duration (APD) and the conduction velocity (Fig. 6).
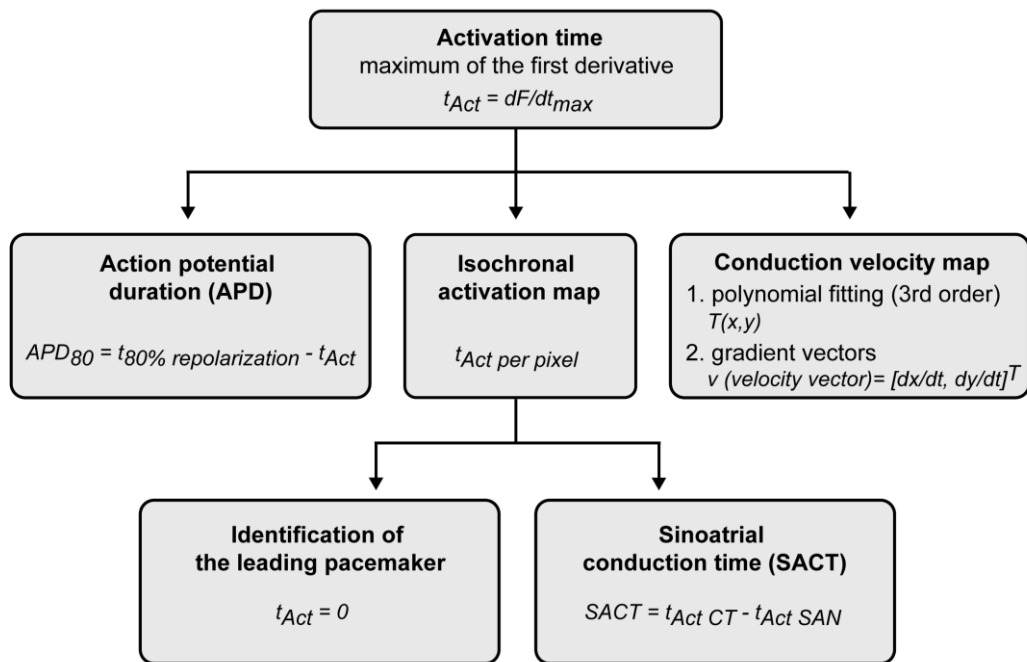
Fig. 6 Parameters determined by optical mapping of cardiac tissue. Activation times (tAct) of individual regions of the tissue preparation are used to calculate the action potential duration (APD), to build isochronal activation maps, and conduction velocity maps. Data derived from activation maps are used to identify the first excitation site, the leading pacemaker within the SAN, and to calculate sinoatrial conduction time (SACT). Further description of the parameters is found in chapter 4.1.4 – 4.1.8.

In the following section the instrumentation setup, the experimental conditions and data analysis found to be appropriate for optical mapping of cardiac tissue in order to phenotype HCN4 FEA cardiac tissue, are explained in detail.

4.1.1 Experimental setup

The experimental setup (Fig. 7) consisted of the optical mapping system (described in chapter 4.1.3), instruments for electrical recordings, and of a perfusion system to supply the cardiac tissue with Tyrode solution, a physiological electrolyte solution. The perfusion system was composed of two peristaltic pumps: one pump was used for retrograde perfusion of the preparation and the second pump was used for superfusion (20 ml/min) of the preparation as well as to return the perfusate back to the holding reservoir passing a 10 µM filter. Tyrode solution was warmed up to 37°C by use of a water jacket and a thermocirculator. In addition, it was oxygenated with 95% O_2 and 5% CO_2 to maintain a pH value of 7.35 ± 0.05 throughout the entire experiment. For cannulation and retrograde perfusion of the heart the perfusate was pumped in a bubble trap, which was equipped with an injection port and was connected to the thermocirculator to maintain constant temperature. The air bubble free solution was then pumped in direction of an aortic cannula used for retrograde perfusion of the heart. The custom-made cannula had two circular notches at a distance of 1 and 2 mm from the tip in

order to mount the heart (described in chapter 3.4.2). Aortic pressure was monitored using a pressure transducer installed in-line with the perfusion system and the cannulated heart. The pressure was kept at 70 ± 10 mmHg by adjusting the flow rate of the peristaltic pump. In order to constantly control the beating rate of the heart, sensing electrodes were placed close to the preparation. The obtained electrical recordings were further used to directly compare the electrical deflections with simultaneously measured optical signals.
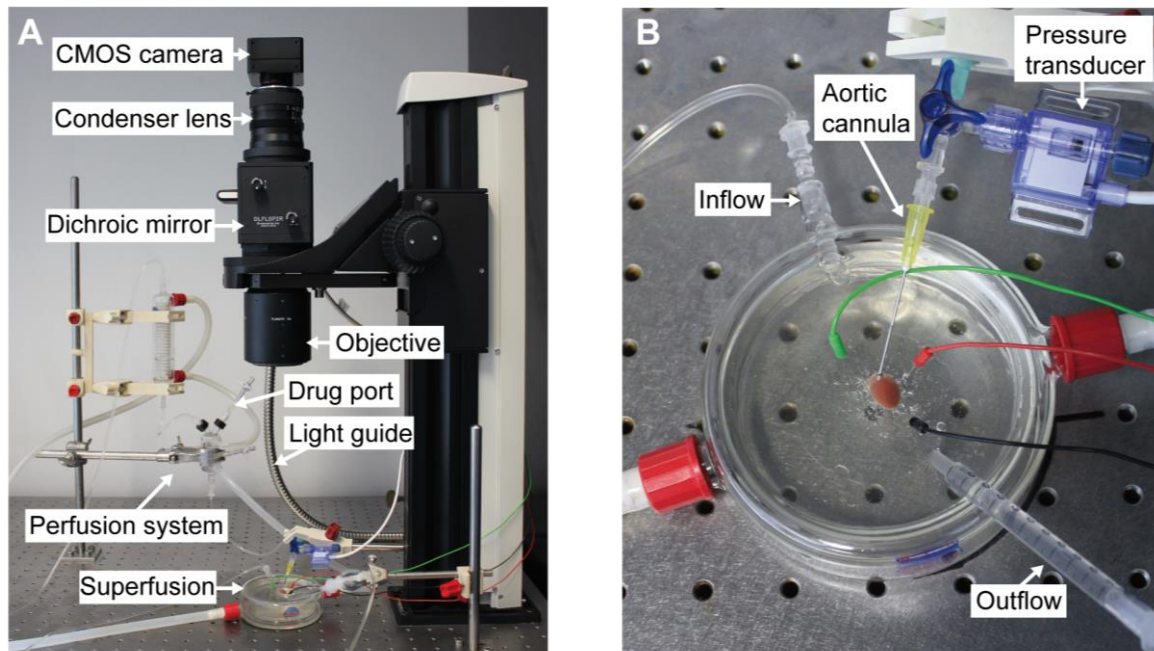
Fig. 7 Experimental setup for optical mapping and perfusion of cardiac tissue. (A) The photograph shows the set-up of the perfusion and superfusion system as well as the imaging system. Peristaltic pumps and the buffer holding reservoir are omitted for better visibility. (B) Cannulated and retrogradely perfused mouse heart in a superfused heating chamber. A pressure transducer is installed in-line with the perfusion system and the aortic cannula. Electrodes are placed close to the preparation for electrical recordings.

4.1.2 Experimental procedure

The following chapter provides a detailed description of the experimental procedure found to be appropriate for optical mapping of cardiac tissue.

First of all, an appropriate dye to measure membrane potentials in cardiac tissue had to be found. Two commonly used dyes, Di-4-ANEPPS and RH237 were tested for the present study. Di-4-ANEPPS is excited by wavelengths in a range of 370 - 570 nm (Fluorophore specifications, Thermo Fisher scientific) and the emission peak of cell-bound Di-4-ANEPPS is located at approximately 590 nm (determined by confocal measurements Fig. 8). RH237 is excited by wavelengths in a range of 400 – 680 nm and the emission peak appears at approximately 700 nm [83]. Fig. 8 shows the emission spectrum of cell-bound Di-4-ANEPPS.

Di-4-ANEPPS shows a higher signal quality, a faster staining rate, and lower phototoxicity compared to RH237. The internalization rate of Di-4-ANEPPS into the cytoplasm is slightly higher compared to other voltage-sensitive dyes, like Di-8-ANEPPS and RH795 [84]. However, the time before internalization of Di-4-ANEPPS was found to be sufficient for short-term experiments. In addition, Di-4-ANEPPS can be readout in a ratiometric manner and therefore could be used in future experiments for simultaneous calcium fluorescence imaging.
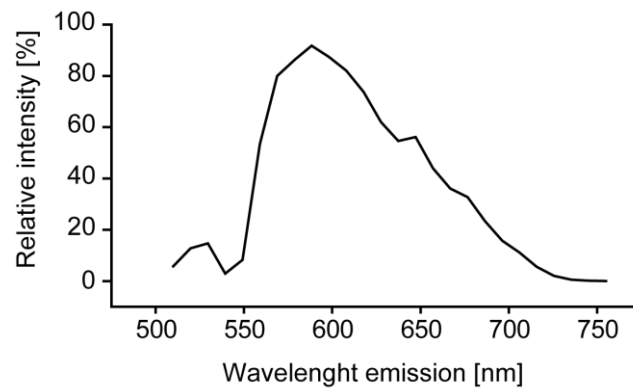
Fig. 8 Emission spectrum of cell-bound dye Di-4-ANEPPS. Confocal microscopic measurement of the emission wavelength range in a SAN preparation loaded with Di-4-ANEPPS. Excitation wavelength 488 nm.

In a next step, an excitation-contraction uncoupler to avoid motion artifacts during voltage-sensitive dye imaging had to be chosen. The uncoupler blebbistatin is recommended for cardiac electrophysiological measurements due to the absence of side effects on the electrical activity of the heart. Other pharmacological uncouplers like 2,3-butanedione monoxime and cytochalasin D show additional effects on intracellular calcium handling, ion channel kinetics, and action potential characteristics. Blebbistatin is an inhibitor of the nonmuscle and skeletal myosin II isoform and therefore lowers the affinity of myosin II to actin. Two limitations of blebbistatin are that it is highly photosensitive and is prone to precipitate in aqueous media [66,85]. Warming blebbistatin prior to dissolving it in Tyrode solution was found to minimize precipitation.

To perform optical experiments Tyrode solution was freshly prepared, oxygenated, and warmed to 37°C. In the meantime, the perfusion system was first cleaned for 20 min using 2% mucasol®, an alkaline cleaning agent, and second washed with 1 l of deionized water. Subsequently, 500 ml and 300 ml of freshly prepared Tyrode solution were circulated in the perfusion system for whole heart measurements and for biatrial SAN measurements, respectively. The solution was continuously warmed and oxygenated. Temperature was monitored (ADInstruments, Labchart) and the flow rate of the peristaltic pump for superfusion of the preparation was set to 20 ml/min.

Optical mapping of intact whole hearts

Intact whole heart optical recordings were made to create isochronal activation maps and to characterize observed arrhythmias. The heart was cannulated as described in chapter 3.4.2 and was mounted to a Langendorff system to be continuously perfused and superfused with Tyrode solution as described above. 15 min after cannulation, 1 ml of blebbistatin solution was slowly injected into the bubble trap via a drug port over a time of 5 min. From that moment on, work space had to be kept in dark to avoid photo deactivation of the substance. After equilibration for 5 min, 1 ml of Di-4-ANEPPS solution was applied via the same port. 10 min poststaining, optical recordings of the anterior and posterior side of the heart were performed using a sampling rate of 2 kHz, a frame number of 8192 and a spatial resolution of approximately 100x100 µm/pixel. According to this, one optical recording had a duration of 4.096 s. Over the course of the optical recordings, the Langendorff heart should be completely covered with Tyrode solution and the superfusion should be turned off to avoid motion artifacts. For whole heart measurements it was of importance to avoid air bubbles in the perfusion system. Air bubbles in the coronary vessels prevent proper heart perfusion and additionally lead to insufficient loading of the preparation with fluorescent dye.

Optical mapping of isolated biatrial SAN preparations

Biatrial SAN preparations were mapped to create isochronal activation maps, to calculate SACT and to identify the location of the leading pacemaker. These parameters (see chapter 4.1.4 to 4.1.8) provide detailed information about pacemaker cell function within the intact SAN network. SAN preparations were performed as described in chapter 3.4.2. The specimen was placed in a silicone (Sylgard®) coated heating chamber, fixed with small pins, and was continuously superfused as described above. Electrical recordings were performed simultaneously and were used to analyze the beating rate and the corresponding beating rate variability parameters. Prior to the optical experiment, the SAN preparations were equilibrated in Tyrode solution for 15 min. In a next step, 1 ml of blebbistatin solution was slowly spread on the SAN explant using a 1 ml syringe. During this procedure and for an incubation time of 5 min the superfusion pump was turned off. 10 min after excitation-contraction uncoupling, 0.5 ml of Di-4-ANEPPS solution was applied in the same way as blebbistatin. The SAN preparation was stained by fluorescence dye for 5 min followed by provisional optical recordings to examine the quality of staining. If required, additional Di-4-ANEPPS application was performed. The settings for optical mapping of biatrial SAN preparations were similar to those described for whole heart measurements. During the optical recordings superfusion should be turned off to avoid motion artifacts. For localization of the leading pacemaker, 5 consecutive optical recordings with a time delay of 1 s were made three times, in an interval of 5 min. Location of the first activation site within the SAN was examined for each OAP of the 15 files.

Optical mapping of isolated biatrial SAN preparations containing the intact right vagus nerve

Optical recordings of biatrial SAN preparations containing the intact right vagus nerve (preparation is described in chapter 3.4.2) were performed as described above with the following alterations. After basal measurements the vagus nerve was placed on a custom-made Ag/AgCl electrode. For this purpose it was essential that the SAN preparation possessed a substantial part of the nerve (>8 mm). This was achieved in advance by dissection of the nerve from the rib cage up to the cervical region of the mouse (described in detail in chapter 3.4.2). The electrode was positioned out of the superfusion solution to ensure conduction of the stimulus to the vagus nerve and to prevent electrical interferences of the stimulation signals to the electrical ECG recordings. Ag/AgCl electrodes were chosen for right vagus nerve stimulation in SAN explants due to its convenient handling and its small size of the silver wires (0.2 mm diameter). Another option was the usage of custom-made nerve cuff electrodes, however, this required an extra long part of the nerve. Furthermore, concentric bipolar electrodes were tested, but appeared to be inappropriate by reason of their size and difficulties in placement of the nerve. Vagus nerve stimulation parameters were set to 4 V, 1 ms pulse width, and 20 Hz for 30 s. These parameters were found to be optimal, since an applied voltage of 4 V was low enough to not injure the nerve and a stimulation frequency of 20 Hz was appropriate to observe an adequate parasympathetic effect on the beating rate of the SAN explant. A frequency of 30 Hz appeared to be too high because it led to a complete interruption of the heartbeat. A break of at least 1 min between two pacing cycles was essential for recovery of the heart preparation.

In order to combine vagus nerve stimulation with optical mapping, 5 consecutive optical recordings (time delay of 1 s) were performed before, during, and after vagus nerve stimulation. Data were used to identify the location of the maximum shift of the leading pacemaker. The distance to the leading pacemaker site under basal conditions was calculated and normalized to the size of the preparation.

4.1.3 Optical mapping system

The optical recording system (Fig. 9) was built on a vibration isolation table in a room that can be shielded from light. It consisted of a high-speed camera (MiCAM05 Ultima, SciMedia) equipped with a CMOS (Complementary Metal-Oxide Semiconductor) sensor. A temporal resolution of 2000 frames/s was selected for measurements of action potentials in the murine heart. The spatial resolution of the camera was 100 x 100 pixels with a pixel size of 100 x 100 µm and could further be increased by an adjustable condenser lens and a 1.6 x objective. The excitation light was generated by a 150 W halogen lamp, passed through a 531/40 nm bandpass excitation filter and was directed in a beam splitter. There, the dichroic mirror directed the light beam through a 1.6x objective onto the sample, loaded with Di-4-ANEPPS.
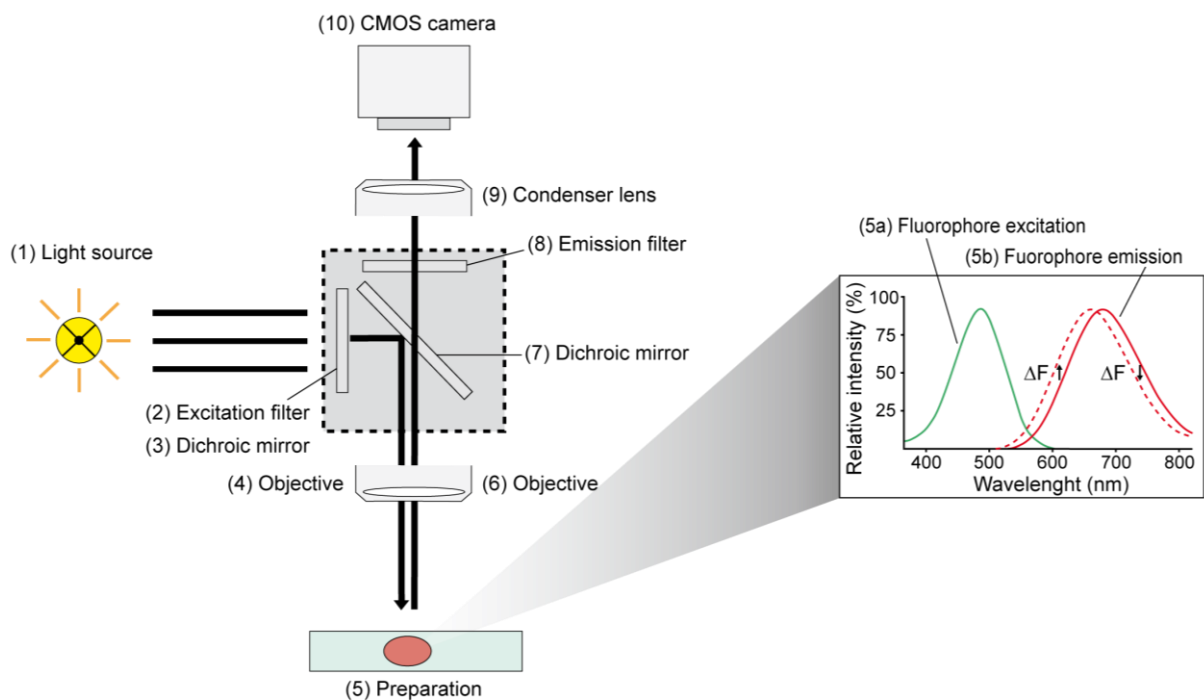
Fig. 9 Schematic illustration of the optical recording system. The excitation path (1-5a) consists of a light source (1), an excitation filter (531/40 nm bandpass) (2), a dichroic mirror which reflects the excitation light (3), a 1.6x objective (4) and the excitation spectrum of the voltage-sensitive dye (5a) in the cell membrane of the preparation (5). The emission path (5b-10) consists of the emission spectrum of the fluorophore (5b), the 1.6x objective (6), the dichroic mirror which transmits the emission light (7), an emission filter (600 nm long pass) (8), a condenser lens (9) and the detector (CMOS camera) (10). Spectrum of unbound Di-4-ANEPPS in methanol (right). Spectrum according to Thermo Fisher Scientific fluorophore specifications.

The excitation wavelength in the green spectral range led to the dye´s emission spectrum at longer wavelengths with a maximum at 590 nm. Voltage-sensitive dyes shift their emission fluorescence based on the membrane potential. Depolarization of the tissue led to a spectral

shift in direction of shorter wavelengths. A voltage change of +100 mV leads to a shift of 2 - 5 nm in direction of shorter wavelengths [86]. The emission signal was passed through the dichroic mirror, a long pass emission filter (> 600 nm) and was collected by the detector (CMOS camera). Acquired fluorescent signals were then digitalized, amplified, and visualized by a custom software (SciMedia, BVAna).

The detector quantified the amount of emitted fluorescent light per pixel for wavelengths above 600 nm. The detected light intensity corresponds to the area under the emission spectrum curve (Fig. 10), thereby, a shift of the emission spectrum to shorter wavelengths due to a positive change in membrane potential led to a decrease in light intensity. Repolarization of the membrane potential shifted the spectrum back in direction of longer wavelengths and thus led to an increase in recorded light intensity. Therefore, the sampled fluorescence intensity correlates directly with changes in transmembrane voltage. The relative signal change is up to 10% per 100 mV [55]. Data were recorded at a sampling frequency of 2 kHz in form of series of matrices. Each pixel of the matrices represents the amount of emitted light for a small group of cardiomyocytes within the tissue at a specific time point. By plotting fluorescence intensity against time, OAPs were generated.
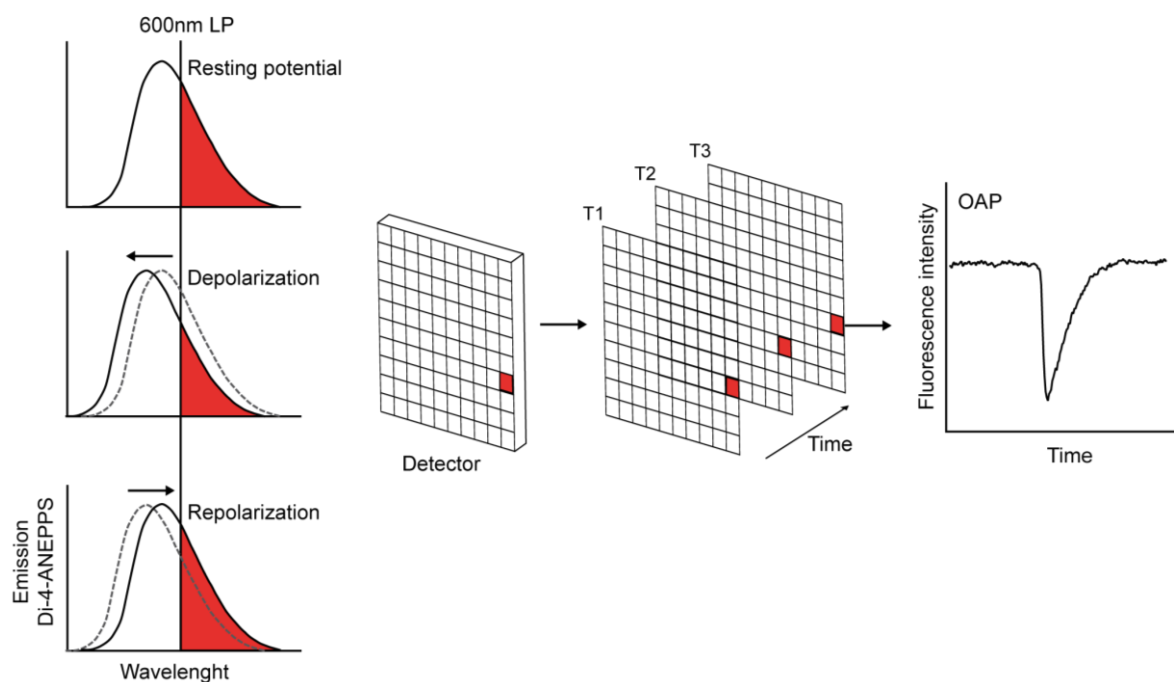

Fig. 10 Functional principle of voltage sensitive dyes and optical action potential acquisition. Emission spectrum of the fluorescent dye Di-4-ANEPPS over the course of an action potential (left). Depolarization shifts the spectrum in direction of shorter wavelengths. Repolarization shifts the emission back to the long-wave range. A longpass filter (LP) of >600 nm is used. The area under the curve of the emission spectrum (in red) represents light intensity that is sampled by the detector. The detector collects fluorescence intensity for each of its multiple pixels at a set sampling frequency to build series of matrices (middle). Optical action potential (OAP) of one specific pixel represents the change in light intensity over time (right). T1 - 3 represent points in time. Figure is adapted from [82].

4.1.4 Signal processing of optical action potentials

A MATLAB[TM] based Graphical User Interface (RHYTHM), programmed and kindly provided by the group of Professor Dr. Igor Efimov (Department of Biomedical Engineering, George Washington University, Washington DC) was used for data processing and analysis [80]. First, OAPs were inverted in order to compare them to action potentials obtained by conventional microelectrode measurements or with electrical recordings of the explant (Fig. 11).
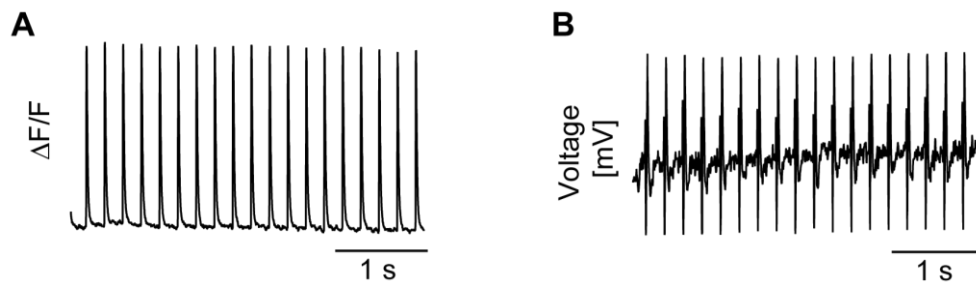

Fig. 11 Representative optical action potentials and the corresponding ECG recordings (A) Inverted OAPs of a recording file of 4.096 s after 3 x 3 pixel binning. Signals were obtained from the RA of a biatrial SAN explant. (B) Corresponding ECG recording monitored during optical mapping.

Second, background fluorescence was automatically subtracted for each pixel. Each single image of the specimen comprises pixels providing relevant fluorescence information and pixels outside of the preparation that contain noise distorting optical data analysis. In order to isolate relevant pixels for further digital processing the image was first segmented by manually cropping the image and second, by applying a threshold criteria. For this purpose, the user defines a threshold value above which a pixel is considered as relevant. In addition, raw data often contained high-frequency noise (>100 Hz) and had to be processed by spatial and temporal filtering (Fig. 12). A common method to improve signal-to-noise ratio is binning. Here, adjacent pixels were combined into 3 x 3 pixel blocks and the average value was computed. Larger bin sizes should be used with caution, because this can remove important features of the OAP.

Signals were then filtered in time domain using a 100th order band pass filter between a user-defined low and high pass band threshold frequency. The high-band of the filter was selected from a drop-down menu in RHYTHM and was set to 100 Hz. In the next step, drift correction was applied to the data. This was required since photo deactivation of the dye or movement of the specimen possibly led to a slight drift of the baseline. In order to obtain a steady baseline, a 1st - 4th order polynomial was fit to the original data and was subsequently subtracted. In the following, the OAPs of each pixel were normalized to a uniform magnitude. Normalized maximum fluorescence of 100% corresponds to a maximally depolarized membrane potential, whereas baseline fluorescence of 0% corresponds to the resting membrane potential.
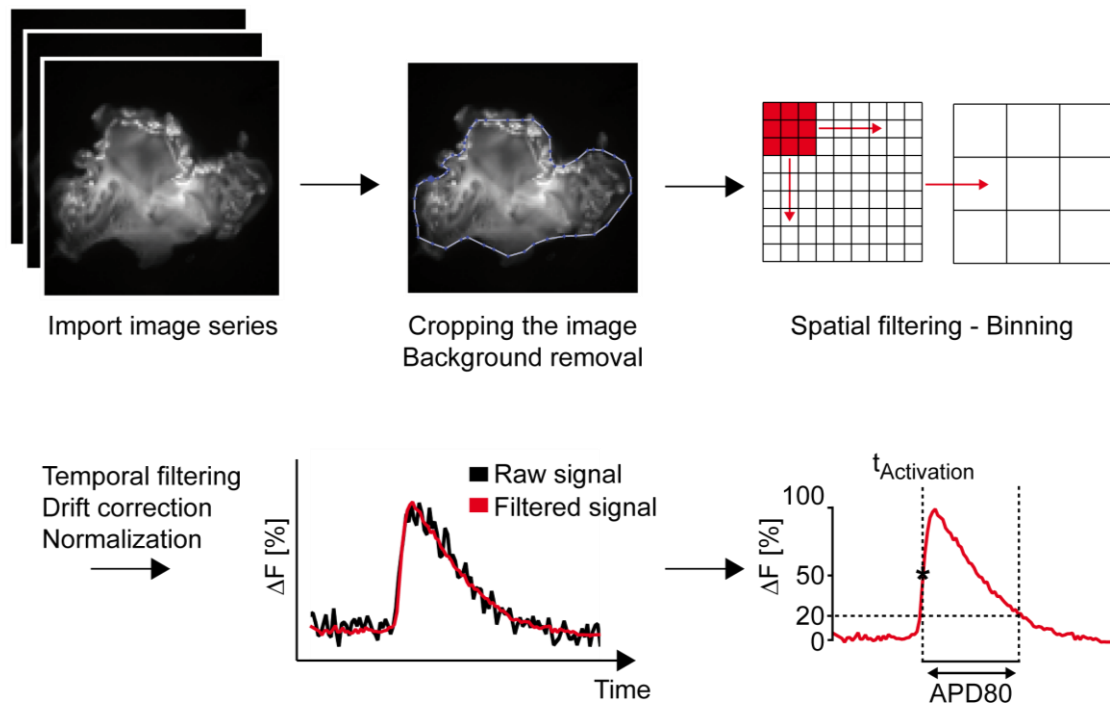
Fig. 12 Digital signal processing using the MATLAB based GUI RHYTHM.Import of the optical data into the software provides a background image of the specimen for better spatial orientation. The area to be examined is cut and background noise is removed by data masking. All relevant pixels are spatially and temporally filtered to improve signal-to-noise ratio. Drift correction and normalization of the data lead to uniform OAPs. Activation times (tActivation) are assigned to all of the pixels for a single action potential propagation. tActivation can be used to define action potential duration (APD) at a repolarization level of, for example, 80% (APD80).

For analysis of the filtered data, the activation time of a single action potential propagation has to be calculated for each pixel (Fig. 12). The activation time is defined as the time of the steepest part of an OAP upstroke and is determined by calculation of the maximum first derivative. To assign the activation times in RHYTHM, the user has to select a time window that encompasses the OAP upstroke of all the pixels within a region of interest. Activation times can be used to create isochronal activation maps and to calculate the action potential duration (APD) per pixel. APD is defined as the duration between the activation time and the time at a defined level of repolarization. In RHYTHM, the user can select between 50%, 80% or 90% repolarization. The time of 80% repolarization (APD80) describes the time where fluorescence intensity is only 20% of its maximum.

4.1.5 Isochronal activation maps

Isochronal activation maps are very convenient to visualize impulse propagation across the cardiac tissue (Fig. 13). Each isochrone depicts the pixels and their associated part of tissue activated at the same time. To create activation maps, a time window that encompasses the OAP upstroke of all relevant pixels was determined. Activation times were calculated and isochrones were built to be represented as colored activation map. The corresponding color time scale (in milliseconds) specified the earliest point of activation (0 ms) in dark blue and the latest activation point in red. In order to determine the origin of activation within the SAN and the activation pattern towards the atria, biatrial SAN preparations were optically mapped during spontaneous pacemaker activity (Fig. 13A-C). The preparation was orientated so that the endocardial side was faced up to give a free view on the SAN. The first activation site, the so called leading pacemaker position within the territory of the SAN, was formed by a small cluster of SAN cells from where the signal was transferred to activate the RA. A block zone was found at the left border of the SAN and two atrial breakthrough points were located along the CT to activate the RA. After complete excitation of the RA, the signal crossed the IAS to subsequently activate the LA.

To investigate the activation pattern of isolated whole hearts (Fig. 13D, E), two separate isochronal activation maps of atrial and ventricular excitation were built for one single heartbeat. The two color time scales for atrial and ventricular excitation showed a time lag between the end of the atrial activation and the beginning of ventricular activation, which corresponds to the atrioventricular transition time (AV delay). The AVN could not be visualized using optical mapping because this method only detects signals of superficial cell layers. Optical recordings of whole hearts were performed from the anterior and posterior site in which ventricular activation was characterized by distinct regions of early activation. The activation maps of anterior positioned hearts showed two breakthrough points on the free walls of the RV and LV, but with the RV activating earlier than the LV. When the posterior site was optically monitored only one breakthrough point was located in the middle of the ventricular surface.
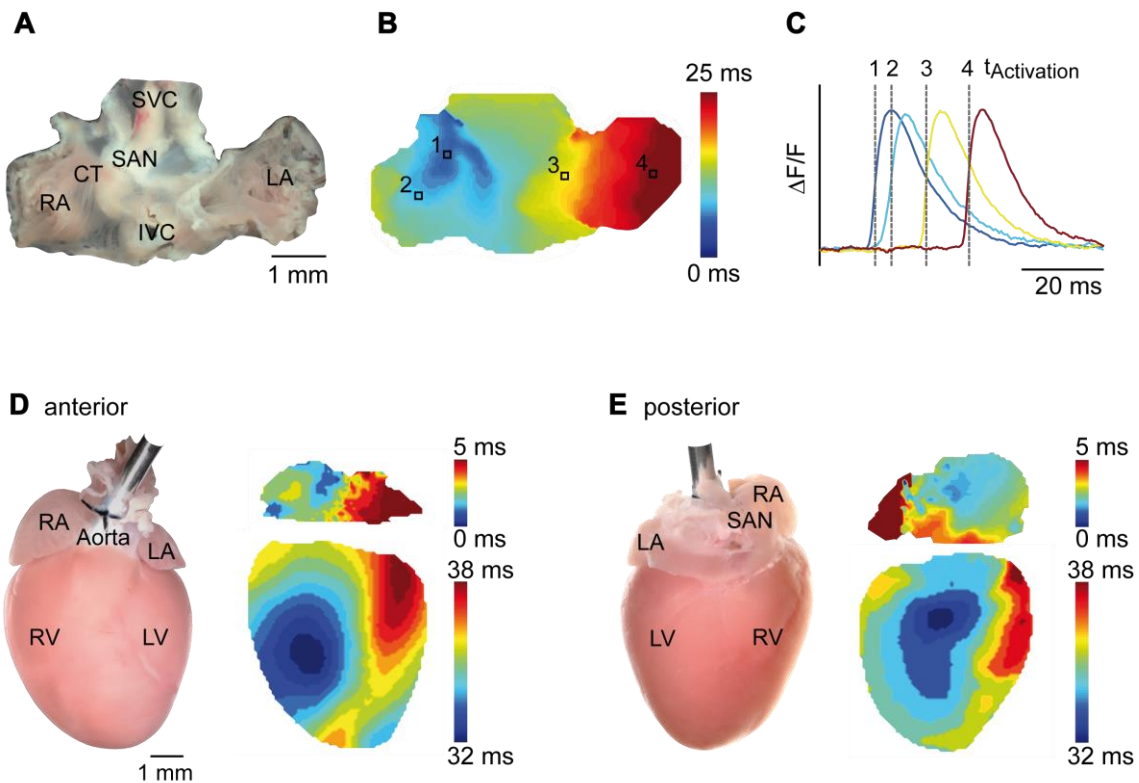
Fig. 13 Isochronal activation maps during spontaneous pacemaker activity. (A) Photograph of a typical biatrial SAN preparation used for optical mapping and (B) the corresponding color contour map. The color time scale (right) indicates the earliest activation point, in dark blue and the latest activation point, in red. Numbers 1 - 4 describe the position of OAPs shown in C. (C) OAPs for 4 regions of interest on the SAN preparation during an AP propagation. Activation times are marked. (D) Isolated Langendorff-perfused heart in anterior and (E) in posterior position with their corresponding activation maps. Two color time scales represent the atrial and ventricular excitation with a time delay of 27 ms representing AV conduction; sinoatrial node (SAN), right atrium (RA), left atrium (LA), right ventricle (RV), left ventricle (LV), vena cava superior (SVC), vena cava inferior (IVC), crista terminalis (CT).

4.1.6 Determination of the leading pacemaker position within the SAN

Optically generated activation maps of biatrial SAN preparations were used to estimate the exact position of the leading pacemaker. The isochrone exhibiting the lowest level, thus representing the first excitation site within the tissue, was identified in RHYTHM. To uniformly plot the location of the leading pacemaker for each preparation the software ImageJ was used. A coordinate grid was placed within a background image captured by the CMOS camera (Fig. 14). The grid was positioned so that the orthogonal axes cross at the IVC. The ordinate was positioned parallel to the CT from superior to inferior direction and the abscissa was running from RA to LA direction. In addition, the coordinates were normalized for each preparation by setting them in relation to the size of the preparation. The XY position of the first excitation site was then plotted and identified within the territory of the SAN. The approximate region of the central SAN was determined by IHC staining of a SAN preparation using an HCN4 channel antibody.
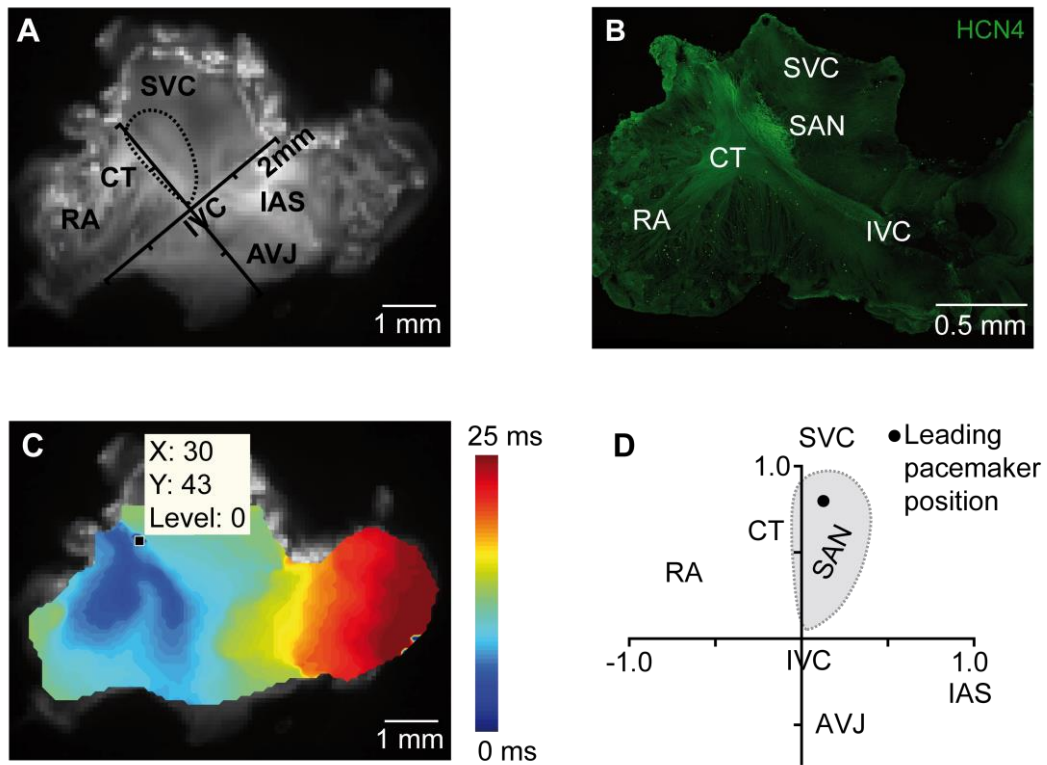
Fig. 14 Identification of the leading pacemaker position within the SAN. (A) Background image of a SAN explant marked with anatomical landmarks. Orthogonal axes crossing at the IVC were used to plot the leading pacemaker position. The ordinate is placed parallel to the CT from superior to inferior direction. The abscissa runs from RA to LA. The dotted line indicates the territory of the SAN. (B) Whole mount immunofluorescence labeling using an HCN4 channel antibody to localize SAN structure (C) Identification of the first activation site by finding the location of the pixel with the lowest level. (D) Illustration of the pacemaker location. The black circle indicates the location of the leading pacemaker within the territory of the SAN (axes are normalized to the size of the preparation). Sinoatrial node (SAN), right atrium (RA), interatrial septum (IAS), atrio-ventricular junction (AVJ), vena cava superior (SVC), vena cava inferior (IVC), crista terminalis (CT).

4.1.7 Sinoatrial conduction time

Sinoatrial conduction time (SACT) describes the transition time from the moment of the leading pacemaker activation to the earliest atrial activation, the atrial breakthrough point. For this purpose, the activation times of both regions were determined and the time interval was calculated (Fig. 15). However, to correctly identify SACT, especially in the very fast beating mouse heart it had to be considered that the OAP of the SAN is composed of two distinct components. The optically mapped SAN signal was always a summation of OAPs recorded over a sandwich of tissue composed of atrial and SAN cells (signal layer depth 0.5 – 2 mm) [7]. Therefore, SAN OAP structure did not exactly correspond with single SAN myocyte recordings but showed an additional component due to interferences of atrial signals. OAPs recorded in the SAN region consisted of a small and slow SAN upstroke followed by a steep upstroke of the atrial signal. Thus, to correctly determine the activation time of the SAN, only the SAN

component of the two-phase OAP had to be included in the calculation. SACT in WT mice during spontaneous pacemaker activity was 4.86 ± 0.37 ms.
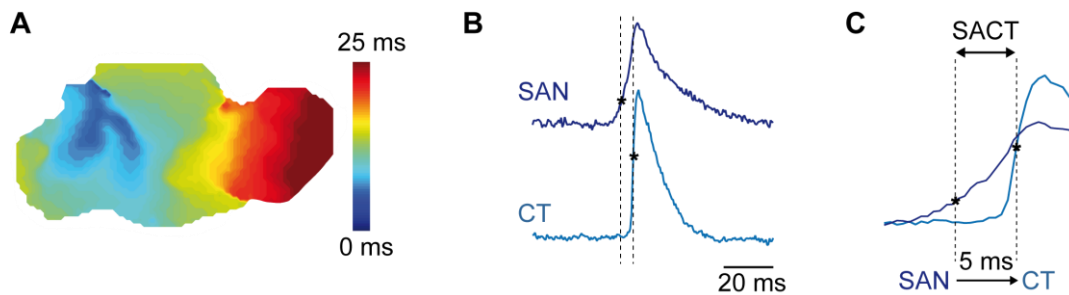

Fig. 15 Determination of the sinoatrial conduction time (SACT). (A) Representative activation map of a biatrial SAN preparation. (B) OAP of the leading pacemaker (SAN) and the atrial breakthrough within the crista terminalis (CT). Activation times are marked (asterisk and dotted line). (C) Magnification of the OAP in B shows the double component of the SAN OAP and an SACT of 5 ms.

4.1.8 Conduction velocity maps

Conduction velocity maps (Fig. 16) represent the rate of an electrical impulse and the direction of impulse propagation within cardiac tissue for a single AP. In order to calculate conduction velocity, the activation time for each pixel is determined and a third order polynomial surface is fitted to the activation data. Next, local velocity vectors are calculated from the gradient of the fitted surface [80]. Data are then represented as a vector field. The lengths of the vectors describe the local conduction velocity; the directions of the vectors describe the direction of activation.
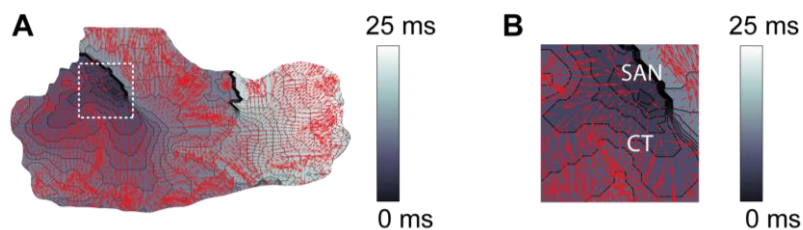

Fig. 16 Conduction velocity map of a biatrial SAN preparation. (A) CV map is a composition of the vector field (red arrows) and the isochronal activation map in grayscale. (B) Magnification of the central SAN region (dotted line from A) shows a block zone of signal transmission towards the septum (in black). Crista teminalis (CT) and SAN region are highlighted.

4.2   Combined telemetric ECG and blood pressure recordings

In order to investigate dynamic interactions between vagus nerve activity and heart function in mice with disrupted CDR of HCN4, combined telemetric ECG and BP recordings were performed. Implantation of the transmitters as well as baroreceptor sensitivity analysis was established for the present study.

HR and BP are both under control of the autonomic nervous system (ANS) and are closely connected to each other because of the baroreceptor reflex. Baroreceptors in the aortic arch and the carotid sinus sense fluctuations of the arterial BP, which has to be maintained within a relatively narrow physiological range. As a result, if BP changes the ANS subsequently starts to adjust the HR to the given conditions by cAMP modulation. To investigate the consequence and degree of the outlined interaction between ANS, BP and HR in HCN4 FEA mice, both HR and BP were recorded simultaneously. This requires the implantation of a transmitter containing 2 ECG leads and a pressure sensor.

4.2.1   Surgical implantation of telemetric transmitters

In order to implant combined telemetric ECG and BP transmitters the following surgical procedure was applied. Before surgery, all instruments were sterilized by dry heat using a glass bead sterilizer. The work bench was disinfected to assure aseptic conditions. Prior to the surgery, each transmitter (Fig. 17A, B) was assigned to a receiver plate (RPC1, DSI) of the Dataquest A.R.T system and the serial number of the transmitter was recorded. The transmitter was then removed from the sterile package and the ECG leads were shortened to a length appropriate for the size of the mouse. For a 12 week-old male mouse, weighing ~30 g, the positive lead (red) was shortened to a length of ~45 mm and the negative lead (colorless) was shortened to a length of ~40 mm. Approximately 6 mm of the silicone tubing was removed from the distal part of each lead to expose the wire. Subsequently, the tips of the electrodes were covered with excessive tubing leaving a ~2 mm portion of ECG wire uncovered to record electrical signals. The tip cover and the silicone tubing proximal to the exposed wire were secured by non-absorbable 5-0 silk suture material (Fig. 17A). During the following steps the transmitter was hydrated in 0.9% NaCl.

The experimental animals were anesthetized with an intraperitoneal injection of 100 mg/kg ketamine (Medistar), 15 mg/kg xylazine (Ecuphar) and 1 mg/kg acepromazine (Vétoquinol) in 0.9% NaCl. The mouse was placed in a supine position on a temperature-controlled surgery plate, which was set to 37°C. Subsequently, eye ointment was applied and fur was removed from the cervical region of the mouse (Fig. 17C). The incision site was disinfected and loss of toe-pinch reflex was confirmed. For better view of the surgical area, a dissecting microscope

(OPMI 1FR pro, Zeiss) was used. A 15 mm midline incision through the skin of the neck was made (Fig. 17D). The mandibular glands were then separated using cotton tip applicators to identify the left carotid artery lateral to the left side of the trachea. After this, the artery was isolated from adjacent tissue, using curved forceps (Fig. 17E, F). This had to be done with caution to not injure the vagus nerve which is running along the vessel.
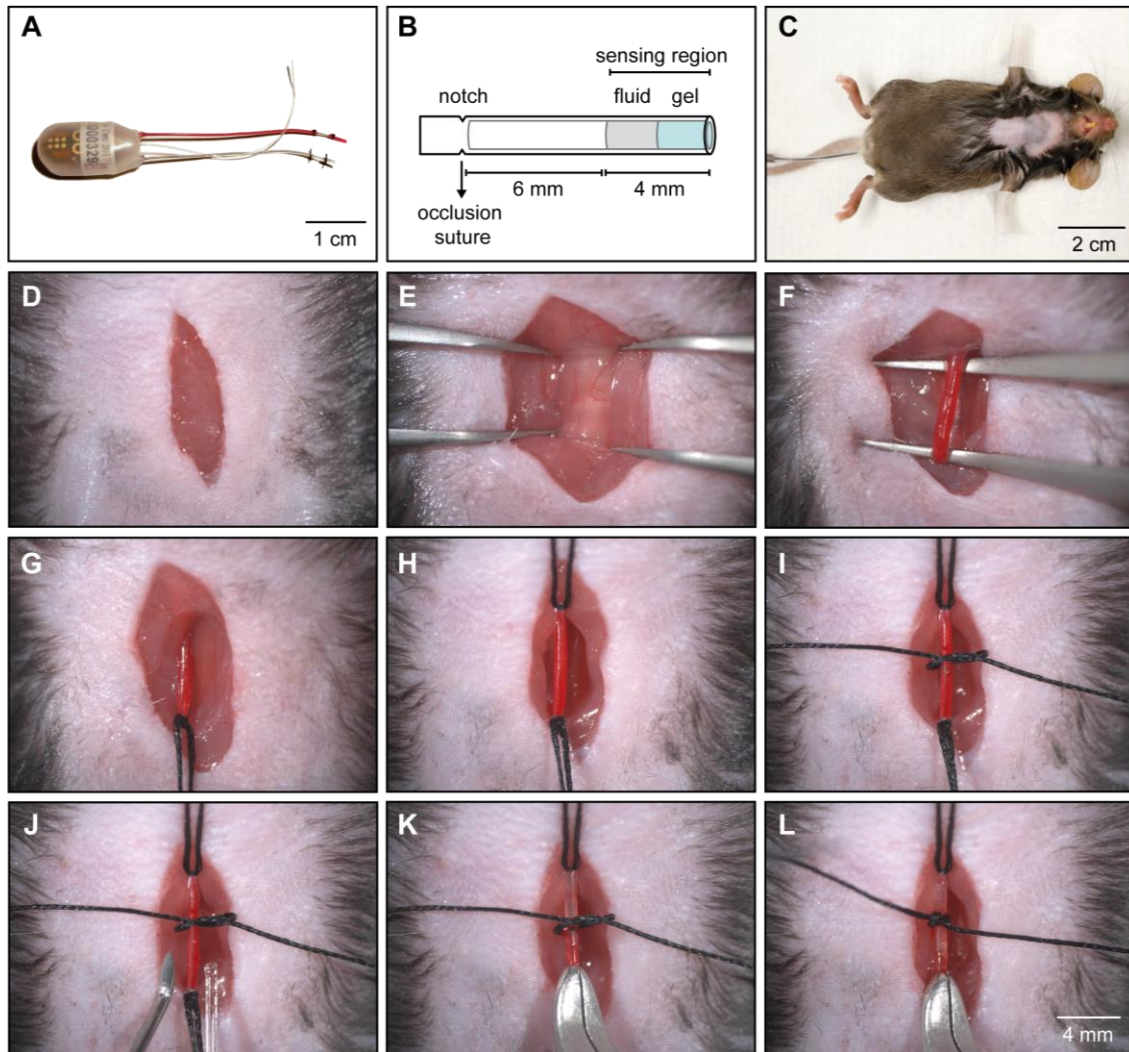

Fig. 17 Implantation of a combined ECG and BP transmitter - left carotid artery cannulation. (A) Device for surgical implantation consists of the device body, two biopotential leads and a pressure catheter. Serial number is labeled on the device body. ECG leads are shortened and tips are insulated. (B) Illustration of the pressure catheter. The sensing region consists of a non-compressible fluid and a biocompatible gel. For a correct position of the catheter, the cranial occlusion suture of the carotid artery has to be secured at the notch of the catheter. (C) Anesthetized mouse prepared for device implantation. (D – L) Step-by step image sequence depicting left carotid artery cannulation. (D) Cervical skin incision. (E) Exposure of the trachea to identify the carotid artery localized sinistral of the trachea. (F) Isolation of the artery from adjacent tissue. (G) Cranial occlusion suture to ligate the vessel. (H) Caudal occlusion suture to temporarily prevent blood flow. (I) Middle occlusion suture to secure the catheter while cannulating. (J) Syringe needle with bended tip to insert the catheter in the artery. (K) Cannulation of the carotid artery (L) The catheter is advanced and positioned in the aortic arch while secured by the middle suture.

Then, three non-absorbable 5-0 sutures were passed underneath the isolated portion of the carotid artery. One was placed cranial, just proximal to the bifurcation of the carotid artery, and was knotted to permanently ligate the vessel (Fig. 17G). The end of the suture was fixed by clamping it in a needle holder. The second suture was placed caudally at a distance of ~5 mm to the ligature suture (Fig. 17H). It is used for temporary occlusion of blood flow during cannulation of the artery. Therefore, a loose knot was made and the end of the suture was tightened and fixed in a second needle holder. The third suture was positioned between suture one and two and a loose knot was made to keep the catheter in place while cannulating the artery (Fig. 17I). Subsequently, one end of the third suture was taped to the surgery table. During the whole procedure the surgical area had to be kept moist using warmed (37°C) 0.9% sterile NaCl solution.

In a next step, the catheter was introduced in the carotid artery. The BP catheter consists of a 5 cm tubing containing a non-compressible fluid and a biocompatible gel at a section of 4 mm from the distal part of the catheter (Fig. 17B). This particular section is the sensing region of the catheter. It should be devoid of air bubbles and should not be touched at any time of the procedure. Before cannulation, the tip of a 25-gauge syringe needle was bent to an angle of ~100° to use it as catheter introducer. Subsequently, the caudally placed occlusion suture was gently pulled using a needle holder to stop blood flow and to slightly lift the artery (Fig. 17J). The artery was then penetrated by the bent needle proximal to the ligation suture and the catheter was inserted at once. For insertion the catheter was gripped by vessel cannulation forceps just before the sensing region (Fig. 17K). When the catheter reached the occlusion suture, the middle suture was tightened to secure the catheter (Fig. 17L). The occlusion suture was then loosened and the catheter was moved forward to position it in the aortic arch. The appropriate length to insert the catheter depends on the size and weight of the mice. For male 12 week-old mice, weighing ~30 g the catheter was inserted until the integrated notch of the catheter reached the ligation suture (Fig. 17B). To secure the catheter in position all three sutures were tied around the artery and the suture ends were cut as short as possible.

Then, the device body was placed in a subcutaneous pocket on the left flank of the mouse. For this purpose, blunt surgical scissors were introduced subcutaneously into the incision and a pocket was formed (Fig. 18B). A 1 ml syringe filled with prewarmed (37°C) 0.9% NaCl was inserted to rinse the pouch followed by insertion of the transmitter core unit (Fig. 18C, D). Subsequently, the ECG leads were arranged subcutaneously in an approximate Einthoven II configuration. For this purpose, the positive lead (red) was tunneled subcutaneously and the terminal end was fixed to the left caudal rib region by absorbable 5-0 sutures (Fig. 18E). The terminal end of the negative lead (colorless) was fixed subcutaneously to the right pectoral muscle (Fig. 18F). To not irritate the tissue, the leads were placed laying flat against the body.

Both leads were tied together and fixed to the left pectoral muscle using absorbable suture (Fig. 18G). The skin was then sutured using non-absorbable 5-0 sutures (Fig. 18H) and the knots were sealed with tissue adhesive (Surgibond®, SMI AG).
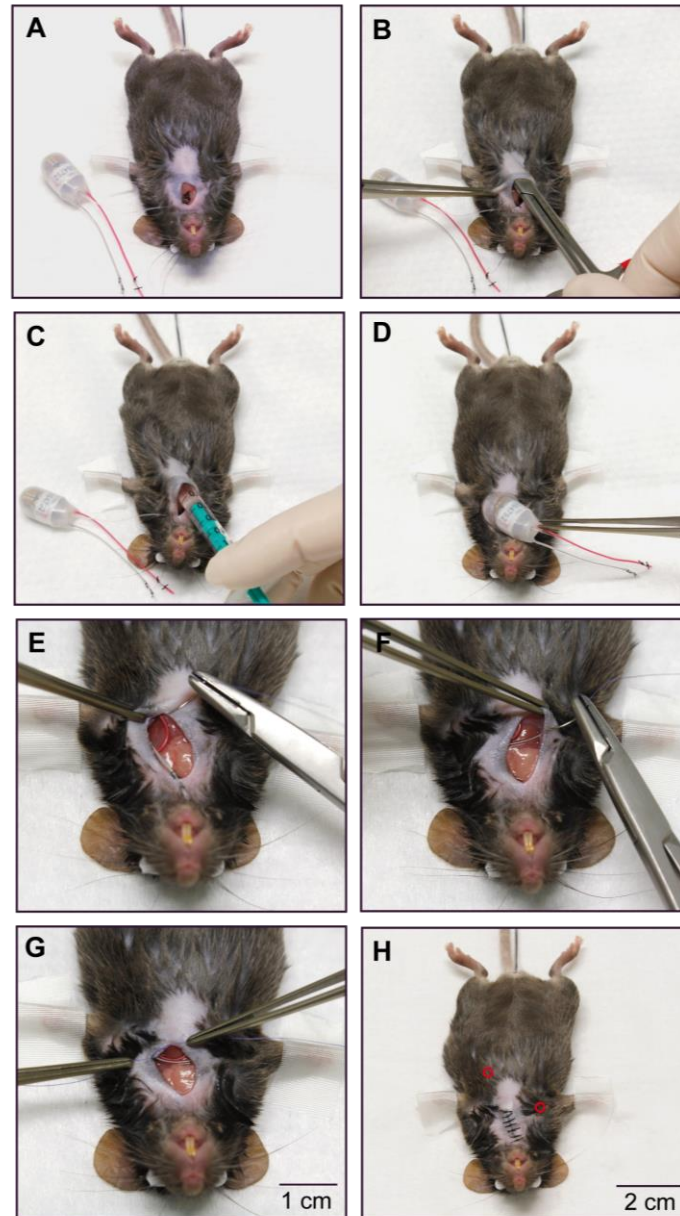

Fig. 18 Implantation of a combined ECG and BP transmitter - subcutaneous placement of the device body and the ECG leads. (A) Mouse after left carotid artery cannulation. The catheter is positioned and secured by the occlusion sutures of the artery (trimmed). (B) Subcutaneous pocket on the left flank of the animal formed by using blunt scissors. (C) Irrigation of the pouch using 1 ml of prewarmed sterile saline. (D) Transmitter placement in the subcutaneous pocket. (E) Placement of the positive lead (red tubing) and fixation of the terminal end to the left intercostal muscles using absorbable suture material. (F) Placement of the negative lead (clear tubing). The tip of the negative lead is fixed to the right pectoral muscle. (G) Placement of a stay suture to secure ECG leads on the chest muscle. (H) Skin closure. Red circles indicate the subcutaneous positions of the lead tips.

Finally, povidone-iodine hydrogel 10% (Ratiopharm GmbH) was applied to the wound for disinfection and 5 mg/kg carprofen (Norbrook) in 0.9% NaCl was injected subcutaneously for postoperative pain relief. In addition, 10 µl/g warmed (37°C) 0.9% NaCl was injected intraperitoneally to protect the mouse against dehydration. The mice were placed in separate housing cages and were allowed to recover for three weeks before basal 72 hours telemetric recordings.

4.2.2 ECG and BP recordings

Implanted transmitters allowed for continuous recordings in freely moving mice. Fig. 19 shows a representative ECG and BP recording. The ECG trace reflects the electrical activity of the heart which is characterized by typical deflections. Depolarization of the atria is represented by the P wave which is followed by depolarization of the ventricles, displayed as the QRS complex. The T wave represents repolarization of the ventricles and appears inverted in murine ECG [87]. The duration of one heartbeat corresponds to the distance of two R - peaks; the RR interval is used to calculate HR in beats per minute (bpm).
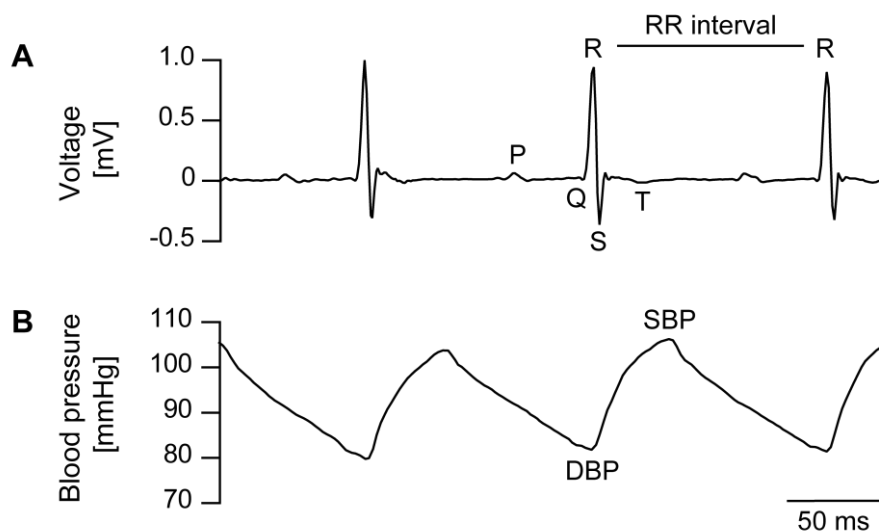

Fig. 19 Telemetric ECG and BP recordings. (A) Representative ECG trace of a WT mouse. Phases of the cardiac cycle are indicated. P wave, QRS complex, T wave and RR interval (B) Corresponding arterial BP data. Systolic (SBP) and diastolic blood pressure (DBP) are highlighted.

The arterial BP rises and falls synchronously with the activity of the heart muscle. Immediately after excitation of the ventricles the heart contracts. As a result, blood of the left ventricle is ejected, which leads to a rise of the aortic BP. The maximum pressure is called systolic blood pressure (SBP). The minimum pressure, before the following cardiac contraction, is called diastolic blood pressure (DBP). The pulse pressure, also called arterial pressure is the difference between SBP and DBP.

4.2.3 Sequence method

For analysis of interactions between vagus nerve activity and HR *in vivo*, a method to estimate baroreflex sensitivity (BRS), was chosen. The applied method provides information about the gain of spontaneous BRS and demonstrates if parasympathetic innervation of the SAN leads to an appropriate HR response.

Since spontaneous BP variability (BPV) leads to an activation of the baroreflex and consequently baroreflex efferents adjust the HR to the given conditions, the translation of BPV into HRV gives an index of BRS [88]. Baroreflex efferents drive HR change by modulation of parasympathetic and sympathetic firing. Changes in sympathetic drive are characterized by very slow fluctuations in a range of 2 to 10 s, whereby changes in vagal drive are in a range of 200 - 650 ms [70]. Therefore, transmission of high-frequency BPV into HRV is related to a change in parasympathetic firing. Hence, when establishing the method, it had to be ensured that only high frequency changes were taken into account.

The applied method is called sequence method, since the beat-to-beat series of SBP and RR intervals were screened for short sequences of 3 beats during spontaneous increase or decrease in SBP. Short sequences were chosen to only capture high frequency changes related to vagus nerve inputs on HR regulation. Increase in SBP over 3 heartbeats leading to a reflectory increase in parasympathetic firing consequently slows down HR. A decrease in HR results in longer RR intervals. This kind of sequence was defined as up sequence (Fig. 20A). In contrast, a down sequence was detected when a decrease in SBP over 3 beats was associated with parallel rise in HR (Fig. 20B). To estimate the relationship between SBP and HR, both parameters were plotted against each other and the slope (ms/mmHg) of the linear regression line was determined per sequence (Fig. 20A, B bottom). The mean slope of all sequences was then calculated and defined as the gain of spontaneous BRS.

For each mouse a 3 hour section of the recording during low activity period was screened for up and down sequences with the following set parameters: only sequences of 3 beats exhibiting a delay between SBP and RR of 1 beat were included in the analysis. The threshold for SBP and RR changes was 0.5 mmHg and 2 ms. The correlation coefficient of the slope of the regression line from RR/SBP plots was set to >0.85 and only sections exhibiting stable SAN rhythm were analyzed.
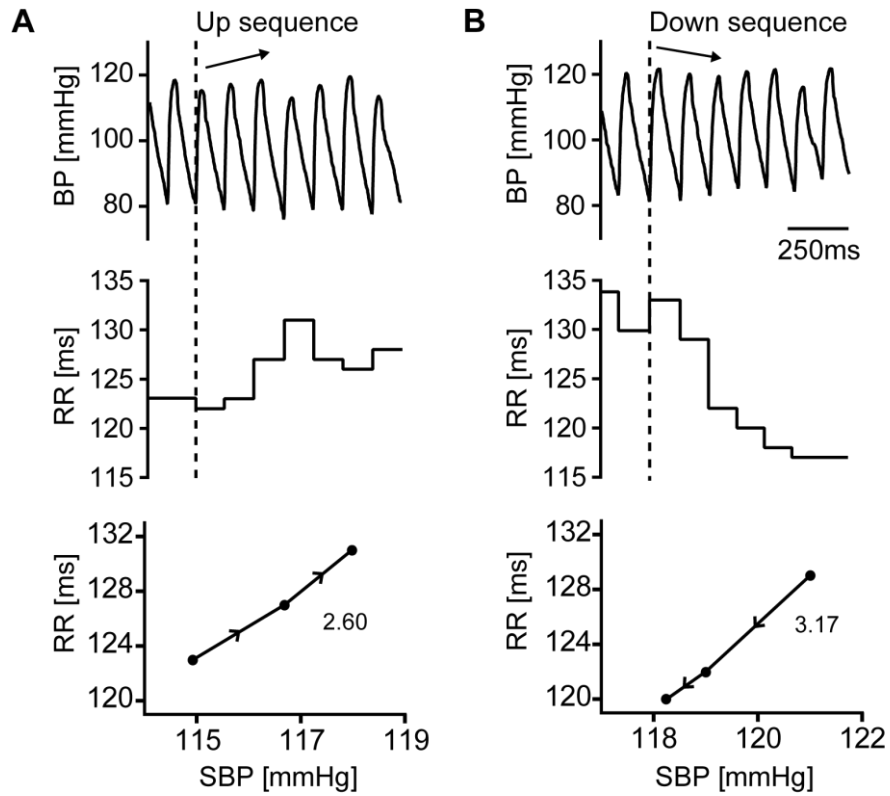
Fig. 20 Estimation of BRS using the sequence method. (A) Representative BP trace of a WT mouse during an up sequence of three consecutive beats (top) associated with parallel increase in RR interval (middle). Representative plot of SBP and corresponding RR intervals (bottom). The slope of the regression line for the outlined exemplary up sequence was 2.60 (in ms/mmHg) as indicated. (B) Representative down sequence with a drop in SBP and a subsequent decrease in RR interval results in a slope of 3.17 ms/mmHg.

4.3 Cardiophysiological analysis of a mouse model with disrupted CDR of HCN4 channels

In the following section the impact of CDR of HCN4 channels on the pacemaker activity was investigated. For this purpose, a multilevel analysis to characterize the cardiac phenotype of HCN4 FEA, a mouse model with disrupted CDR was applied. The study combined *in vivo* investigations by the use of ECG and BP telemetry recordings and *in vitro* studies on different tissue levels. Hence, electrophysiology and optical recordings of whole heart preparations and intact biatrial SAN preparations were performed. In addition, calcium transients of single SAN cells within the intact SAN network were examined.

4.3.1 *In vivo* role of CDR of HCN4 channels

In order to investigate the physiological significance of CDR of HCN4 channel on the cardiac function *in vivo*, analyses of telemetric long-term ECG and BP recordings in freely moving animals were implemented. Therefore, 72 h recordings of continuous measurements during low and high activity phases of WT (n = 9) and HCN4 FEA (n = 11) mice were evaluated for basal HR parameters. The mean HR of HCN4 FEA mice was significantly decreased compared to WT (HR_{Mean}; WT: 522.9 ± 8.3 bpm; HCN4 FEA: 435.9 ± 13.6 bpm; p = 0.00007) (Fig. 21A). This bradycardia was not due to a decreased resting behavior of HCN4 FEA mice as HCN4 FEA and WT mice displayed similar activity data. Fig. 21C depicts circadian rhythm of HR and activity measured in both mouse lines over 72 h during 12 h light/dark cycle. Furthermore, significant bradycardia was observed when average HR in low activity (LA) phases and high activity (HA) phases were analyzed independently. For all three data sets (72h, 12 h LA, and 12 h HA), the absolute value of maximum HR (HR_{max}) and the value of minimum HR (HR_{min}) were compared for HCN4 FEA and WT animals. It revealed, that HR_{max} and HR_{min} were both shifted to lower values in HCN4 FEA mice (Table 1). In contrast, the relative degree of HR regulation dynamics which can be determined by HR_{max}/HR_{min} and the HR range which is defined as $HR_{max} - HR_{min}$ were indistinguishable in WT and HCN4 FEA (Table 1). To further evaluate differences in HR dynamics, mean HR histograms over a period of 72 h were created. WT histograms of HR were symmetrical with a peak in the middle of the histogram whereby HCN4 FEA histograms were shifted to lower values with a left-skewed peak in the low-frequency range (Fig. 21B). In addition, histograms represent that maximum HR values of WT were not reached by HCN4 FEA mice while HR range was similar in both phenotypes. Taken together, HR analysis demonstrated that disrupted CDR of HCN4 channel caused marked bradycardia throughout the entire HR spectrum.
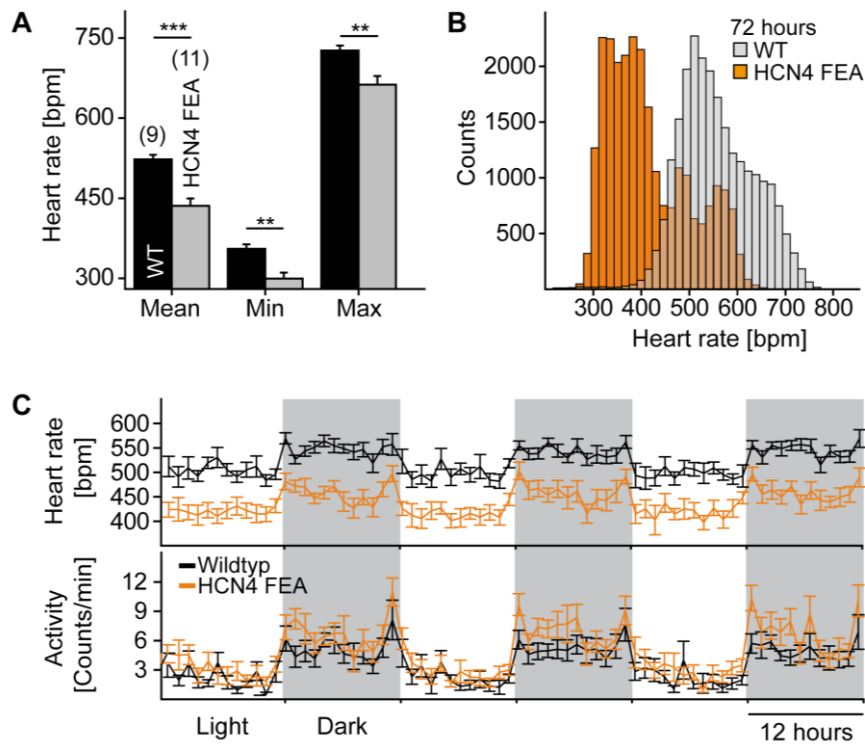
Fig. 21 HR analysis of telemetric ECG recordings. (A) Statistics of HR over a 72 h period. HCN4 FEA mice depict a significantly decreased mean, minimal (min) and maximal (max) HR. All values are given in mean ± SEM; **p<0.01; ***p<0.001; n(WT)=9, n(HCN4 FEA)=11. (B) Representative histograms of a WT (grey) and HCN4 FEA mouse (orange) from 72 h. (C) Regular circadian rhythm of HR (top) and activity (bottom) recorded over a period of 72 h in WT (black) and HCN4 FEA mice (orange). Animals display a lower activity and HR during 12 h light/low activity phase and a higher activity and HR during 12 h dark/high activity phase. A reduction of HR in HCN4 FEA mice was consistently observed during the whole recording period. Graphs are given in mean ± SEM.

In a next step, ECG data was tested for variability of the HR, since the observed bradycardia in HCN4 FEA could be due to a consistent reduction of HR or could be related to HR fluctuations and the incidence of frequent sinus pauses. To obtain a first impression of the data, RR tachograms and poincaré plots were generated of RR interval time series extracted from ECG recordings (Fig. 22). Tachograms of HCN4 FEA mice revealed pronounced HR fluctuations compared to WT. When data was graphically represented by poincaré plots, where each heartbeat is plotted versus its subsequent heartbeat (RR_n on the x-axis versus RR_{n+1} on the y-axis), HCN4 FEA mice demonstrated a high beat-to-beat dispersion and a broad comet-shaped pattern typically observed in SAN dysfunction. By contrast, scatter plots of WT mice displayed less dispersion of the data, located in the high frequency range.
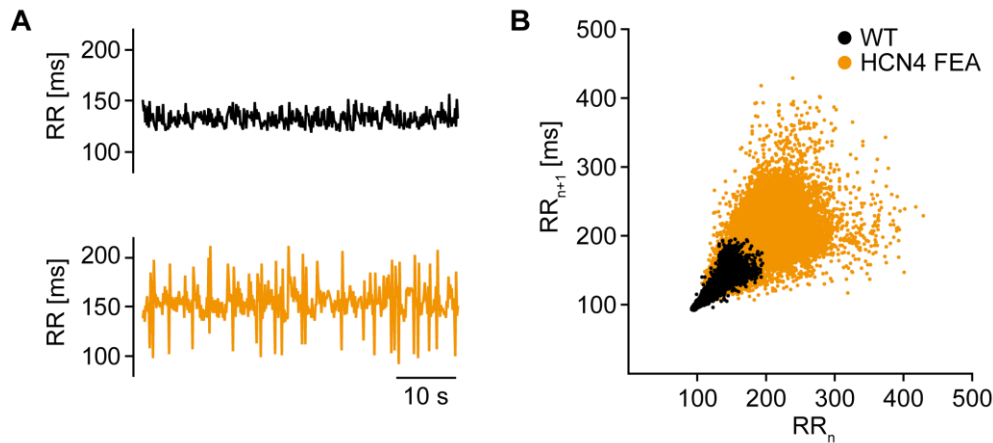
Fig. 22 Analysis of RR interval time series (A) Representative tachograms of the RR interval extracted from ECG recordings of a WT (upper panel, black) and an HCN4 FEA mouse (lower panel, orange) over a period of 30 s during low HR (~400 bpm). (B) Representative poincaré plots of 20000 successive heartbeats for a WT (black) and an HCN4 FEA mouse (orange).

Furthermore, analysis of RR interval time series by statistical descriptors, namely, SDNN and RMSSD revealed markedly increased HRV in HCN4 FEA mice compared to WT. Both time domain parameters were significantly elevated in HCN4 FEA mice, consistent with dramatic fluctuations of the RR interval (Fig. 23A, Table2). RMSSD describes the change in HR from one heartbeat to its successive heartbeat and thereby mainly reflects parasympathetic input. Frequency domain analysis of HRV of HCN4 FEA mice revealed a markedly increased power in all frequency bands (VLF, LF, and HF) compared to WT (Fig. 23B, C, Table 2).
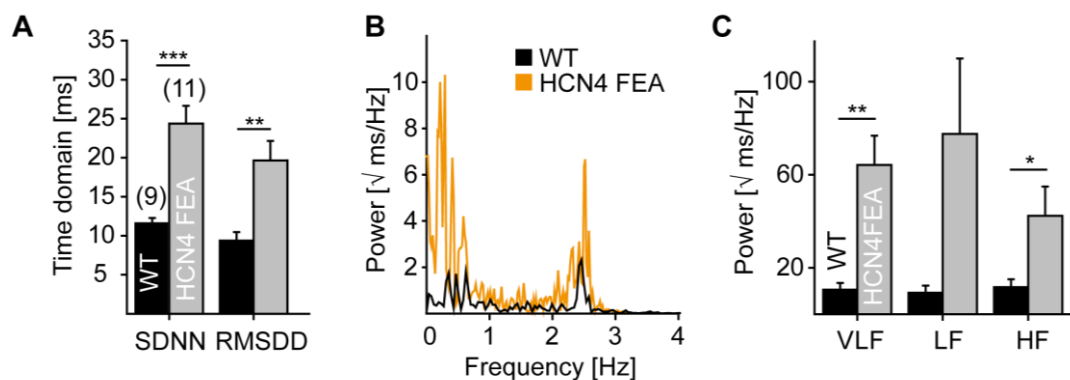

Fig. 23 Time domain and frequency domain analysis. (A) Time domain analysis revealed significantly increased SDNN and RMSSD parameters for HCN4 FEA mice compared to WT. (B) Representative power spectral density plots of a WT (black) and HCN4 FEA mouse (orange), obtained by frequency domain analysis. (C) Statistics of frequency domain analysis. (VLF, very low frequency = 0 – 0.4 Hz; LF, low frequency = 0.4 – 1.5 Hz; HF, high frequency = 1.5 – 4.0 Hz). All values are given in mean ± SEM; *p<0.05; **p<0.01; ***p<0.001; n(WT)=9, n(HCN4 FEA)=11.

Finally, HRV analysis revealed dramatic HR fluctuations in HCN4 FEA mice accompanied by severe bradycardia. Characteristic parameters of ECG data (time of QRS complex, PQ and QT intervals) were similar in WT and HCN4 FEA mice (data not shown). Since it was unclear, if generation of HR fluctuations was attributable to ANS input, sympathetic and parasympathetic regulation were blocked *in vivo* by treatment with propranolol and subsequent injection of atropine. Both reduced HR fluctuations in WT and HCN4 FEA mice (data not shown), which indicated that HRV in HCN4 FEA mice were mainly accountable to intrinsically autonomic regulation.

In the next step, raw ECG and BP traces were further analyzed to evaluate the impact of the previously determined bradycardia and sinus dysrhythmia on the hemodynamics of HCN4 FEA mice. Analysis of 3 h recordings during low activity phase of the mice revealed a significantly reduced DBP in HCN4 FEA mice compared to WT (Fig. 24A, Table 3) (DBP; WT: 86.3 ± 2.0 mmHg; HCN4 FEA: 79.2 ± 1.9 mmHg; p = 0.0196). In contrast, SBP was relatively constant and at similar levels in both phenotypes (SBP; WT: 112.6 ± 1.6 mmHg; HCN4 FEA: 111.1 ± 2.6 mmHg; p = 0.6241). Data inspection revealed that long sinus pauses in HCN4 FEA mice led to extended periods of diastole, the ventricular refilling phases of the heart cycle (Fig. 24B). During diastole, arterial pressure dramatically dropped until the following contraction of the ventricles led to an ejection of blood into the arterial blood system which led to an eventual rise of BP. When SBP and DBP were plotted against their corresponding RR interval it became apparent that long RR intervals and in particular sinus pauses correlate with low DBP whereby SBP was not affected (Fig. 24C).
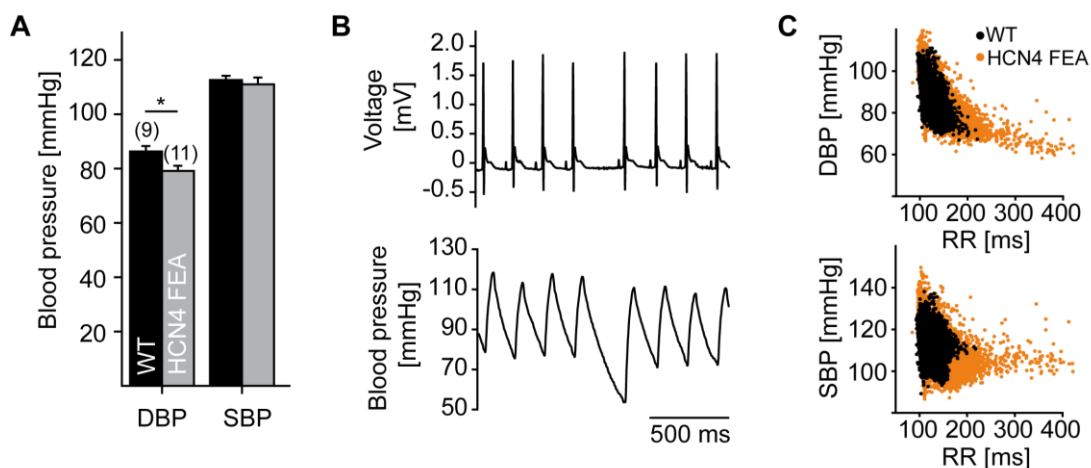

Fig. 24 Correlation of HR and BP in HCN4 FEA mice (A) Statistical analysis of DBP and SBP of a 3 h recording during low activity phase of the mice revealed significantly lower DBP values of HCN4 FEA mice compared to WT but similar SBP data. (B) Representative ECG and BP trace of an HCN4 FEA mouse during a sinus pause which is accompanied with a dramatic drop in DBP. (C) Representative plots of 20000 consecutive RR intervals against their corresponding DBP (top) and SBP (bottom) values for WT (black) and HCN4 FEA (orange). All values are given in mean ± SEM; *p<0.05; n (WT)=9, n(HCN4 FEA)=11.

On closer inspection of telemetric recordings of HCN4 FEA mice, further anomalies of ECG and BP were identified. Data traces were composed of alternating episodes of low and high HR. Sections of bradycardia characterized by long sinus pauses and dramatic decrease in DBP were followed by periods of increased HR and BP fluctuations. Fig. 25 represents typical ECG and BP traces of a WT and HCN4 FEA mouse. WT ECG recordings showed stable sinus rhythm with steady BP rise (SBP) and fall (DBP). By contrast, ECG recordings of HCN4 FEA mice displayed distinct arrhythmias.
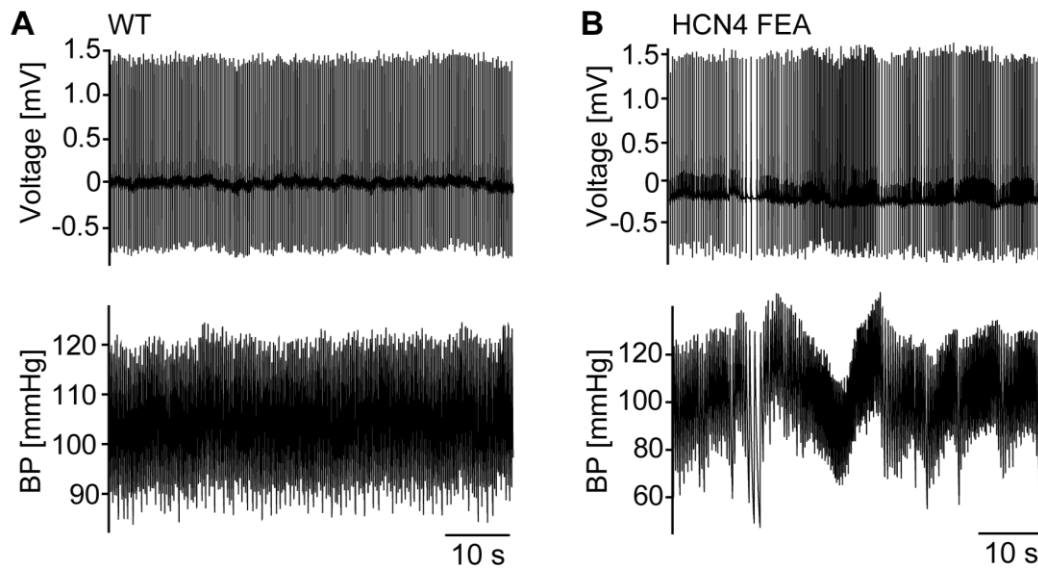

Fig. 25 Telemetric ECG and BP traces of WT and HCN4 FEA mice. (A) Representative raw ECG (upper panel) and BP (lower panel) traces of a WT mouse show a stable rhythmicity. (B) Representative traces of an HCN4 FEA mouse revealed periods of slow and fast HR accompanied with BP fluctuations.

Closer examination of a section during spontaneous accelerated HR revealed two specific forms of arrhythmia in HCN4 FEA mice: isorhythmic AV dissociation (IAVD) and junctional escape rhythm (JER) (Fig. 26). Both types of dysrhythmia are characterized by the presence of a subsidiary pacemaker which compensates slow SAN rhythm and takes over the activation of the heart. Therefore, it can be described as a kind of escape mechanisms. During JER, an ectopic focus activates the ventricles as well as retrogradely activates the atria which lead to short-term episodes of junctional tachycardia. IAVD sustains over longer periods and two independent foci exist in parallel: the SAN drives the activation of the atria whereby an ectopic focus drives the activation of the ventricles [89]. Consequently, P wave and QRS complexes are dissociated which lead to fluctuations of the PR interval. Notably, QRS complex morphology during escape rhythm is undistinguishable to that during sinus rhythm. Over the course of escape phenomena, atrial and ventricular contraction are not properly timed leading to insufficient filling of the ventricles and consequently to a decrease in systemic arterial BP [89].

Combined telemetric ECG and BP recordings of HCN 4 FEA mice revealed that a decrease in PR interval led to a decrease in SBP and DBP (Fig. 26). A return of the rhythm to stable SAN conduction led to normalization of BP. Importantly, HR range in HCN4 FEA mice was still preserved after excluding episodes during JER and IAVD (data not shown).

Both types of escape phenomena where identified in telemetric ECG data of HCN4 FEA mice and were further analyzed by optical mapping of Langendorff hearts.
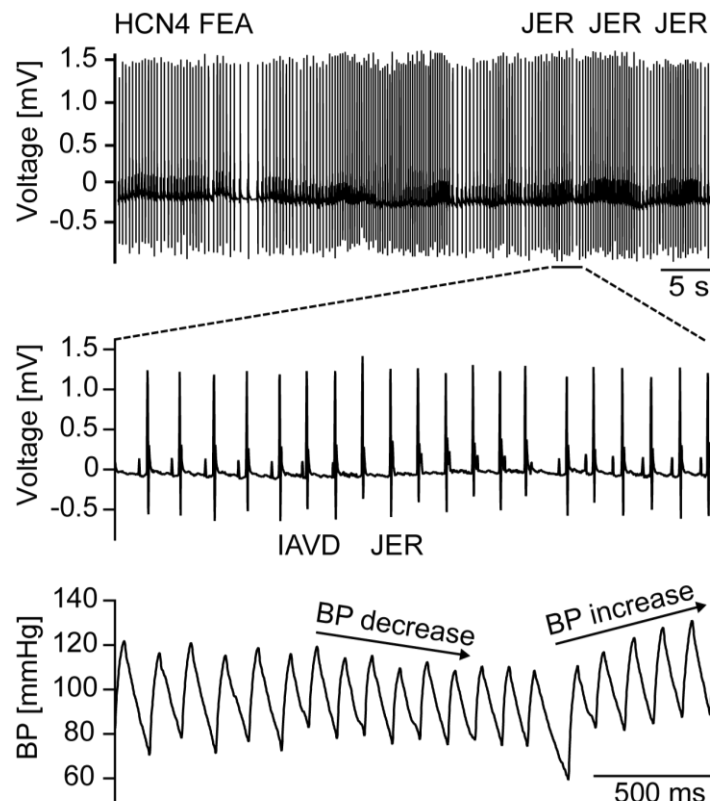

Fig. 26 Escape phenomena in HCN4 FEA mice. Representative telemetric ECG trace of an HCN4 FEA mouse (top) depicts alternating episodes of sinus rhythm during low HR and of an escape rhythm during accelerated HR. Closer inspection (middle) reveals dissociation of the P waves and QRS complexes which indicates the presence of two independent pacemakers. Isoryhthmic AV dissociation (IAVD) and junctional escape rhythm (JER) were observed in HCN4 FEA mice. Corresponding arterial BP recordings showed a decrease in arterial pressure during successive decrease in PR intervals. Return of the rhythm to normal stabilizes BP.

JER was characterized by episodes of HR acceleration that alternate with short episodes of sinus rhythm. Since HR of HCN4 FEA mice were dramatically reduced, heartbeats partially originated from a subsidiary pacemaker that activated both, the atria and the ventricles. The ectopic rhythm of a second independent pacemaker was faster than SAN firing and thereby suppressed SAN rhythm. During JER the P wave lied hidden in the QRS complex or occurred slightly after of before QRS complex. The location of the P wave depends on the location of the subsidiary pacemaker. Optical mapping of an HCN4 FEA Langendorff heart during JER

verified the existence of a second pacemaker located on the endocardial side close to the AV junction and it evidenced its retrograde activation of the atria. Fig. 27 displays optical action potentials and a simultaneously measured ECG trace during JER. Isochronal activation maps of the atria and the ventricles were created. The interval from the time when atrial activation was completed to the time of the first breakthrough of the signal in the ventricles describes the transition time through the AV node, the branches of AV bundle and the HIS bundle. Optical data only derived from superficial layers of tissue, but conclusions about the location of the subsidiary pacemaker within the heart could be drawn from the transition time and the pattern of activation. In beat number 1 of Fig. 27 SAN activated the atria, though the signal was not conducted to the ventricles. It was blocked by refractory tissue due to subsidiary pacemaker activation driving the ventricles. This event led to a shorter PR interval. JER occurred in beat number 2, atria were activated retrogradely and ventricles were activated anterogradely at once which led to the conclusion that the ectopic focus was located somewhere close to the AV junction. In beat number 3 – 5 the ventricular signal preceded the atrial signal and PR interval became negative.
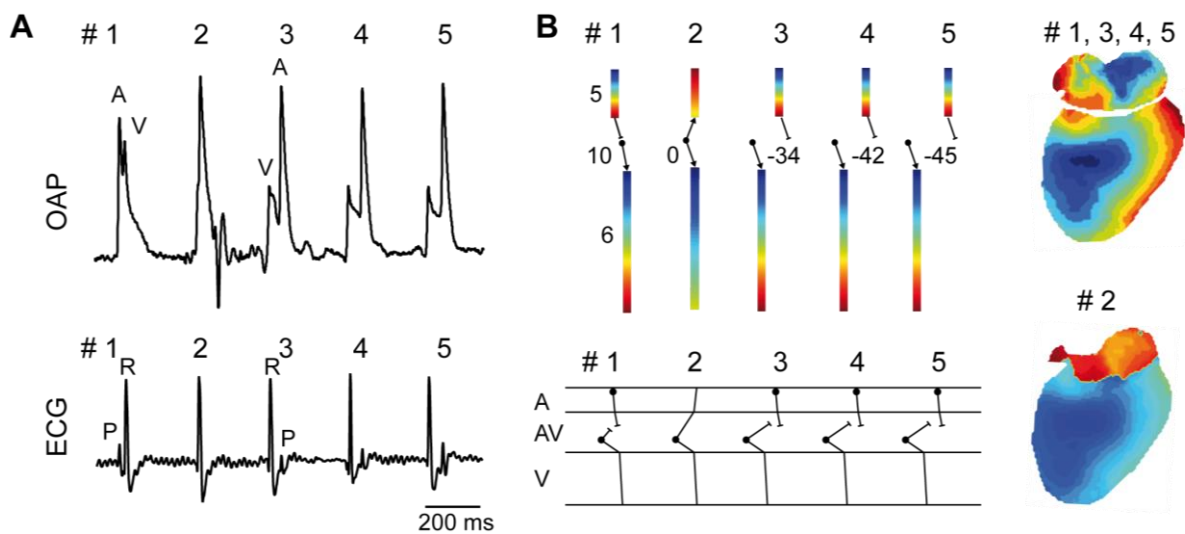

Fig. 27 JER during optical recordings of HCN4 FEA Langendorff hearts. (A) OAPs (upper panel) and surface ECG recordings (lower panel) from an HCN4 FEA Langendorff heart during JER. In beat #1 atrial signal occurred slightly before ventricular signal. In beat #2 the atrial signal is hidden behind the ventricular signal. In beat #3 - 5 the ventricular signal precedes the atrial signal. (B) Ladder diagrams for beat #1 – 5 determined from color time scales of the optical data (B left, top) and its schematic ladder diagrams (B left, bottom) indicate atrial (color time scale, top), AV (middle) and ventricular (bottom) conduction times in ms. For beat #1 ventricles were activated by an ectopic focus 10 ms after atrial activation. In beat #2 ventricles and atria were activated simultaneously. In beats #3 – 5 atria were activated by the SAN after the activation of the ventricles by a subsidiary pacemaker. Representative activation map for beat #1 (right, top) demonstrates normal activation pattern. Activation maps for beat #3 – 5 were similar. Activation map (right, bottom) of beat #2 revealed an anterograde activation of the ventricles and retrograde activation of the atria from the AV junction.

IAVD describes a form of escape rhythm where characteristic flirtatious P waves indicate the presence of two independent pacemakers. During IAVD in HCN4 FEA mice the P wave moved back and forth across the QRS complex. The SAN activated the atria, however, its firing rates oscillated and were reduced. The firing rates of a subsidiary pacemaker remained stable and were fast enough to excite the ventricles. This phenomenon was determined by optical mapping of an HCN4 FEA Langendorff heart during IAVD (Fig. 28). Data were analyzed as described above for JER. Beat number 1 and 3 in Fig. 28 demonstrates regular activation of the heart by the SAN. Conduction time was approximately 27 ms. Since the conduction time in beat number 2 was less than 27 ms, the ventricles were driven by a subsidiary pacemaker whereby the atria were activated by the SAN. In the electrical recordings P wave moved closer to the QRS complex. In beat number 4, P wave was hidden behind the QRS complex but atria were still activated by the SAN as became apparent by the pattern of the activation (Fig. 28, #4). In beat number 5, P wave occurred after the QRS complex. In this case, activation of the ventricles by a subsidiary pacemaker preceded activation of the atria by SAN. For beat number 2 and 5 the activation maps were indistinguishable from that of regular rhythm in beat number 1.
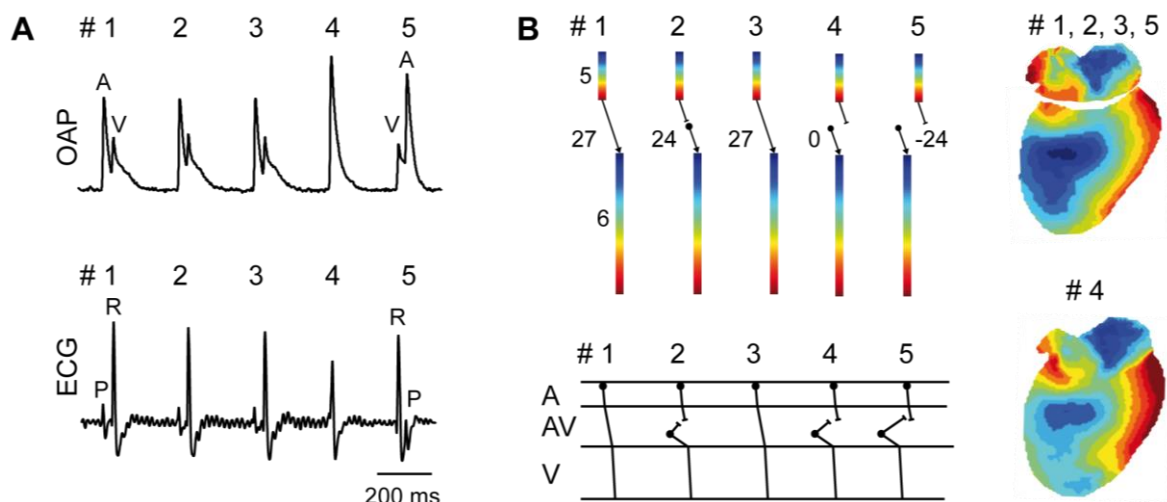

Fig. 28 IAVD during optical recordings of HCN4 FEA Langendorff heart. (A) OAPs (top) and surface ECG (bottom) recorded from an HCN4 FEA Langendorff-perfused heart during IAVD. (B) Ladder diagrams (left) for beat #1 – 5 determined from the recordings presented in (A). Beat #1 and 3 depict regular activation arising from the SAN. Conduction time was 27 ms. Beat #2, 4, and 5 depict a shortened or negative PR during IAVD indicating that the atria were activated by SAN whereby ventricles were activated by a subsidiary pacemaker. The pattern of activation maps for beat #1 – 5 (right) were similar whereby atria and ventricles in beat #4 were activated in parallel and therefore one single activation map for the entire activation of the heart could be drawn.

Taken together, optical mapping of HCN4 FEA Langendorff hearts revealed the presence of two independent pacemaker sites, one in the SAN and one close to the inferior vena cava or

the AV junction. The subsidiary pacemaker takes over ventricular activation or retrogradely activates the atria in circumstances when SAN firing decelerates and therefore acts as escape impulse generator. The occurrence of IAVD and JER in HCN4 FEA mice confirms chronotropic incompetence of the SAN and indicates that the coordinated response of the SAN and the subsidiary pacemaker to HR regulation by the ANS is impaired.

To further analyze the properties of ANS driven HR regulation in HCN4 FEA mice, dynamic interaction between parasympathetic activity and the HR was investigated *in vivo*. Therefore the sequence method, described in chapter 4.2.3 was applied to combined ECG and BP measurements during periods of stable SAN rhythm without IAVD and JER. Briefly, data was screened for short sequences of three beats during rise (up sequence) and fall (down sequence) of SBP that lead to reflectory vagus nerve activation or inactivation which results in a subsequent effect on the HR. Each sequence was analyzed for the graphical relationship of SBP and HR by calculating the slope of the regression line. Interestingly, HCN4 FEA mice showed a higher amplitude and steeper slope for up and down sequences compared to WT (Slope$_{up}$; WT: 4.21 ± 0.25 ms/mmHg; HCN4 FEA: 7.63 ± 1.23 ms/mmHg; p = 0.0238; Slope$_{down}$; WT: 4.09 ± 0.39 ms/mmHg; HCN4 FEA: 8.93 ± 1.49 ms/mmHg; p = 0.0103). For both phenotypes a similar amount of sequences were identified (Fig. 29, Table 3). These results indicated a higher gain of the reflex in HCN4 FEA mice which implies that a loss of HCN4 channel CDR leads to overshooting responses to vagus nerve activity and that SAN firing is more prone to perturbating influences like inputs from the ANS. Therefore, CDR of HCN4 channel appears to be essential to antagonize and dampen parasympathetic effects on the heart and is also required for adequate baroreceptor reflex function.
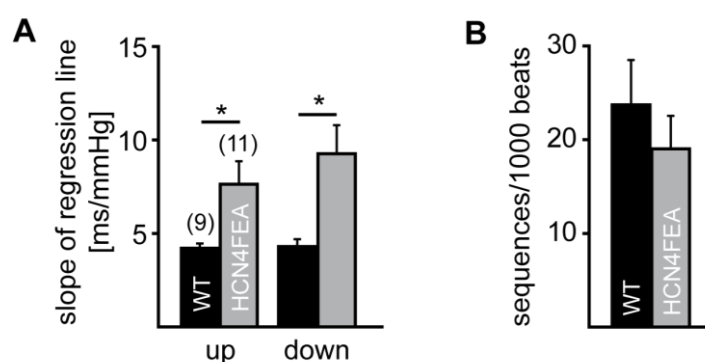

Fig. 29 HR adaptation to dynamic vagal nerve activity *in vivo* determined by the sequence method. (A) Statistics of the mean slope of RR/SBP relationship. HCN4 FEA mice showed a significantly higher mean slope of the regression line in up and down sequences compared to WT. (B) Total amount of up and down sequences in WT and HCN4 FEA mice indicated in sequences/1000 beats. All values are given in mean ± SEM; *p<0.05; n(WT)=9, n(HCN4 FEA)=11.

4.3.2 Role of CDR of HCN4 channels in the SAN network

Evidence of chronotropic incompetence of the SAN in HCN4 FEA mice was provided by *in vivo* ECG and BP data analysis. Intact biatrial SAN preparations of WT (n=26) and HCN4 FEA (n=31) were investigated by electrical recordings and optical measurements to further analyze the impact of disrupted CDR of HCN4 on the SAN network level. Electrical recordings of SAN explants revealed significantly pronounced fluctuations of the beating rate in HCN4 FEA preparations compared to WT determined by tachograms and the calculation of RMSSD and SDNN (Fig. 30, Table 4). In addition, a loss of CDR of HCN4 resulted in a significantly reduced beating rate, depicted as the length of NN intervals (Fig. 30, Table 4). These data are almost consistent with data derived from *in vivo* ECG recordings (chapter 4.3.1) even though intrinsic autonomic regulation is lacking in *in vitro* preparations which indicates that the SAN network of HCN4 FEA mice by itself is unstable and prone to perturbations.
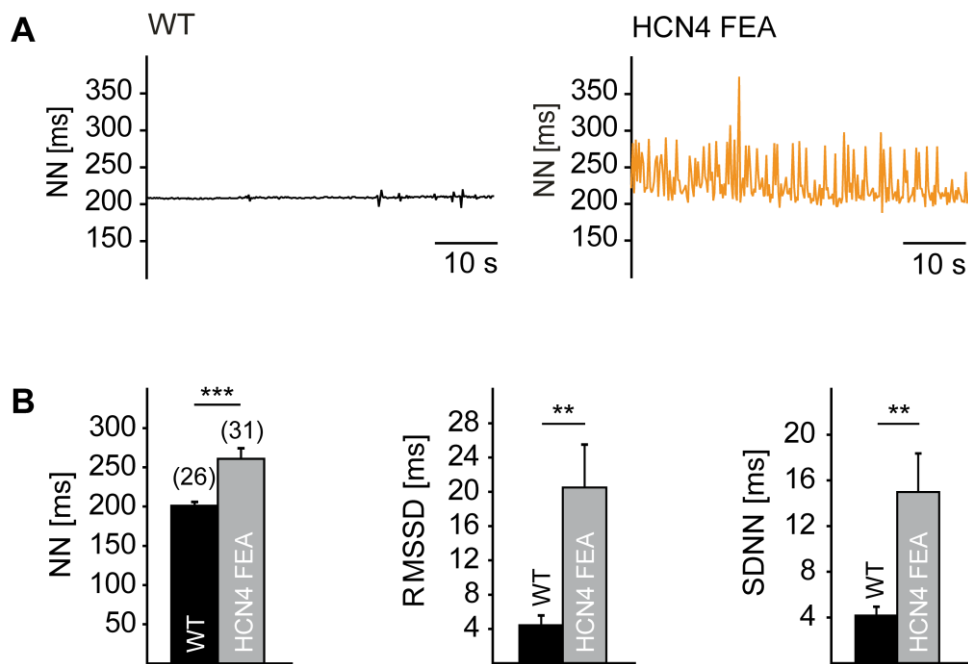

Fig. 30 Analysis of the beating rates and HRV parameters from biatrial SAN preparations. (A) Representative tachograms of biatrial SAN preparations from a WT (left) and HCN4 FEA mouse (right) demonstrate increased fluctuations of the NN intervals in HCN4 FEA. (B) Statistics of the mean beating rate, indicated as NN interval (right), of the mean RMSSD (middle), and mean SDNN (right). Values were obtained from electrical recordings of biatrial SAN preparations over a duration of 1 min. SAN explants of HCN4 FEA mice showed increased values in all three parameters compared to WT. All values are given in mean ± SEM; **p<0.01; ***p<0.001; n(WT)=26, n(HCN4 FEA)=31.

To further evaluate the cause and impact of SAN network instability, optical recordings of intact biatrial SAN preparations were performed to obtain informations about the anatomical structure of impulse formation and propagation within the intact SAN network (Fig. 31). Isochronal

activation maps of WT and HCN4 FEA preparations showed a similar impulse origin and comparable conduction pathways throughout the SAN and atria. In contrast, SACT was significantly prolonged in HCN4 FEA explants (n=8) compared to WT (n=7) (SACT; WT: 4.86 ± 0.37 ms; HCN4 FEA: 7.44 ± 0.57 ms; p = 0.0029) (Fig. 31B, Table5). Activation maps of WT (n=26) and HCN4 FEA (n=31) were further analyzed for the exact position of the leading pacemaker site. This investigation revealed that a loss of CDR of HCN4 channel had no impact on the pacemaker position within the SAN during baseline conditions. For both phenotypes the impulse origin was similar and remained perfectly stable within the territory of the SAN (Fig. 31C, D).
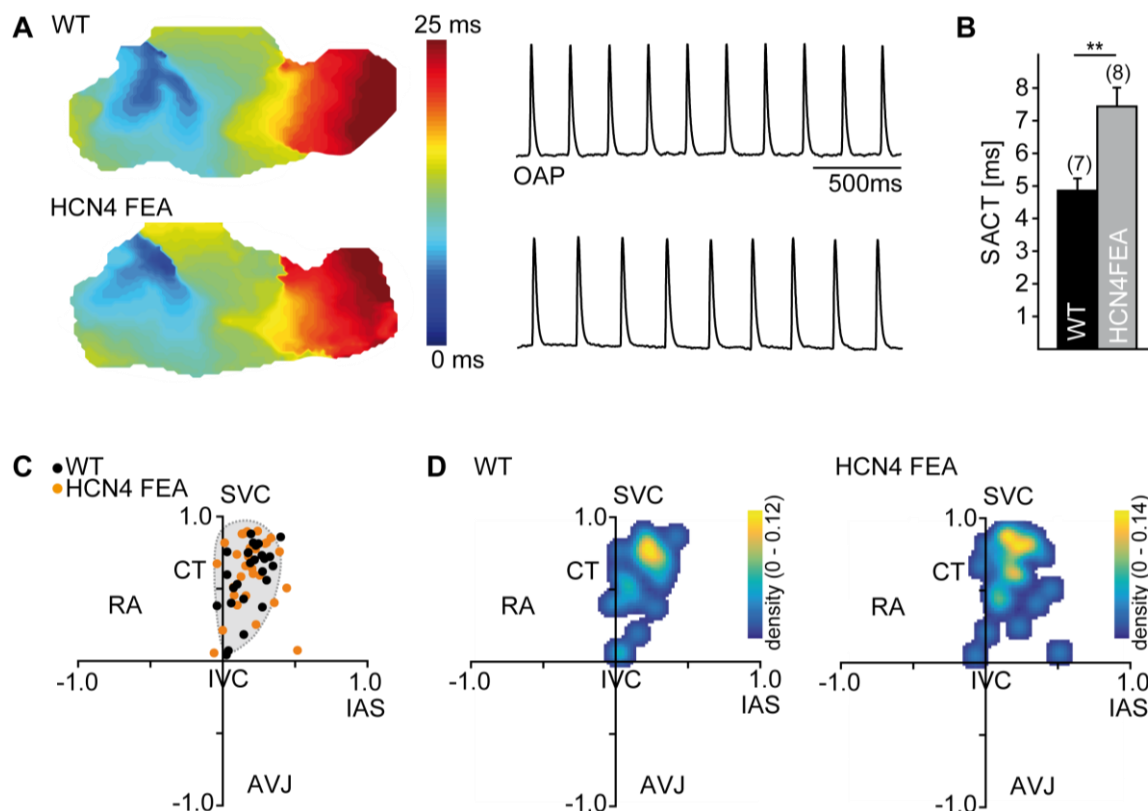

Fig. 31 Optical mapping of biatrial SAN preparations of WT and HCN4 FEA mice. (A) Representative isochronal activation maps of biatrial SAN preparations of WT (upper panel) and HCN4 FEA (lower panel) and their corresponding OAPs derived from SAN region during spontaneous rhythm. (B) Statistics of mean SACT determined by optical mapping of WT (n=7) and HCN4 FEA (n=8). Values are given in mean ± SEM; **p<0.01 (C) Coordinate system with plotted leading pacemaker position for WT (black dots) and HCN4 FEA (orange dots). (D) Density plots demonstrate a similar distribution of the leading pacemaker site within the anatomical borders of the SAN (in grey) for WT (left) and HCN4 FEA (right). RA: right atrium; CT: crista terminalis; IVC: inferior vena cava; SVC: superior vena cava; AVJ: atrioventricular junction; IAS interatrial septum.

The hypothesis that disrupted CDR of HCN4 leads to a markedly increased sensitivity of the SAN to perturbating influences was further tested by application of a parasympathomimetic drug. Treatment of intact biatrial SAN preparations of WT (n=13) and HCN4 FEA (n=16) with

1 µM of the ACh analog carbachol reduced the cAMP level and therefore mimicked vagus nerve activity. Carbachol led to a decrease in beating rate in both genotypes (Table 5). Optical recordings during carbachol application revealed a shift of the leading pacemaker site towards the IVC and IAS. The magnitude of the shift was larger in HCN4 FEA SAN explants compared to WT, but not significantly different (Fig. 32, Table 5).
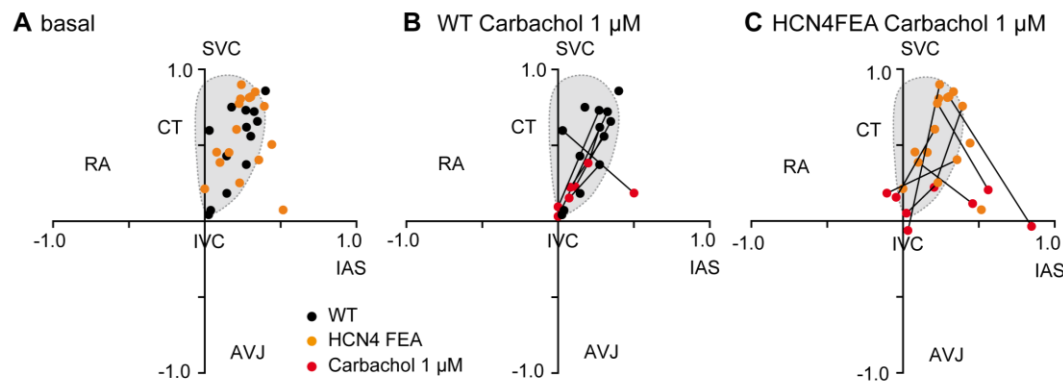

Fig. 32 Leading pacemaker position before and during application of a parasympathomimetic drug. (A) Location of the leading pacemaker site at baseline in biatrial SAN preparations of WT (black dots, n=13) and HCN4 FEA (orange dots, n=16). (B) Leading pacemaker position of WT before (black dots) and during application of 1 µM carbachol (red dots). Pacemaker position shifted in n=7 WT SAN preparations. (C) Leading pacemaker position of HCN4 FEA before (orange dots) and after application of 1 µM carbachol (red dots). Pacemaker position shifted in n=8 HCN4 FEA SAN preparations but to a larger extent compared to WT.

Physiologically, parasympathetic nerve terminals of the right vagus nerve release ACh to the SAN. To investigate the effect of physiological, pulsatile, and transient release of ACh, the right vagus nerve of WT (n=6) and HCN4 FEA (n=7) biatrial SAN preparations was electrically stimulated (VNS, vagus nerve stimulation). VNS at 20 Hz stimulation frequency evoked a marked reduction in firing rates of WT and HCN4 FEA preparations. The magnitude of vagal bradycardia was not significantly different in WT compared to HCN4 FEA (Table 5). However, VNS of HCN4 FEA explants induced overshooting episodes of slow firing rates or even sinus arrest which alternated with short episodes of recovery and faster firing rates. In comparison to HCN4 FEA, VNS of WT preparations caused a very stable and persistent decrease in beating rate (Fig. 33A).

To adress this effect to the anatomical location of the leading pacemaker position, optical recordings during VNS were performed. Electrical stimulation of the vagus nerve caused a shift of the leading pacemaker towards an inferior position. The leading pacemaker site shifted approximately within the anatomical borders of the SAN in WT. In contrast, VNS of HCN4 FEA explants caused an extreme shift of the impulse origin towards the IVC and IAS or even in direction of the AV junction (Fig. 33B, D). However, these changed positions of the leading

pacemaker were not persistent thoughout VNS but temporarily returned back to their previous position (Fig. 33C). Furthermore, the magnitude of the shift was significantly larger in HCN4 FEA compared to WT (Table 5).
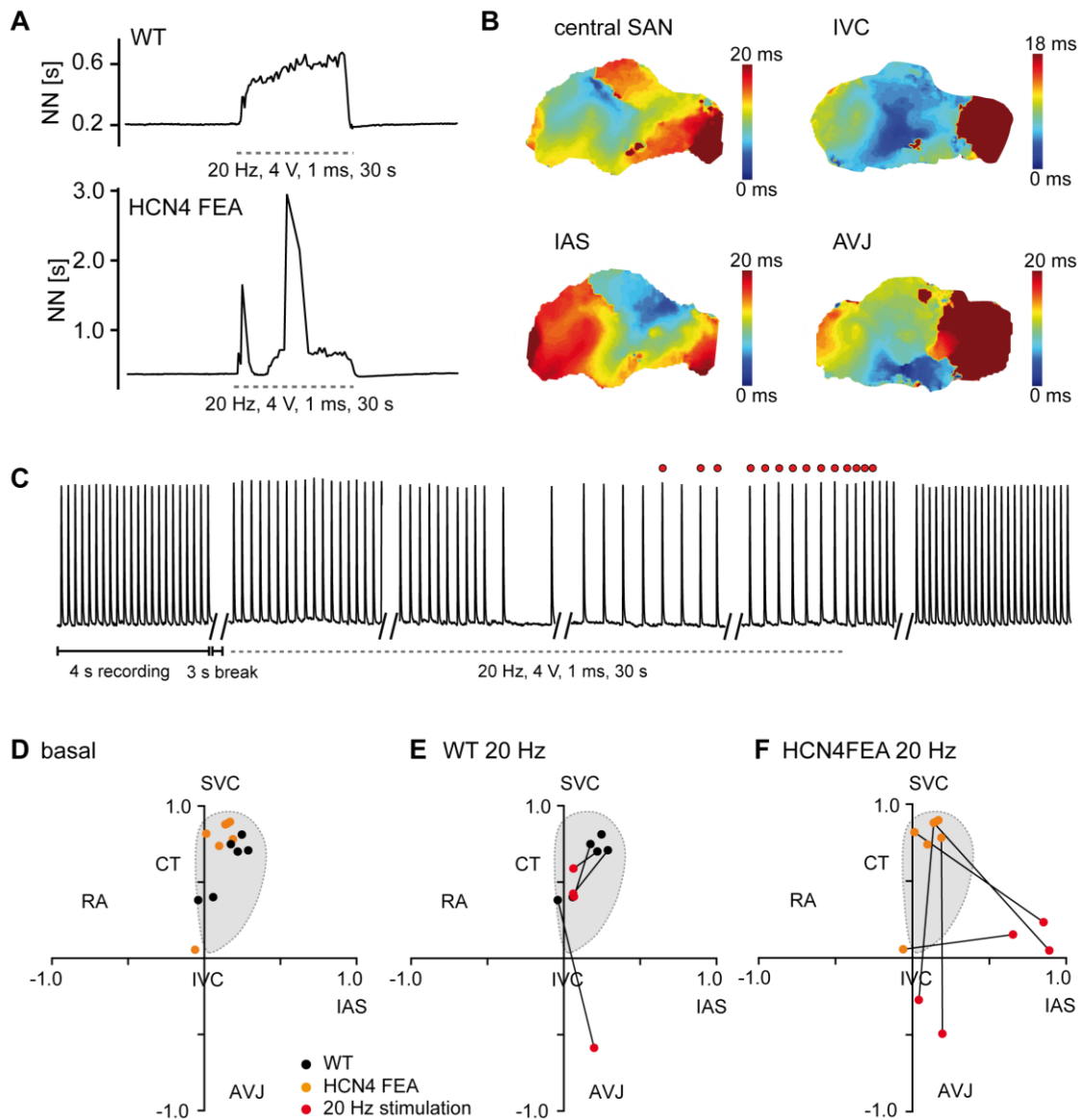

Fig. 33 Leading pacemaker position during vagus nerve stimulation. (A) Representative NN tachograms of biatrial SAN preparations of WT (upper panel) and HCN4 FEA (lower panel) before, during, and after VNS. Time interval of VNS is marked by a dotted line. (B) Isochronal activation maps of HCN4 FEA preparations represent potential positions of the leading pacemaker site (dark blue) during VNS. (C) Representative OAP trace before, during (dotted line) and after VNS obtained by optical recordings of 4 s interrupted by 3 s break. Red dots are highlighting signals that originate from a different leading pacemaker position compared to baseline position. (D) Location of the leading pacemaker site at baseline in biatrial SAN preparations of WT (black dots, n=6) and HCN4 FEA (orange dots, n=7). (E) Leading pacemaker position of WT before (black dots) and during VNS (red dots). Pacemaker position shifted in n=4 WT SAN preparations. (F) Leading pacemaker position of HCN4 FEA before (orange dots) and after VNS (red dots). Pacemaker position shifted in n=4 HCN4 FEA SAN preparations towards the IVC, IAS, and the AVJ.

In conclusion, analysis of mice lacking CDR of HCN4 channel on the network level of the SAN revealed higher beating rate variability, reduced firing rates of the SAN and prolonged SACT. However, the origin of impulse formation and the conduction pathways towards the atria were not impaired in HCN4 FEA mice. VNS of HCN4 FEA preparations caused an overshooting, inappropriate HR response. All these findings are comparable with the discoveries *in vivo* of the present thesis where intrinsic vagus nerve activity led to an overshooting HR reaction. Overall, these findings indicate that CDR of HCN4 channels holds a function as a dampener and antagonist of parasympathetic inputs to the HR.

4.3.3 Role of CDR of HCN4 channels in single cells within the intact SAN network

In a separate experiment, performed by Konstantin Hennis, long-term patch clamp recordings of isolated pacemaker cells derived from HCN4 FEA mice revealed that regular firing of the cells was temporarily interrupted by periods of electrical silence. This mode of intermittent firing was characterized by slow and progressive hyperpolarization of the membrane potential until firing was completely suppressed. These findings implied the existence of an additional activity mode for pacemaker cells during which the cells are electrically silent. This phenomenon was also observed in WT SAN cells but with a lower incidence. For the present thesis, the question was raised, whether cells during non-firing mode are apparent in the SAN cellular network where cells are connected via gap junctions. Therefore confocal calcium imaging of intact whole mount SAN preparations was performed. A preliminary experiment performed by René Rötzer confirmed, that measurements of calcium transients can be used as reliable readout for activity mode of SAN cells.

Calcium imaging of WT preparations using Fluo-4 AM demonstrated rhythmic and global calcium transients in pacemaker cells embedded in the SAN network. By contrast, scanning of HCN4 FEA SAN explants uncovered small subsets of SAN cells exhibiting localized and spontaneous calcium transients during diastole (Fig. 34). In general, these local calcium releases were at a subthreshold level and therefore did not result in global calcium transients. Moreover, these calcium signals were self-limiting and in some cases triggered calcium signal propagation towards neighboring cells which indicates an interaction between adjacent cells. The entire SAN of WT (n=8) and HCN4 FEA (n=8) was scanned for cells exhibiting spontaneous calcium releases and number of cells observed was determined (Fig. 34C). HCN4 FEA SAN showed a significantly higher amount of cells in the non-firing state within the SAN network compared to WT (N cells/μm^2[$*10^{-3}$]$_{basal}$; WT: 0.60 ± 0.16; HCN4 FEA: 1.51 ± 0.35; p = 0.0330) (Table 6). In a next step it was tested if disruption of HCN4 CDR was in fact the cause for spontaneous calcium waves in HCN4 FEA SAN. Therefore, TAT-TRIP8b$_{nano}$ [81] a small peptide that blocks CDR of HCN4 was applied to WT SAN

preparations (n=4). Interestingly, WT SAN thereupon showed a significant increase of the fraction of cells exhibiting localized calcium release (N cells/μm^2[*10^{-3}]$_{Trip8bnano}$; WT: 4.24 ± 1.41; p= 0.0039, compared to WT basal), thus confirming the assumption that HCN4 CDR is mandatory to maintain a stable SAN cellular network activity and prevents switching of pacemaker cells to the non-firing mode.
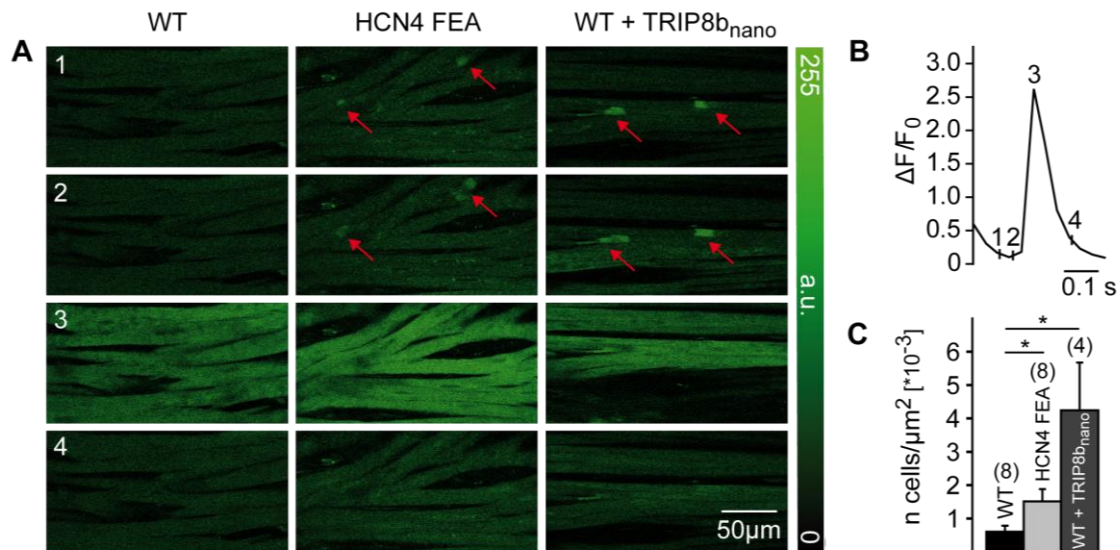

Fig. 34 Confocal calcium recordings to identify non-firing pacemaker cells within the SAN network. (A) Representative sequential series images of confocal calcium recordings using the calcium indicator Fluo-4-AM (fluorescence in arbitrary units [a.u.]) in intact SAN preparations of WT, HCN4 FEA and WT treated with TAT-TRIP8b$_{nano}$. Localized calcium signals are marked by red arrows. (B) Time course of the calcium transient of WT SAN. Numbers 1 – 4 mark the time of the images shown in (A). Spontaneous calcium transients occur during diastole (number 1 and 2). (C) Mean number of cells per μm^2 of the entire SAN displaying subthreshold calcium transient. All values are given in mean ± SEM; *p<0.05; n(WT)=8, n(HCN4 FEA)=8; n(WT+TRIP8b$_{nano}$)=4.

5   Discussion

The present work focuses on the establishment of two methods to perform a cardiophysiological analysis of the genetic modified mouse model HCN4 FEA. It was aimed at specifically determining the role of cAMP-dependent regulation (CDR) of HCN4 channels within the sinoatrial node (SAN).

5.1   Optical mapping to study cardiac electrophysiology

In the present thesis the method of optical mapping was applied to murine whole hearts and biatrial SAN preparations with and without preserved vagus nerve. The method was established to identify the pathology of disrupted CDR of HCN4 channels specifically on the SAN network level. Optical mapping is a method to precisely visualize electrical processes within the intact cardiac tissue. Therefore, it provides a useful tool to investigate the cardiac phenotype of genetically modified mouse models. It is particularly useful to examine cardiac pacemaker function. A wide range of cardiac studies on animal models are limited to investigations on the *in vivo* or whole heart level by using ECG, echocardiography or electrophysiological studies. These investigations focus mainly on the whole heart automaticity and not primarily on the SAN. Further data of SAN function are usually given by isolated single cell electrophysiological investigations. However, to understand pacemaker function in its entirety, SAN cell-to-cell coupling and the functional anatomy of the pacemaker complex should not be overlooked when interpreting results. For the development of novel treatments for SAN dysfunction in human it is necessary to understand the SAN physiology on the network level.

Optical mapping uses fast-voltage-sensitive dyes to map electrical signals in the intact heart. Dyes are embedded in the plasma membrane of the cells and linearly follow transmembrane voltage changes by a change in the emission spectrum. High-spatiotemporal resolution of the applied optical method allowed for exact representation of electrical processes in the heart and provided closer insights in the structure of the SAN region. Isochronal activation maps obtained by optical recordings revealed the exact pattern of activation and the location of the leading pacemaker site within the SAN. It led to an understanding of the hierarchic structure within the SAN built by the leading pacemaker region and by multiple subsidiary pacemakers as published by Glukhov et al [13]. In addition, a block zone in direction to the IAS and LA as well as particular SACPs that conduct the signal towards the RA have been made visible by optical mapping of biatrial SAN preparations. A related method is the usage of microelectrode arrays, which are mounted on the cardiac surface. The signals obtained are not affected by contraction

artifacts or by scattering due to epicardial fat tissue. However, surface microelectrode arrays exhibit a lower spatial resolution and are not strong enough to detect the precise origin of excitation within the SAN [90]. Furthermore, it does not provide the exact SAN structure including conduction pathways from the SAN towards the RA [91,92].

Optical mapping provided a large field of view and offered the advantage to investigate the entire spectrum of heart excitation on the epicardial or endocardial side of the heart. Electrical stimulation of the SAN preparations did not interfere with the optical signals. ECG data of HCN4 FEA mice provided an idea of the cardiac phenotype but optical mapping elucidated the exact origin of arrhythmias (IAVD and JER) and the SAN network function.

5.2   Combined telemetric ECG and BP recordings to estimate BRS

In the present work BRS was estimated by the sequence method that analyses spontaneous BP and HR fluctuations. The method was customized to only detect reflectory HR changes driven by vagus nerve activities. Traditional techniques to estimate BRS are the bolus injections of vasoconstrictors (e.g. phenylephrine) or vasodilators (e.g. sodium nitroprusside). However, due to the immediate effect of these drugs on hemodynamics, BRS can only be measured in anesthetized mice or after a complex implantation of an infusion catheter [71]. In addition, the bolus injection of vasoactive drugs has been considered to be an excessive and less physiological stimulus for reflex changes in HR to BP alterations [93]. A considerable advantage of the sequence method is the fact that it is a noninvasive technique that provides data on spontaneous BRS in real life conditions [94]. Another equally appropriate method to estimate BRS and the effect of dynamic vagus nerve activity on HR is assumed to be the spectral method. It assesses BRS in the frequency domain by calculation of the ratio between changes in HR and changes in blood pressure in a specific frequency band [93,95].

5.3   Cardiophysiological analysis of a mouse model with disrupted CDR of HCN4 channels

The heart function of HCN4 FEA mice was investigated on the whole-animal level, the isolated organ level and on the cellular level:

(1) Studies on the *in vivo* level by ECG and BP measurements were implemented.

(2) The pacemaker function was investigated *in vitro* on the SAN network level by optical experiments and electrical recordings of explanted heart preparations.

(3) The single pacemaker cell function within the intact SAN network was tested *in vitro* by confocal calcium imaging and correlated with data obtained by single cell patch-clamp recordings.

5.3.1   Chronotropic incompetence *in vivo* due to loss of CDR of HCN4 channels

Long-term telemetric ECG recordings of HCN4 FEA mice revealed severe bradycardia, frequent sinus pauses, and SAN dysrhythmia as well as two specific forms of arrhythmias, JER and IAVD.

A severe sinus bradycardia of HCN4 FEA mice became evident by long-term HR analysis and by study of HR histograms. Importantly, observed bradycardia was not due to a reduced activity behavior of HCN4 FEA mice. While maximum, minimum and average HR values were reduced in HCN4 FEA, dynamic range and degree of HR regulation were both similar to WT mice. This indicated that the principle HR regulation by the ANS was not affected in case of disrupted CDR of HCN4 but the whole range of HR regulation was shifted to lower HR values.

In line with the observed chronotropic incompetence marked by bradycardia, escape phenomena arose in heart rhythm of HCN4 FEA mice. ECG data of HCN4 FEA mice revealed frequent phases of accelerated HR accompanied with JER and IAVD. Optical mapping of explanted and perfused whole hearts demonstrated that these forms of arrhythmia were characterized by the activity of two independent pacemaker sites. The leading pacemaker within the SAN drove the atria while a subsidiary pacemaker close to the AVN drove the ventricles or even retrogradely activated the atria. Under physiological conditions the SAN firing rates exceed the firing rates of the AVN by what the AVN activity is suppressed. AVN acts as secondary pacemaker in case of SAN failure. In the absence of CDR of HCN4 channels the intrinsic firing rates of the SAN were reduced and close to the intrinsic firing rates of the AVN whereby it took over heartbeat generation at times. During IAVD the AVN firing rates came near to that of the SAN and overtook ventricular activation. During JER the AVN firing

rates exceeded and outpaced the SAN firing rates to retrogradely activate the atria.

These observations demonstrated that the SAN of HCN4 FEA mice was chronotropically incompetent whereas the subsidiary pacemaker showed unimpaired chronotropic competence. This is suggested to be due to reduced HCN4 expression levels in AVN compared to the SAN region [27,96]. Accordingly, it explains a lower impact of disrupted CDR of HCN4 channels on the AVN. In addition, it is considered that during sympathetic activity AVN firing rates in HCN4 FEA mice accelerated, whereby SAN firing lagged behind AVN rhythm and escape phenomena occurred. Furthermore, high HR values in HR histograms of HCN4 FEA mice displayed by a second peak in the high frequency range were attributable to JER. Notably, after excluding episodes during escape rhythm from HR analysis, the HR range of HCN4 FEA mice was still preserved.

Further analysis of telemetric ECG recordings revealed increased HRV parameters and poincaré plots showing higher beat-to-beat dispersion in HCN4 FEA mice compared to WT, which is considered to be characteristic for SAN dysfunction [97]. Blocking of the ANS by application of propranolol and atropine reduced HRV in HCN4 FEA mice and thus confirmed that increased HRV parameters were mainly attributable to ANS influences. These data indicated that after loss of HCN4 CDR, the SAN was more prone to perturbating influences like parasympathetic or sympathetic inputs. These findings were further confirmed by combined telemetric ECG and BP recordings and determination of BRS. The applied method, the sequence method, to estimate BRS revealed that dynamic increase and decrease in vagus nerve activities led to overshooting and inappropriate HR responses in mice lacking CDR of HCN4 channels.

To conclude, these data demonstrate that the SAN is highly sensitive to ANS inputs in the absence of HCN4 CDR. Furthermore, it indicates that CDR of HCN4 dampens and counteracts parasympathetic effects on the HR. These findings are in line with the work of Fenske and colleagues [3,28] who described that one role of HCN channels is to stabilize and dampen transient changes in membrane potential and fluctuations in firing rates of the SAN.

5.3.2 Instabilities of the SAN network *in vitro* due to loss of CDR of HCN4 channels

In vitro SAN preparations, where the system was dissociated from the ANS displayed a reduced firing rate and increased HR fluctuations. These findings point to the presence of SAN dysfunction and intrinsic instabilities of the SAN network due to disrupted CDR of HCN4 channels. Optical mapping of biatrial SAN preparations revealed a decreased SACT in HCN4 FEA compared to WT. However, this was not due to an altered functional pacemaker anatomy as, during basal conditions, activation maps of WT and HCN4 FEA demonstrated no

differences in the activation pattern or the origin of excitation. The leading pacemaker site in both phenotypes was mainly located in the head of the SAN and all preparations showed two distinct SACPs that conduct pacemaker signals towards the RA. During basal measurements the leading pacemaker site remained stable in its position within the territory of the SAN. Fluctuations in beating rates in HCN4 FEA preparations were not related to a competition of beat-to-beat multiple pacemakers in SAN as shown for example in calsequestrin 2 deficient mice suffering from SAN dysfunction [15].

Telemetric data indicated that after loss of HCN4 CDR, SAN network was more prone to perturbating influences like inputs from the ANS. To further test this hypothesis on the SAN network level, carbachol, an ACh analogon, was applied to biatrial SAN preparations in order to mimic parasympathetic activation by decreasing cAMP levels. This led to a marked decrease in beating rates in WT and HCN4 FEA explants. So far, it has been shown that a change in HR is accompanied with an anatomical shift of the leading pacemaker within the SAN region [13]. This was proven in the present thesis by optical mapping and the identification of the first excitation site: carbachol application led to a shift of the leading pacemaker position in direction of the IVC and AVJ, to a same extent in both phenotypes. To test the system under more physiological conditions a biatrial SAN preparation containing the right vagus nerve was established for the present thesis. It showed that vagus nerve stimulation induced a more physiological, pulsatile, and transient release of ACh that led to a temporary decrease in beating rates and to a pronounced shift of the leading pacemaker. Notably, HCN4 FEA preparations demonstrated an overshooting response with phases of large decrease in firing rate and a disorganized and large shifting of the leading pacemaker to peripheral portions of the SAN preparation. These findings demonstrate that the role of CDR is more pronounced in the head region of the SAN possibly due to a higher HCN4 expression compared to the tail region [69].

This dataset also showed that application of parasympathomimetic drugs and direct vagus nerve stimulation are incomparable. A reason for this might be that stimulation of the vagus nerve leads to a more localized and short-term release of ACh by postganglionic nerve endings supplying the SAN. Thereupon, ACh reacts only with muscarinic receptors located in the synaptic cleft. By contrast, superfusion of the SAN preparation with carbachol provides free access to the entire surface of the SAN to be stimulated. A different set of receptors gets activated which possibly increase the potassium conductance of pacemaker cells. This incomparability of the two methods has been discussed by Campell and colleagues in 1989 [98], however, ACh or carbachol application is often used as a correlate for vagus nerve stimulation [99]. On the other hand, Lang and colleagues [100] used information gathered by ACh-induced shift of the leading pacemaker to elucidate gradient expression of ACh-sensitive

channels within the SAN. Their mathematical model provided instructive insights into the anatomically heterogeneous expression of ACh-sensitive channels within the SAN.

5.3.3 Non-firing activity mode of pacemaker cells within the SAN network regulated by CDR of HCN4 channels

In addition to the experiments presented in the present thesis, in long-term patch clamp studies performed by K. Hennis [4,101] it was discovered that single SAN cells of HCH4 FEA mice fired rhythmically but frequently entered an activity mode characterized by hyperpolarized membrane potentials. During these phases the cells stopped firing and only recovered as soon as membrane potentials slowly shifted to more positive values. Notably, WT cells rarely demonstrated periods of electrical silence but did so when intracellular cAMP levels were lowered by application of carbachol. So, these findings provided evidence for a so far undiscovered activity mode of pacemaker cells regulated by CDR of HCN4 channels.

The finding that single pacemaker cells are able to access a non-firing activity mode, was confirmed in the present thesis by confocal calcium measurements of single cells in the intact SAN network, where cells are electrically connected via gap-junctions. Cells in the non-firing mode were also observed on the SAN network level and more frequently in HCN4 FEA SAN preparations compared to WT SAN. Blocking CDR of HCN4 channels by application of TAT-TRIP8b$_{nano}$ induced non-firing mode in WT SAN cells and thereby mimicked the effect observed in HCN4 FEA. The cell-penetrating peptide TAT-TRIP8b$_{nano}$ compete with cAMP for the same binding site in the C-helix of the CNBD of HCN channels and was able to totally abolish cAMP modulation of WT HCN4 channels [81]. The effect of TAT-TRIP8b$_{nano}$ was even higher compared to the FEA mutation as it resembled a complete knockout of HCN4 CDR and hence shifted the activation threshold to dramatically hyperpolarized values in accordance with the work of Harzheim et al. [48]. In physiological conditions basal cAMP levels in cytoplasm of SAN cells are required to constantly preactivate HCN4 channels [102]. This condition was provided in HCN4 FEA mice by the exchange of Y527 to phenylalanine.

Hyperpolarization-mode in pacemaker cells due to disrupted CDR of HCN4 can be explained as follows. HCN4 channels provide a depolarizing current, I$_h$, that maintains a well-balanced relationship between depolarizing and hyperpolarizing input currents. In WT, both hyperpolarization and cAMP increase HCN4 channel activity and thereby are able to counteract arising hyperpolarizing currents. By contrast, HCN4 FEA channel activity can only be accelerated by hyperpolarization, the channels' fine-tuning by cAMP is lacking. Thus, HCN4 FEA channels are not able to counterbalance hyperpolarizing offset currents as efficiently as WT HCN4 channels do. As a result, membrane potential progressively slides into direction of hyperpolarization until firing is completely suppressed. In summary, CDR of HCN4 channels is

required for maintaining a stable firing activity in pacemaker cells and for its restoration in non-firing mode cells.

The present thesis further elucidated the importance of electrically silent cells for electrical conduction and impulse formation within the intact SAN network. Altered SAN function in HCN4 FEA mice can be explained by the presence of more non-firing cells within the SAN network. More hyperpolarized cells exert a pull on the positive charges of more depolarized, adjacent cells and thereby act as a current sink. A source-sink model of signal transmission describes depolarized cells as source and resting cells as sink, whereby impulse propagation depends on the source-sink relation. During AP propagation positive charges from the source cells flow into sink cells until the activation threshold of the sink cells is reached [22,103]. Cells that are concurrently in the electrical silent mode are supposed to form a functional network that slows down pacemaking of firing cells or rather leads to a slowing down of sinoatrial conduction of APs. This phenomenon explains prolonged SACT in HCN4 FEA SAN preparations.

Confocal calcium recordings of intact SAN preparations performed in the present thesis revealed that cells in the non-firing mode are characterized by localized spontaneous calcium signals during diastole. These signals did not lead to global calcium transients as observed. In the given context, this subthreshold calcium activity can be explained by the cation flow from more depolarized cells to hyperpolarized cells. In addition, localized calcium activity was never observed in single pacemaker cells and only occurred in the SAN network as evidenced by preliminary experiments of R. Rötzer [101]. To conclude, in WT we found a source-sink balance. But in HCN4 FEA disruption of CDR of HCN4 channels led to a source-sink mismatch with more cells in the non-firing mode that inhibited firing cells. The described mechanism explains slowed impulse formation, reduced SACT, and SAN dysfunction observed in HCN4 FEA SAN preparations.

These findings of a so far unknown activity mode of pacemaker cells regulated by CDR of HCN4 channels explain the shift of the leading pacemaker site during vagus nerve stimulation in WT as well as the pronounced shift in HCN4 FEA SAN preparations. In the head region of the SAN HCN4 expression is higher compared to inferior parts of the SAN and parts closer to the AV junction [69]. Therefore, the impact of CDR of HCN4 channels and of inputs from the ANS are more pronounced. During parasympathetic activities pacemaker cells in the superior part of the SAN are more prone to switch to the non-firing mode which leads to a slowing of impulse generation in the SAN head region. At the same time fewer cells in the peripheral region of the SAN are non-firing and therefore the network in this region fires faster than the SAN head region. As a consequence, lower portions of the SAN overtake impulse formation (Fig. 35).
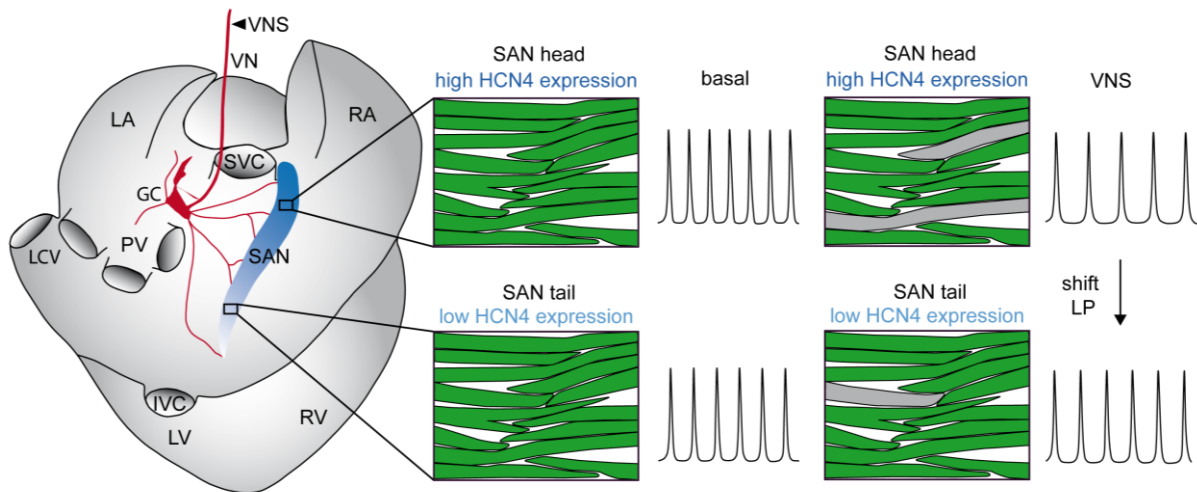
Fig. 35 Schematic overview of the mechanism underlying the leading pacemaker shift during parasympathetic activity. Schematic illustration of the heart, left. Vagus nerve (VN), autonomic ganglia complex (GC) and epicardial nerve fibres that innervate the SAN are plotted in red. Territory of the SAN is depicted in blue. Color gradient represents HCN4 expression levels within the SAN. Cells in the head region of the SAN show a higher HCN4 expression compared to the tail region of the SAN. Right panel shows the SAN network with pacemaker cells in the firing mode in green and cells in the non-firing mode in grey and the corresponding APs of the particular SAN regions. During basal conditions the leading pacemaker is located in the head region of the SAN. Vagus nerve stimulation (VNS) leads to a switch of pacemaker cells to the non-firing mode but to a higher extent in the head region of the SAN. This leads to a more pronounced reduction in pacemaking in the head region compared to the tail region. As a result, the leading pacemaker (LP) shifts in direction of parts located more inferior within the SAN.

In HCN4 FEA hearts this effect is more pronounced compared to WT. An increased number of cells switch to the non-firing mode and constitute an enlarged inhibitory network that slows down pacemaking and facilitates shifting of the leading pacemaker even to portions outside of the territory of the SAN.

In summary, CDR of HCN4 channels is not required for principal HR regulation by the ANS as proposed by Bucchi et al [104] but provides stabilizing and dampening properties on the SAN network function and pacemaker activity. It is suggested that CDR of HCN4 channels plays a key role in regulating a newly identified component of the chronotropic effect which is characterized by the non-firing mode of pacemaker cells.

6   Outlook

The present study demonstrates that dependencies of autonomic regulation, CDR of HCN channels, and SAN network function are obvious and confirms experiments done by DiFrancesco [21,105]. However, the underlying mechanism of autonomic HR regulation through CDR of HCN4 channels is more complex than originally proposed. The role of CDR of HCN4 in regulating the non-firing mode of pacemaker cells is a novel finding and merits further research. This new perspective on pacemaker cell regulation could clarify the role of HCN expression in other organ pacemaker cells like interstitial cells of cajal in the gastrointestinal tract [25] or the urinary bladder [26], where the channels are not required for the generation of pacemaker potentials but are suggested to play a regulatory role for pacemaker activity.

In the context of the present work it would be of further interest to investigate the effect of sympathetic stimulation on the SAN function in HCN4 FEA mice. This question could be experimentally addressed by the application of a sympathomimetic drug like isoproterenol, or through direct stimulation of cardiac sympathetic nerves. Furthermore, extended research on the non-firing mode of pacemaker cells could be introduced by a combination of calcium and voltage confocal imaging of pacemaker cells within the SAN network. Confocal imaging of SAN preparations with preserved vagus nerve might be of great interest to demonstrate pacemaker cells switching into the non-firing mode during vagus nerve stimulation. *In vivo,* a surgical removal of the cardiac parasympathetic nerves, a vagotomy, in HCN4 FEA mice could provide further data to elucidate the impact of parasympathetic activity on SAN dysfunction in mice with disrupted CDR of HCN4 channels.

The cardiac phenotype of HCN4 FEA mice including sinus dysrhythmia, pathological bradycardia and chronotropic incompetence is comparable with symptoms observed in human patients with sick sinus syndrome [106]. The mechanisms discovered are considered to be translatable to human SAN function. Although the absolute HR values differ between the two species, the relative dynamic range of HR regulation is similar. For the development of novel treatments for SAN dysfunction in human disease, it is crucial to understand the underlying physiology of the SAN and its regulation by the ANS. Thus, the findings may have direct impact on future treatment of human arrhythmias.

7 Summary

HCN4 channels within the SAN of the heart play a pivotal role for the pacemaker function of SAN cells. Together with other members of the HCN channel family, the current passing HCN4 channels is considered to be fundamental regarding the automaticity of the SAN by contributing to spontaneous depolarization of the membrane potential initiating an action potential. It is commonly known that HCN4 channels are activated upon hyperpolarization and that the gating of the channel is facilitated by binding of cAMP. However, the specific role of CDR of HCN4 channels had not yet been clarified.

The findings of the present thesis provide evidence that CDR of HCN4 is not required for principal HR regulation through the ANS, but plays an important role in stabilizing HR and the sinoatrial network activity. Loss of CDR of HCN4 leads to chronotropic incompetence and to an overshooting, inappropriate response of the HR to parasympathetic activity. In addition, lack of CDR of HCN4 decelerates HR in general which triggers the occurrence of arrhythmia.

The present study together with preliminary work of lab colleagues (S. Fenske, K. Hennis and R. Rötzer [101]) elucidated a previously undiscovered activity mode of pacemaker cells regulated by CDR of HCN4 channels. It was found that pacemaker cells do not continuously fire, but are able to switch temporarily into a non-firing electrical silent mode. Non-firing cells build an inhibitory network within the SAN that slows down pacemaking of firing cells. During inputs from the vagus nerve, CDR of HCN4 counteracts the increase of the inhibitory network by preventing cells from switching to the non-firing mode. This additional activity mode of pacemaker cells increases the dynamic range of HR regulation and builds a so far unknown component of the chronotropic response. The non-firing mode of pacemaker cells may be important to preserve energy during continuous heartbeat generation, and additionally ensures regular pacemaker activity.

The present work investigates the consequence of disrupted CDR of HCN4 on several cardiac levels: *in vivo*, in isolated whole hearts, in SAN preparations, and in single cells embedded in the SAN network. Therefore, two methods were established beforehand, tailored for the needs of this study, and were applied to a mouse model with disrupted CDR of HCN4 channels.

First, visualization of electrical processes in the heart by optical mapping elucidated the functional anatomy of the SAN. The procedure uncovered the influence of the HCN4 expression gradient within the SAN to the effect of parasympathetic inputs. In addition, optical mapping provided information not given by ECG recordings, like the exact origin of arrhythmias. Second, combined ECG and BP measurements and the implemented sequence

method to obtain the gain of baroreflex led to a better understanding of the role of CDR of HCN4 to the interaction of the brain with the SAN pacemaking.

8 Bibliography

1. Mangoni, M. E. & Nargeot, J. Genesis and Regulation of the Heart Automaticity. *Physiol. Rev.* **88,** 919–982 (2008).

2. Kaese, S. & Verheule, S. Cardiac electrophysiology in mice: A matter of size. *Front. Physiol.* **3,** 1–19 (2012).

3. Fenske, S. *et al.* Comprehensive multilevel in vivo and in vitro analysis of heart rate fluctuations in mice by ECG telemetry and electrophysiology. *Nat. Protoc.* **11,** 61–86 (2015).

4. Fenske, S. *et al.* A previously unknown component of the chronotropic effect is controlled by cAMP-dependent regulation of HCN4. *Submitt. to Circ. Res.* (2019).

5. Keith, A. & Flack, M. The Form and Nature of the Muscular Connections between the Primary Divisions of the Vertebrate Heart. *J. Anat. Physiol.* **41,** 172–89 (1907).

6. Liu, J., Dobrzynski, H., Yanni, J., Boyett, M. R. & Lei, M. Organisation of the mouse sinoatrial node : structure and expression of HCN channels. *Cardiovasc. Res.* **73,** 729–738 (2007).

7. Fedorov, V. V. *et al.* Structural and functional evidence for discrete exit pathways that connect the canine sinoatrial node and atria. *Circ. Res.* **104,** 915–923 (2009).

8. Boyett, M. R., Honjo, H. & Kodama, I. The sinoatrial node, a heterogeneous pacemaker structure. *Cardiovasc. Res.* **47,** 658–687 (2000).

9. Coppen, S. R. *et al.* Connexin45, a major connexin of the rabbit sinoatrial node, is co-expressed with connexin43 in a restricted zone at the nodal-crista terminalis border. *J. Histochem. Cytochem.* **47,** 907–918 (1999).

10. Bartos, D. C., Grandi, E. & Ripplinger, C. M. Ion Channels in the Heart. *Compr. Physiol.* **5,** 1423–1464 (2015).

11. Verheijck, E. E. *et al.* Distribution of Atrial and Nodal Cells Within the Rabbit Sinoatrial Node. *Circulation* **97,** 1623–1631 (2012).

12. Unudurthi, S. D., Wolf, R. M. & Hund, T. J. Role of sinoatrial node architecture in maintaining a balanced source-sink relationship and synchronous cardiac pacemaking. *Front. Physiol.* **5,** 1–7 (2014).

13. Glukhov, A. V., Fedorov, V. V., Anderson, M. E., Mohler, P. J. & Efimov, I. R. Functional anatomy of the murine sinus node: high-resolution optical mapping of ankyrin-B heterozygous mice. *Am J Physiol Hear. Circ Physiol* **299,** H482–H491 (2010).

14. Zhang, H. *et al.* Mathematical models of action potentials in the periphery and center of the rabbit sinoatrial node. *Am. J. Physiol. Heart Circ. Physiol.* **279,** H397-421 (2000).

15. Glukhov, A. V. *et al.* Calsequestrin 2 deletion causes sinoatrial node dysfunction and atrial arrhythmias associated with altered sarcoplasmic reticulum calcium cycling and degenerative fibrosis within the mouse atrial pacemaker complex. *Eur. Heart J.* **36,** 686–697a (2015).

16.   Moorman, A. F. M. & Christoffels, V. M. Cardiac Chamber Formation: Development, Genes, and Evolution. *Physiol. Rev.* **83,** 1223–1267 (2003).

17.   Boyett, M. R. ' And the beat goes on ' The cardiac conduction system : the wiring system of the heart. *Exp. Physiol.* **94,** 1035–1049 (2009).

18.   DiFrancesco, D. The contribution of the 'pacemaker' current (if) to generation of spontaneous activity in rabbit sino- atrial node myocytes. *J. Physiol.* **434,** 23–40 (1991).

19.   DiFrancesco, D. Characterization of single pacemaker channels in cardiac sino-atrial node cells. *Nature* **324,** 470–473 (1986).

20.   Ludwig, A., Zong, X., Jeglitsch, M., Hofmann, F. & Biel, M. A family of hyperpolarization-activated mammalian cation channels. *Nature* **393,** 587–591 (1998).

21.   DiFrancesco, D. & Tortora, P. Direct activation of cardiac pacemaker channels by intracellular cyclic AMP. *Nature* **351,** 145–147 (1991).

22.   Wahl-Schott, C., Fenske, S. & Biel, M. HCN channels: New roles in sinoatrial node function. *Curr. Opin. Pharmacol.* **15,** 83–90 (2014).

23.   Dorrell, C. *et al.* Human islets contain four distinct subtypes of β cells. *Nat. Commun.* **7,** 11756 (2016).

24.   Zhang, Y. *et al.* Functional characterization of hyperpolarization-activated cyclic nucleotide-gated channels in rat pancreatic β cells. *J. Endocrinol.* **203,** 45–53 (2009).

25.   Shahi, P. K. *et al.* The possible roles of hyperpolarization-activated cyclic nucleotide channels in regulating pacemaker activity in colonic interstitial cells of Cajal. *J. Gastroenterol.* **49,** 1001–1010 (2014).

26.   Mader, F. *et al.* Hyperpolarization-activated cyclic nucleotide-gated non-selective (HCN) ion channels regulate human and murine urinary bladder contractility. *Front. Physiol.* **9,** 1–16 (2018).

27.   Herrmann, S., Layh, B. & Ludwig, A. Novel insights into the distribution of cardiac HCN channels: An expression study in the mouse heart. *J. Mol. Cell. Cardiol.* **51,** 997–1006 (2011).

28.   Fenske, S. *et al.* Sick sinus syndrome in HCN1-Deficient mice. *Circulation* **128,** 2585–2594 (2013).

29.   Fenske, S. *et al.* HCN3 contributes to the ventricular action potential waveform in the murine heart. *Circ. Res.* **109,** 1015–1023 (2011).

30.   James, Z. M. & Zagotta, W. N. Structural insights into the mechanisms of CNBD channel function. *J. Gen. Physiol.* **150,** 225–244 (2018).

31.   Much, B. *et al.* Role of Subunit Heteromerization and N -Linked Glycosylation in the Formation of Functional Hyperpolarization-activated Cyclic Nucleotide-gated Channels. *J. Biol. Chem.* **278,** 43781–43786 (2003).

32.   Biel, M., Wahl-schott, C., Michalakis, S. & Zong, X. Hyperpolarization-Activated Cation Channels : From Genes to Function. *Physiol. Rev.* **89,** 847–885 (2009).

33.   Doyle, D. A. The Structure of the Potassium Channel: Molecular Basis of K+ Conduction and Selectivity. *Science.* **280,** 69–77 (1998).

34. Lee, C. & Mackinnon, R. Structures of the human HCN1 hyperpolarization-activated channel. *Cell* **168,** 111–120 (2018).

35. Zhou, Y., Morais-Cabral, J. H., Kaufman, A. & MacKinnon, R. Chemistry of ion coordination and hydration revealed by a K+ channel–Fab complex at 2.0 Å resolution. *Nature* **414,** 43–48 (2001).

36. Aggarwal, S. K. & MacKinnon, R. Contribution of the S4 Segment to Gating Charge in the Shaker K+ Channel. *Neuron* **16,** 1169–1177 (1996).

37. Long, S. B., Tao, X., Campbell, E. B. & MacKinnon, R. Atomic structure of a voltage-dependent K+ channel in a lipid membrane-like environment. *Nature* **450,** 376–382 (2007).

38. Männikkö, R., Elinder, F. & Larsson, H. P. Voltage-sensing mechanism is conserved among ion channels gated by opposite voltages. *Nature* **419,** 837–841 (2002).

39. Cowgill, J. *et al.* Bipolar switching by HCN voltage sensor underlies hyperpolarization activation. *Proc. Natl. Acad. Sci. U. S. A.* **116,** 670–678 (2018).

40. Flynn, G. E. & Zagotta, W. N. Insights into the molecular mechanism for hyperpolarization-dependent activation of HCN channels. *Proc. Natl. Acad. Sci.* **115,** 8086–8095 (2018).

41. Zagotta, W. N. *et al.* Structural basis for modulation and agonist specificity of HCN pacemaker channels. *Nature* **425,** 200–205 (2003).

42. Zong, X. *et al.* Regulation of Hyperpolarization-activated Cyclic Nucleotide-gated (HCN) channel activity by cCMP. *J. Biol. Chem.* **287,** 26506–26512 (2012).

43. Xu, X., Vysotskaya, Z. V., Liu, Q. & Zhou, L. Structural basis for the cAMP-dependent gating in the human HCN4 channel. *J. Biol. Chem.* **285,** 37082–37091 (2010).

44. Verkerk, A. O. & Wilders, R. Pacemaker activity of the human sinoatrial node: An update on the effects of mutations in hcn4 on the hyperpolarization-activated current. *Int. J. Mol. Sci.* **16,** 3071–3094 (2015).

45. Zhang, G., Liu, Y., Ruoho, A. E. & Hurley, J. H. Structure of the adenylyl cyclase catalytic core. *Nature* **386,** 247–253 (1997).

46. Gordan, R., Gwathmey, J. K. & Xie, L.-H. Autonomic and endocrine control of cardiovascular function. *World J. Cardiol.* **7,** 204–214 (2015).

47. Stieber, J. *et al.* The hyperpolarization-activated channel HCN4 is required for the generation of pacemaker action potentials in the embryonic heart. *Proc. Natl. Acad. Sci.* **100,** 15235–15240 (2003).

48. Harzheim, D. *et al.* Cardiac pacemaker function of HCN4 channels in mice is confined to embryonic development and requires cyclic AMP. *EMBO J.* **27,** 692–703 (2008).

49. Baruscotti, M. *et al.* Deep bradycardia and heart block caused by inducible cardiac-specific knockout of the pacemaker channel gene Hcn4. *Proc. Natl. Acad. Sci.* **108,** 1705–1710 (2011).

50. Herrmann, S., Stieber, J., Stöckl, G., Hofmann, F. & Ludwig, A. HCN4 provides a 'depolarization reserve' and is not required for heart rate acceleration in mice. *EMBO J.* **26,** 4423–4432 (2007).

51.   Schulze-Bahr, E. *et al.* Pacemaker channel dysfunction in a patient with sinus node disease. *J. Clin. Invest.* **111,** 1537–1545 (2003).

52.   Schweizer, P. A. *et al.* cAMP Sensitivity of HCN Pacemaker Channels Determines Basal Heart Rate But Is Not Critical for Autonomic Rate Control. *Circ. Arrhythmia Electrophysiol.* **3,** 542–552 (2010).

53.   Alig, J. *et al.* Control of heart rate by cAMP sensitivity of HCN channels. *Proc. Natl. Acad. Sci.* **106,** 12189–12194 (2009).

54.   Verkerk, A. O. & Wilders, R. Pacemaker activity of the human sinoatrial node: effects of HCN4 mutations on the hyperpolarization-activated current. *EP Eur.* **16,** 384–395 (2014).

55.   Herron, T. J., Lee, P. & Jalife, J. Optical imaging of voltage and calcium in cardiac cells & tissues. *Circ. Res.* **110,** 609–623 (2012).

56.   Efimov, I. R., Nikolski, V. P. & Salama, G. Optical Imaging of the Heart. *Circ. Res.* **95,** 21–33 (2004).

57.   Salzberg, B. M., Davila, H. V. & Cohen, L. B. Optical Recording of Impulses in Individual Neurones of an Invertebrate Central Nervous System. *Nature* **246,** 508–509 (1973).

58.   Salama, G. & Morad, M. Merocyanine 540 as an optical probe of transmembrane electrical activity in the heart. *Science.* **191,** 485–487 (1976).

59.   Morad, M. & Salama, G. Optical probes of membrane potential in heart muscle. *J. Physiol.* **292,** 267–295 (1979).

60.   Matson, M., Carlsson, N., Beke-Somfai, T. & Nordén, B. Spectral Properties and Orientation of Voltage-Sensitive Dyes in Lipid Membranes. *Langmuir* **28,** 10808–10817 (2012).

61.   Loew, L. M. Design and characterization of electrochromic membrane probes. *J. Biochem. Biophys. Methods* **6,** 243–260 (1982).

62.   Clarke, R. J., Zouni, A. & Holzwarth, J. F. Voltage sensitivity of the fluorescent probe RH421 in a model membrane system. *Biophys. J.* **68,** 1406–1415 (1995).

63.   Fluhler, E., Burnham, V. G. & Loew, L. M. Spectra, membrane binding, and potentiometric responses of new charge shift probes. *Biochemistry* **24,** 5749–5755 (1985).

64.   Efimov, I. R., Fedorov, V. V., Joung, B. & Lin, S. Mapping Cardiac Pacemaker Circuits: Methodological Puzzles of the Sino-Atrial Node Optical Mapping. *Circ. Res.* **106,** 255–271 (2010).

65.   Matiukas, A. *et al.* Near-infrared voltage-sensitive fluorescent dyes optimized for optical mapping in blood-perfused myocardium. *Hear. Rhythm* **4,** 1441–1451 (2007).

66.   Swift, L. M. *et al.* Properties of blebbistatin for cardiac optical mapping and other imaging applications. *Pflugers Arch. Eur. J. Physiol.* **464,** 503–512 (2012).

67.   Entcheva, E., Kostov, Y., Tchernev, E. & Tung, L. Fluorescence Imaging of Electrical Activity in Cardiac Cells Using An All-Solid-State System. *IEEE Trans. Biomed. Eng.* **51,** 333–341 (2004).

68. Shen, M. J. & Zipes, D. P. Role of the Autonomic Nervous System in Modulating Cardiac Arrhythmias. *Circ. Res.* **114,** 1004–1021 (2014).

69. Pauza, D. H. *et al.* Neuroanatomy of the murine cardiac conduction system. *Auton. Neurosci.* **176,** 32–47 (2013).

70. Baudrie, V., Laude, D. & Elghozi, J. Optimal frequency ranges for extracting information on cardiovascular autonomic control from the blood pressure and pulse interval spectrograms in mice. *J. Physiol.* **292,** R904-12 (2007).

71. Just, A., Faulhaber, J. & Ehmke, H. Autonomic cardiovascular control in conscious mice. *Am J Physiol Regul Integr Comp Physiol* **279,** R2214-2221 (2000).

72. Bernardi, L. *et al.* Respiratory sinus arrhythmia in the denervated human heart. *J. Appl. Physiol.* **67,** 1447–1455 (1989).

73. Stauss, H. M. Heart rate variability. *Am. J. Physiol. Integr. Comp. Physiol.* **285,** R927–R931 (2003).

74. Evans, S. *et al.* Heart rate variability as a biomarker for autonomic nervous system response differences between children with chronic pain and healthy control children. *J. Pain Res.* **6,** 449–457 (2013).

75. Abboud, F. M., Liberles, S. D. & Patapoutian, A. PIEZOs mediate neuronal sensing of blood pressure and the baroreceptor reflex. *Science.* **362,** 464–467 (2018).

76. Scharr, A. Ein genetischer Ansatz zur Analyse der cAMP-abhängigen Modulation des Schrittmacherkanals HCN4. (2011).

77. Iancu, R. V. *et al.* Cytoplasmic cAMP concentrations in intact cardiac myocytes. *Am. J. Physiol. Physiol.* **295,** C414–C422 (2008).

78. Bunting, M., Bernstein, K. E., Greer, J. M., Capecchi, M. R. & Thomas, K. R. Targeting genes for self-excision in the germ line. *Genes Dev.* **13,** 1524–1528 (1999).

79. Gruner, C. Herstellung eines Knockin Mausmodells mit veränderter Modulation des HCN2-Ionenkanals. (2011).

80. Laughner, J. I., Ng, F. S., Sulkin, M. S., Arthur, R. M. & Efimov, I. R. Processing and analysis of cardiac optical mapping data obtained with potentiometric dyes. *Am J Physiol Hear. Circ Physiol* **303,** H753–H765 (2012).

81. Saponaro, A. *et al.* A synthetic peptide that prevents cAMP regulation in mammalian hyperpolarization-activated cyclic nucleotide-gated (HCN) channels. *Elife* **7,** 1–22 (2018).

82. Loew, L. M. Potentiometric dyes: Imaging electrical activity of cell membranes. *Pure Appl. Chem.* **68,** 1405–1409 (1996).

83. Ronzhina, M. *et al.* Application of the optical method in experimental cardiology: Action potential and intracellular calcium concentration measurement. *Physiol. Res.* **62,** 125–137 (2013).

84. Preuss, S. & Stein, W. Comparison of Two Voltage-Sensitive Dyes and Their Suitability for Long-Term Imaging of Neuronal Activity. *PLoS One* **8,** e75678 (2013).

85. Fedorov, V. V. *et al.* Application of blebbistatin as an excitation-contraction uncoupler

for electrophysiologic study of rat and rabbit hearts. *Hear. Rhythm* **4,** 619–626 (2007).

86. Bachtel, A. D. *et al.* A Novel Approach to Dual Excitation Ratiometric Optical Mapping of Cardiac Action Potentials With Di-4-ANEPPS Using Pulsed LED Excitation. *IEEE Trans. Biomed. Eng.* **58,** 2120–2126 (2011).

87. Boukens, B. J., Rivaud, M. R., Rentschler, S. & Coronel, R. Misinterpretation of the mouse ECG: 'musing the waves of Mus musculus'. *J. Physiol.* **592,** 4613–26 (2014).

88. Swenne, C. A. Baroreflex sensitivity : mechanisms and measurement. *Neth Hear. J.* **21,** 58–60 (2013).

89. Perego, M., Ramera, L. & Santilli, R. A. Isorhythmic Atrioventricular Dissociation in Labrador Retrievers. *J. Vet. Intern. Med.* **26,** 320–325 (2012).

90. Fedorov, V. V., Glukhov, A. V. & Chang, R. Conduction barriers and pathways of the sinoatrial pacemaker complex: their role in normal rhythm and atrial arrhythmias. *AJP Hear. Circ. Physiol.* **302,** H1773–H1783 (2012).

91. Boineau, J. P. *et al.* Demonstration of a widely distributed atrial pacemaker complex in the human heart. *Circulation* **77,** 1221–1238 (1988).

92. Boineau, J. P. *et al.* Widespread distribution and rate differentiation of the atrial pacemaker complex. *Am. J. Physiol. Circ. Physiol.* **239,** H406–H415 (1980).

93. Parati, G., Di Rienzo, M. & Mancia, G. How to measure baroreflex sensitivity : from the cardiovascular laboratory to daily life. *J. Hypertens.* **18,** 7–19 (1999).

94. Laude, D., Baudrie, V. & Elghozi, J.-L. Applicability of recent methods used to estimate spontaneous baroreflex sensitivity to resting mice. *Am. J. Physiol. Integr. Comp. Physiol.* **294,** R142–R150 (2008).

95. Robbe, H. W. *et al.* Assessment of baroreceptor reflex sensitivity by means of spectral analysis. *Hypertension* **10,** 538–543 (1987).

96. Pauza, D. H. *et al.* Neuroanatomy of the murine cardiac conduction system. *Auton. Neurosci.* **176,** 32–47 (2013).

97. Bergfeldt, L. & Haga, Y. Power spectral and Poincaré plot characteristics in sinus node dysfunction. *J. Appl. Physiol.* **94,** 2217–2224 (2003).

98. Campbell, G. D., Edwards, F. R., Hirst, G. D. . S. & O´Shea, J. E. Effects of vagal stimulation and applied acetylcholine on pacemaker potentials in the guinea-pig heart. *J. Physiol.* **415,** 57–68 (1989).

99. Vinogradova, T. M., Fedorov, V. V, Yuzyuk, T. N. & Rosenshtraukh, L. V. Local cholinergic supression of pacemaker activity in the rabbit sioatrial node. *J Cardiovasc Pharmacol* **32,** 413–24 (1998).

100. Lang, D., Petrov, V., Lou, Q., Osipov, G. & Efimov, I. R. Spatiotemporal control of heart rate in a rabbit heart. *J. Electrocardiol.* **44,** 626–634 (2011).

101. Fenske, S., Hennis, K. & Rötzer, R. Current scientific collaborators in the Faculty of Chemistry and Pharmacy, Department of Pharmacy, Pharmacology for Natural Sciences, LMU Munich. (2019).

102. DiFrancesco, D. & Mangoni, M. Modulation of single hyperpolarization-activated

channels (i(f)) by cAMP in the rabbit sino-atrial node. *J. Physiol.* **474,** 473–482 (1994).

103. Spector, P. Principles of Cardiac Electric Propagation and Their Implications for Re-entrant Arrhythmias. *Circ. Arrhythmia Electrophysiol.* **6,** 655–661 (2013).

104. Bucchi, A., Baruscotti, M., Robinson, R. B. & DiFrancesco, D. If-dependent modulation of pacemaker rate mediated by cAMP in the presence of ryanodine in rabbit sino-atrial node cells. *J. Mol. Cell. Cardiol.* **35,** 905–913 (2003).

105. Brown, H. F., DiFrancesco, D. & Noble, S. J. How does adrenaline accelarete the heart? *Nature* **280,** 235–236 (1979).

106. Kerr, C. R., Prystowsky, E. N., Smith, W. M., Cook, L. & Gallagher, J. J. Electrophysiologic effects of disopyramide phosphate in patients with Wolff-Parkinson-White syndrome. *Circulation* **65,** 869–878 (1982).

9   List of figures

10 List of abbreviations

ACh	Acetylcholine
ANEP	Aminonaphthylethenylpyridinium
ANS	Autonomic nervous system
AO	Aorta
AP	Action potential
APD	Action potential duration
ATP	Adenosine triphosphate
AV delay	Atrio-ventricular delay
AVB	Atrioventricular bundle
AVJ	Atrio-ventricular junction
AVN	Atrioventricular node
BB	Bundle branches
BP	Blood pressure
Bpm	Beats per minute
BPV	Blood pressure variability
BRS	Baroreflex sensitivity
cAMP	Cyclic adenosine monophosphate
CCD	Charge-coupled device
cCMP	Cyclic cytosine monophosphate
CDR	cAMP-dependent regulation
CFB	Central fibrous body
cGMP	Cyclic guanosine monophosphate
CMOS	Complementary metal oxide semiconductor cameras
CNBD	Cyclic nucleotide binding domain
CNG	Cyclic nucleotide-gated
CT	Crista terminalis
Cx	Connexin
DBP	Diastolic blood pressure
DMSO	Dimethyl sulfoxide
DNA	Deoxyribonucleic acid
ECG	Electrocardiogram
FFT	Fast Fourier transform
FIR filter	Finite impulse response filter
G protein	Guanine nucleotide-binding protein

GC	Ganglia complex
GPCR	G protein-coupled receptor
GYG	Glycine-tyrosine-glycine
HCN channel	Hyperpolarization-activated cyclic nucleotide-gated channel
HF	High frequency
HR	Heart rate
HRV	Heart rate variability
IAS	Interatrial septum
IAVD	Isorhythmic atrioventricular dissociation
I_h	Hyperpolarization-activated current
IHC	Immunohistochemistry
IVC	Inferior vena cava
JER	Junctional escape rhythm
KCNH	Voltage-dependent potassium channels (ether-á-go-go-type)
LA	Left atrium
LA	Low activity phase
LED	light-emitting diodes
LF	Low frequency
LP	Leading pacemaker
LSVC	Left superior vena cava
LV	Left ventricle
M2-receptor	Type-2 muscarinic receptor
MV	Mitral valve
NN	Normal-normal interval
OAP	Optical action potential
OPSL	Optically pumped semiconductor laser
PA	Pulmonary artery
PBS	Phosphate buffered saline
PCR	Polymerase chain reaction
PF	Purkinje fibre
PFA	Paraformaldehyde
PV	Pulmonary vein
RA	Right atrium
RMSSD	Root mean square of the successive differences
RT	Room temperature
RV	Right ventricle
SACP	Sinoatrial conduction pathways

SACT	Sinoatrial conduction time
SAN	Sinoatrial node
SBP	Systolic blood pressure
SDD	Slow diastolic depolarization
SDNN	Standard deviation of the NN interval
ST	Sulcus terminalis
SVC	Superior vena cava
tACE	Testis-specific promoter from the angiotensin-converting enzyme
tAct	Activation time
TV	Tricuspid valve
VLF	Very low frequency
VN	Vagus nerve
VNS	Vagus nerve stimulation
VSD	Voltage sensing domain
WT	Wildtype

11 Appendix

11.1 Tables of data

Table 1: Heart rate analysis of 72 h telemetric ECG recordings

Parameter	WT	n	HCN4 FEA	n	p-value
HR mean 72h [bpm]	522.91 ± 8.33	9	435.88 ± 13.64	11	0.00007
HR max 72h [bpm]	726.65 ± 9.25	9	662.82 ± 16.15	11	0.00467
HR min 72h [bpm]	355.25 ± 8.52	9	299.70 ± 11.27	11	0.00136
Dynamic range 72h [bpm]	371.40 ± 12.72	9	363.12 ± 18.46	11	0.72857
Degree of HR reg 72h [bpm]	2.05 ± 0.05	9	2.24 ± 0.09	11	0.12640
HR mean LA [bpm]	501.52 ± 11.13	9	417.00 ± 13.68	11	0.00020
HR max LA [bpm]	707.91 ± 12.22	9	642.22 ± 15.68	11	0.00508
HR min LA [bpm]	362.87 ± 9.64	9	299.70 ± 11.27	11	0.00061
Dynamic range LA [bpm]	345.04 ± 9.15	9	342.53 ± 17.34	11	0.90590
Degree of HR reg LA [bpm]	1.96 ± 0.04	9	2.17 ± 0.09	11	0.05674
HR mean HA [bpm]	544.10 ± 6.89	9	454.75 ± 13.81	11	0.00004
HR max HA [bpm]	720.64 ± 7.49	9	661.60 ± 16.41	11	0.00563
HR min HA [bpm]	375.03 ± 11.61	9	313.79 ± 12.95	11	0.00289
Dynamic range HA [bpm]	345.61 ± 13.47	9	347.82 ± 18.95	11	0.92852
Degree of HR reg HA [bpm]	1.94 ± 0.06	9	2.14 ± 0.10	11	0.11110

Mean ± SEM; n= number of animals

Table 2: Time domain and frequency domain analysis of telemetric ECG data

Parameter	WT	n	HCN4 FEA	n	p-value
RR [ms]	132.24 ± 2.67	9	151.59 ± 5.05	11	0.0053
SDNN [ms]	11.60 ± 0.69	9	24.37 ± 2.28	11	0.0001
RMSSD [ms]	9.38 ± 1.09	9	19.64 ± 2.53	11	0.0029
VLF power [$\sqrt{ms}$/Hz]	10.63 ± 2.82	9	64.17 ± 12.54	11	0.0014
LF power [$\sqrt{ms}$/Hz]	9.22 ± 3.05	9	77.46 ± 32.45	11	0.0754
HF power [$\sqrt{ms}$/Hz]	11.66 ± 3.44	9	42.29 ± 12.61	11	0.0468

Mean ± SEM; n= number of animals;

Table 3: Analysis of combined telemetric BP and ECG data

Parameter	WT	n	HCN4 FEA	n	p-value
RR [ms]	124.77 ± 2.96	9	155.70 ± 5.62	11	0.0002
DBP [mmHg]	86.33 ± 2.01	9	79.17 ± 1.92	11	0.0196
SBP [mmHg]	112.62 ± 1.57	9	111.05 ± 2.55	11	0.6241
Sequences/1000 beats	23.72 ± 4.76	9	19.02 ± 3.52	11	0.4282
$Slope_{up}$ [ms/mmHg]	4.21 ± 0.25	9	7.63 ± 1.23	11	0.0238
$Slope_{down}$ [ms/mmHg]	4.09 ± 0.39	9	8.93 ± 1.49	11	0.0103

Mean ± SEM; n= number of animals

Table 4: Electrical recordings of biatrial SAN preparations

Parameter	WT	n	HCN4 FEA	n	p-value
Beating rate [bpm]	302.91 ± 7.42	26	247.28 ± 11.85	31	0.0004
SDNN [ms]	4.18 ± 0.76	26	14.98 ± 3.37	31	0.0057
RMSSD [ms]	4.44 ± 1.14	26	20.49 ± 5.01	11	0.0057

Mean ± SEM; n= number of animals

Table 5: Optical mapping and electrical recordings of biatrial SAN preparations

Parameter	WT	n	HCN4 FEA	n	p-value
SACT [ms]	4.86 ± 0.37	7	7.44 ± 0.57	8	0.0029
Beating rate$_{before\ Carbachol}$ [bpm]	288.20 ± 6.44	13	235.74 ± 14.19	16	0.0043
Beating rate$_{Carbachol}$ [bpm]	151.87 ± 5.63	13	109.55 ± 5.24	16	0.000008
LP shift$_{Carbachol}$	0.503 ± 0.075	7	0.624 ± 0.090	8	0.3261
Beating rate$_{before\ VNS}$ [bpm]	330.83 ± 18.76	6	322.5 ± 17.52	7	0.7620
Mean RR$_{VNS\ 20Hz}$ [s]	0.396 ± 0.053	6	0.491 ± 0.194	7	0.6676
LP shift$_{VNS\ 20Hz}$	0.478 ± 0.177	4	1.044 ± 0.119	4	0.0381

Mean ± SEM; n= number of animals

Table 6: Confocal calcium recordings of SAN cell within the intact SAN network

Parameter	WT	n	HCN4 FEA	n	p-value
N cells/µm^2 [*10^{-3}]$_{basal}$	0.60 ± 0.16	8	1.51 ± 0.35	8	0.0330
N cells/µm^2 [*10^{-3}]$_{TRIP8bnano}$	4.24 ± 1.41	4	--- ---	---	---

Mean ± SEM; n= number of animals

11.2 Publications

Fenske, S., **V. F. Brox**, K. Hennis, R. Roetzer, E. Becirovic, A. Scharr, C. Gruner, T. Ziegler, V. Hammelmann, J. Brennan, I. R. Efimov, A. G. Pauza, M. Moser, C. T. Wotjak, C. Kupatt, R. Goenner, X. Zong, M. Biel, and C. Wahl-Schott. **2019**. *"A Previously Unknown Component of the Chronotropic Effect Is Controlled by cAMP-Dependent Regulation of HCN4."* Submitted to Circulation Research.

Lin, H. C. A., X. L. Déan-Ben, M. Reiss, **V. Schöttle**, C. A. Wahl-Schott, I. R. Efimov, and D. Razansky. **2018**. *"Ultrafast Volumetric Optoacoustic Imaging of Whole Isolated Beating Mouse Heart."* Scientific Reports 8(1):1–7.

Stieglitz, M. S., S. Fenske, V. Hammelmann, E. Becirovic, **V. Schöttle**, J. E. Delorme, M. Schöll-Weidinger, R. Mader, J. Deussing, D. P. Wolfer, M. W. Seeliger, U. Albrecht, C. T. Wotjak, M. Biel, S. Michalakis, and C. Wahl-Schott. **2018**. *"Disturbed Processing of Contextual Information in HCN3 Channel Deficient Mice."* Frontiers in Molecular Neuroscience 10:436.

Straubinger, J., **V. Schöttle**, N. Bork, H. Subramanian, S. Dünnes, M. Russwurm, M. Gawaz, A. Friebe, M. Nemer, V. O. Nikolaev, and R. Lukowski. **2015**. *"Sildenafil Does Not Prevent Heart Hypertrophy and Fibrosis Induced by Cardiomyocyte Angiotensin II Type 1 Receptor Signaling."* Journal of Pharmacology and Experimental Therapeutics 354(3):406–16.

11.3 Acknowledgements